Millimeter-Wave Polarimetric Radar Sensor for Detection of Power Lines in Strong Clutter Background

by

Moonsoo Park

A dissertation submitted in partial fulfillment
of the requirements for the degree of
Doctor of Philosophy
(Electrical Engineering)
in The University of Michigan
2003

Doctoral Committee:
Professor Kamal Sarabandi, Chair
Professor Fawwaz Ulaby
Professor Anthony W. England
Professor Wayne E. Stark
Research Scientist Valdis Liepa

To my wife and children for their support and sacrifice

ACKNOWLEDGEMENTS

First of all, I give my sincere gratitude and appreciation to my academic advisor Dr. Kamal Sarabandi for his guidance, patience, and encouragement during my Ph.D. journey. I was very fortunate to have him as my advisor. Dr. Sarabandi's broad academic background and positive attitude towards his field of study and his students was always an inspiration to me. I always was able to revive my energy due to his encouragement whenever I got frustrated. I also would like to thank all my committee members for their time and consideration.

I owe many thanks to Dr. Adib Nashashibi, who introduced me to millimeter-wave polarimetric radar, and to Dr. Leland Pierce, who always had answers to my questions related to computers and radar image processing. I also want to thank Mark D. Casciato for his kind help and proofreading, including this dissertation.

My time in the Rad Lab was enjoyable and memorable due to the Rad Lab staff and my Rad Lab friends. I would also like to express my appreciation to my Korean buddies for their help and friendship including Dr. Il-Seuk Koh, Dr. Kyoung Yang, and Yongshik Lee. I apologize to those people whose names I've missed here; my thanks goes to you nonetheless for any help you have given me to make my work easier.

I give my special appreciation to my mother-in-law, Y.J. Jung for her love and patience. She did not miss a single day of praying for me for many years. Finally I would like to thank and acknowledge my family: my wife, Mehyun L. Park and my children, Jeeyun, and Phillipe. I would not have been able to complete this journey towards my Ph.D. degree without their love and many sacrifices.

I should also mention that my graduate studies in Michigan were supported by the U.S. Army Research Laboratory under Cooperative Agreement DAAL01-96-2-0001.

TABLE OF CONTENTS

LIST OF TABLES

LIST OF FIGURES

Figure

CHAPTER 1

INTRODUCTION

1.1 Introduction

Since its invention at the first of the 20th century, the use of helicopters for military and civilian applications is ever increasing. The civilian applications cover a broad range including rescue operations, air ambulance, recreation, construction, etc.. Helicopters also have a broad range of applications in military. They provide superiority over rugged battle fields and constitute a formidable force against armored vehicles and heavy artillery. Operation of these fast low-flying machines, however, is highly limited under poor visibility. The major safety problem is the collision with man-made and natural obstacles such as towers, power lines and mountains.

When crossing rivers and valleys, power transmission lines can be as high as several hundred feet above ground level. Guy wires that support towers may be almost invisible to pilots, even if the general location of the wires is known. Pilots' ability to see wires is affected by dirty windscreens, light conditions, the obscuring effects

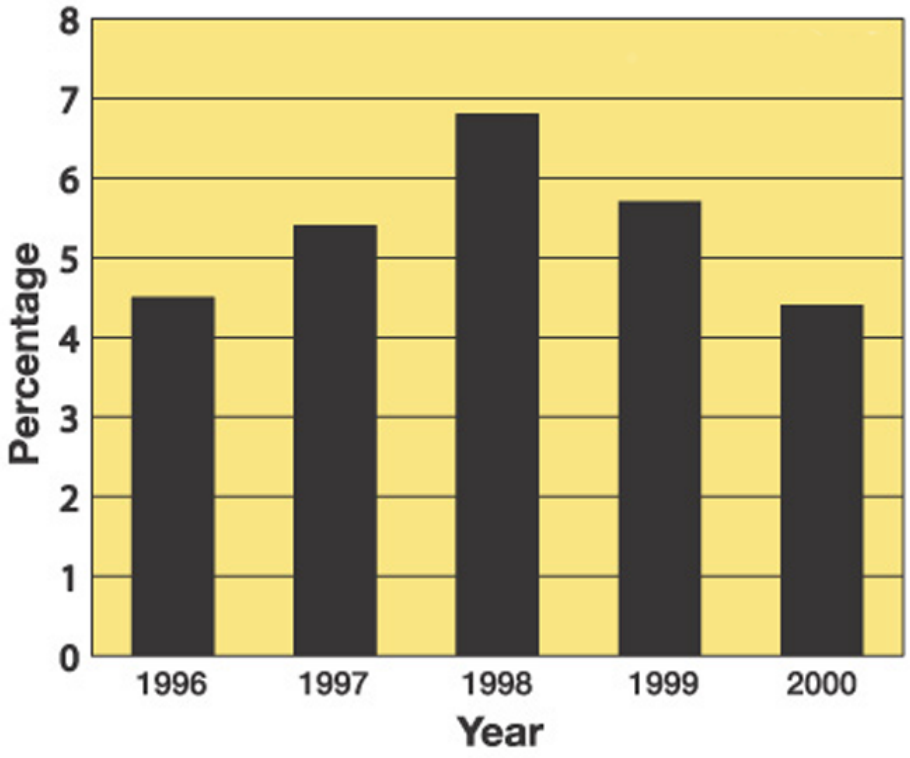

Figure 1.1: Wire-strike accidents as a percentage of all US commercial helicopter accidents, 1996-2000. (934 in total)

of terrain and changes in visual perspective that occur during climb and descent. In addition, accurately judging the helicopter's distance from unmarked wires is nearly impossible. Wires are difficult to see, partly because of the way the human eye functions and partly because of the effects of some backgrounds and light angles in camouflaging wires. Their low observability makes them difficult to detect and in the U.S. alone, tens of helicopter collisions with power lines are reported every year [1]. Data show that, of 934 U.S.-registered civilian helicopters involved in accidents from 1996 through 2000, 50 accidents (5.4 percent) were classified as wire-strike accidents. (See Figure 1.1.) Due to the existing poor safety records of helicopters, strict

Figure 1.2: A rescue helicopter approaching cables

safety regulations have been put in place to ensure helicopters stay grounded under conditions of bad visibility even in emergencies. A reliable and all-weather collision warning system rectifies this deficiency. Several wire detection systems have been proposed. For example, one of the power line detection system senses the electromagnetic field generated by live electrical power lines and emits an audible alert through the aircraft's audio system–a clicking sound that increases in frequency as the aircraft is flown nearer to a "live" electric power line (a line carrying electric current)–and illuminates a red warning light in the cockpit. The warnings are provided regardless of whether the helicopter is approaching the power line from above, below, or at an oblique angle. The system does not alert pilots to wires that are not live, however. Another system is a wire-strike protection system designed to help protect the he-

licopter in the event of inadvertent flight into horizontally strung wires or cables. The equipment consists of a windshield deflector, an upper cutter/deflector and a lower cutter/deflector. (The cutter/deflectors are sharp blades above the windshield and below the nose of the aircraft). Each cutter consists of high-tensile-steel cutting blades designed to cut through the wires, thus preventing them from catching the mast, flight controls, or landing gear and preventing them from slicing through the cockpit. For this system to be effective, however, the helicopter should approach the wire with proper incidence angle. And this system fails to work when vertical spacing between power lines are not far enough. Honeywell's Enhanced Ground-proximity Warning System (EGPWS) warns for approximately 30-seconds pilots of rising terrain and obstacles (including power lines) that are 100 feet or more above ground level. This system has database showing all low-level obstacles in North America of 100 feet and above. Position data on radio and TV towers, buildings and bridges all are contained in the box. The system does not yet contain data on the location of power lines in the United States, in part because some power companies have not cooperated. There may be good reasons why power companies are reluctant to share power-grid information. For one thing, the data could fall into the wrong hands, terrorists. However, without the data on location of power lines, this warning system can not function successfully.

In the past, several approaches for detecting nearby power line cables have been proposed which include optical and infrared sensors [4, 6]. This system offers many advantages including fine resolution and compactness, however there are a number of major limitations including limited range, significant atmospheric attenuation un-

Figure 1.3: High voltage power lines and towers

der inclement weather conditions, and limited ability to automate the wire detection warning for pilots. As a results of these limitations, these laser systems have not preceded beyond the demonstration phase. Millimeter-wave frequency band has several advantages over both microwave band and infrared/optical band for radar applications. [2] Since antenna gain of radar is promotional to the frequency squared, millimeter-wave antenna has higher angular resolution than that of microwave antenna of same size. This results in reduced multipath, ground clutter and improved discrimination of closely spaced targets. Shorter wavelength of millimeter-wave band offers compactness of the system due to smaller antenna size and circuit dimensions. Another advantage of millimeter-wave frequency over microwave is wider bandwidth allowing higher range resolution of radar. Furthermore at millimeter-wave the sur-

face dimensions of power lines are comparable to the wavelength and unique features of radar backscatter can be used to detect power lines while the radar backscatter of power lines is similar to that of smooth cylinders at microwave frequencies. [8] Millimeter-wave radar has the advantage over infrared/optical band of relaying target information even under low visibility conditions, and millimeter-wave sensors are economically viable due to the advances in millimeter-wave technology.

The detection of power lines, independent of frequency of the sensor, is very challenging since the cross section of these cables are rather small. Radar cross section (RCS) of power lines is small at millimeter-wave frequencies and clutter levels can dominate the radar echo. Because of this several detection algorithms have been proposed to separate the power line return from the clutter. These algorithms must be automatic and provide the pilot with sufficient time to respond to the threat of collision with power line.

A automatic detection of targets using radars was initiated by Marcum [9], and later Swering [10] in 1960s. Marcom generated curves of probability of detection (PD) versus signal-to-noise (S/N). In his work, a constant false alarm (CFAR) was applied assuming that the environment was known, homogeneous and that a fixed threshold worked well for detection. In a realistic environment, however, fixed threshold can cause exorbitant false alarm (FA) rates. Various methods have been proposed to solve the FA problems. [11]-[18] They can be categorized into two main groups, adaptive parametric, and non-parametric. In parametric method the threshold is adaptively changed by estimating parameters from the surrounding reference cells. Clutter distribution has to be known in this design. A non-parametric type is not designed for

a specific probability density function (pdf) and works fairly well with a wide variety of pdf with a slight reduction in probability of detection. All of the detection schemes mentioned above depend on amplitude information of the backscattered signal and are limited when there is not enough signal-to-clutter ratio. However the clutter tends to dominate the backscattered signal for off normal incidence angles.

Radar polarimetry, based on the measurement of complete radar scattering matrix allows new detection scheme. It provides useful information that is not available from single channel processing. Several polarimetric detection algorithms have been proposed. Yamada [19] used polarimetric FM-CW radar to classify targets buried in the underground. A polarization anisotropy coefficient is used to distinguish man-made targets from natural targets and polarimetric signature approach is used to find the angle of the anisotropic targets. However this approach does not work if signal-to-clutter is below a certain level. In power line detection this signal-to-clutter ratio may be below this level. Novak [21] considered target detection with polarimetric SAR. Polarimetric SAR images are first processed by polarimetric whitening filter (PWF) to minimize the clutter standard deviation (σ_c). The output image is then used for target detection. Various polarization combinations (HH, VV, HH-VV, LL, *etc*) were evaluated to find the optimum polarization which maximize the signal-to-clutter ratio. The correlation between the co- and cross-polarized channel in the targets is not used which may improve the signal-to-clutter ratio.

Target detection from SAR (Synthetic Aperture Radar) images has been studied by many authors. [19]-[27] High resolution SAR technology provide a useful tool for detecting small objects included in the clutter. Kuga [22] proposed an approach for

3-D imaging in a heavy-clutter environment. Circular SAR image is generated at X-band frequency by moving the antenna in circular orbit whereas SAR platform moves linearly in a flight path. Clutter is suppressed by angular correlation function. Circular orbiting is not applicable to power line detection since helicopters fly in a linear path. Klausing [20] used the Rotor-SAR (ROSAR) concept to generate high resolution images for the detection of power lines and its supporting towers. It is based on the circular-shape synthetic aperture by rotating antennas mounted in the helicopter rotor. Obstacles are detected by comparing the image of the targets with the preprogrammed obstacle models. Polarimetric processing is not used in both SAR approaches and the target is not easily detected if the power line is immersed in a strong clutter. Both approach also demand exorbitant computing power and state-of-the-art super computers are required for data processing. This makes it impractical as a real-time detection tool.

A simpler detection algorithm which maintains the high accuracy of detection is being considered in this thesis work. It does not require high resolution SAR images and can be processed in real time. The feasibility of this algorithm for detection of power lines using millimeter-wave polarimetric radar is researched. Theoretical and experimental investigations show that co- and cross- polarized component of radar back scatter of natural random media with azimuthal symmetry are uncorrelated. The polarimetric detection algorithm proposed is based on the polarimetric scattering characteristics of power lines. These characteristics were observed by measuring several typical power lines. The average co- and cross- polarized components if the scattering matrix are strongly correlated for power lines while they are uncor-

related for natural clutters. By taking ensemble average of pixels clutter level can be suppressed significantly and signal-to-clutter ratio is enhanced resulting in easier detection of power lines in the presence of clutters.

The accurate prediction of polarimetric backscatter of power lines for arbitrary strand arraignment is of great importance in the development of a millimeter–wave detection system, however a polarimetric RCS model does not exist. Rembold [5] modelled radar backscatter of power lines using physical optics at microwave frequencies. Power lines are simplified as a smooth cylinder. This model does not account for Bragg scattering and cross-polarization is not considered. Al-Kahatib [4] measured RCS of power lines at four millimeter-wave frequencies (18, 34, 56, 94 GHz) and two laser wave length (10.6 and 1.06 um). This geometrical theory of diffraction (GTD) based model is capable of predicting Bragg scattering. RCS is calculated for co-polarized component (VV, HH) without considering cross-polarization. In this thesis work, analytical RCS model is developed based on iterative physical optics. This model considers both co- and cross-polarized component. It is shown that the cross-polarized component is essential component in the proposed detection scheme.

The feasibility of power line detection further should be investigated in real situation. However, this is very costly and part of the goal can be fulfilled without launching a helicopter. One option is using Polarimetric SAR data which is already available. The other option is to build a radar simulator to demonstrate the feasibility of power line detection and to optimize the required hard specification for the best detection performance.

1.2 Radar Polarimetry

Any target can be characterized by its scattering matrix or Mueller matrix. The scattering matrix $\bar{\mathbf{S}}$ of the target relates the electric field $\bar{\mathbf{E}}^r$ received by the radar to the transmitted electric field $\bar{\mathbf{E}}^t$. The transmitted electric field $\bar{\mathbf{E}}^t$ and the reflected electric field $\bar{\mathbf{E}}^r$ are represented as

$$\bar{\mathbf{E}}^t = E_v^t \hat{\mathbf{v}} + E_h^t \hat{\mathbf{h}}$$

$$\bar{\mathbf{E}}^r = E_v^r \hat{\mathbf{v}} + E_h^r \hat{\mathbf{h}}$$

respectively.

Using the vector notation:

$$\bar{\mathbf{E}} = \begin{pmatrix} E_v \\ E_h \end{pmatrix}$$

the two fields can be related by the scattering matrix $\bar{\mathbf{S}}$:

$$\begin{pmatrix} E_v^r \\ E_h^r \end{pmatrix} = \frac{e^{ikr}}{r} \begin{pmatrix} S_{vv} & S_{vh} \\ S_{hv} & S_{hh} \end{pmatrix} \begin{pmatrix} E_v^t \\ E_h^t \end{pmatrix}$$

or

$$\bar{\mathbf{E}}^r = \frac{e^{ikr}}{r} \bar{\mathbf{S}} \bar{\mathbf{E}}^t$$

Once the scattering matrix is known by measurement or theoretical calculation, it is possible to synthesize the radar cross section(RCS) for any possible choice of transmit and receive antenna polarizations; this process is called "polarization synthesis" [32]. This important technique is what gives polarimetry its great advantage over conventional fixed-polarization radars—more information maybe inferred about the

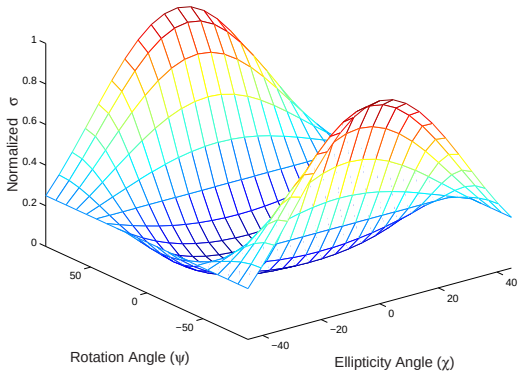

(a)Co-polarization

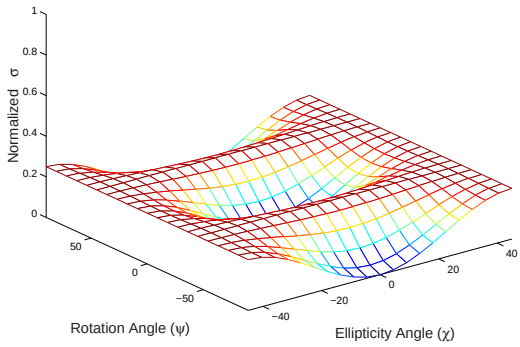

(b)Cross-polarization

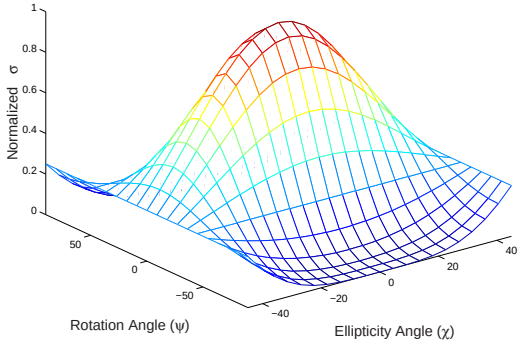

(c)Co-polarization

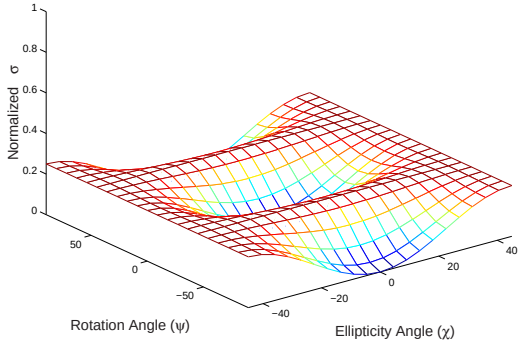

(d)Cross-polarization

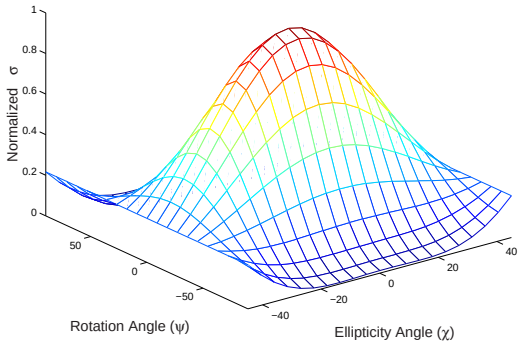

(e)Co-polarization

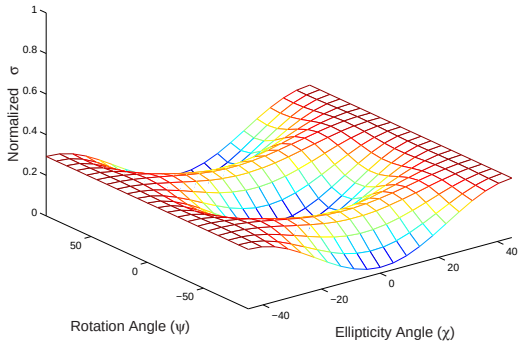

(f)Cross-polarization

Figure 1.4: Polarization signature of power line #1 and that of a conducting short, thin cylinder. (a)(b)Cylinder (vertical orientation) (c)(d)Cylinder (horizontal orientation) (e)(f)Power line#1 (horizontal orientation)

target if the full polarization is known. The radar cross section(RCS) for the choice of transmit antenna polarization t and receive antenna polarization r is defined as

$$\sigma_{rt}(\psi_r, \chi_r, \psi_t, \chi_t) = 4\pi|\bar{\mathbf{p}}^r \bar{\mathbf{S}} \bar{\mathbf{p}}^t|,$$

where $\bar{\mathbf{p}}^m$, the field polarization vector is given by

$$\bar{\mathbf{p}}^m = \frac{\bar{\mathbf{E}}^m}{|\bar{\mathbf{E}}^m|}, \qquad m = r, t,$$

and $\bar{\mathbf{S}}$ is the scattering matrix of the target. The rotation angle and ellipticity angle define the polarization of a electric field $\bar{\mathbf{E}}$

$$\bar{\mathbf{E}} = \hat{v} + a_m e^{i\delta_m} \hat{h}$$

where $\hat{v}$ and $\hat{h}$ are orthogonal unit vectors along the vertical and horizontal directions and

$$a_m = \frac{1 - \cos(2\psi_m)\cos(2\chi_m)}{1 + \cos(2\psi_m)\cos(2\chi_m)}$$
$$\delta_m = \tan^{-1} \frac{\tan(2\chi_m)}{\tan(2\psi_m)}.$$

Two kinds of responses are important and physically meaningful: co-polarized response and cross-polarized response. In the case of the co-polarized response, the transmit and receive antennas have the same polarization, whereas with the cross polarized response the receive antenna is polarized orthogonally to the transmit antenna. These conditions can be expressed mathematically as

$$\psi_r = \psi_t, \ \chi_r = \chi_t \qquad \text{Co} - \text{polarization}$$

$$\psi_r = \psi_t \pm \pi/2, \ \chi_r = -\chi_t \qquad \text{Cross} - \text{polarization}$$

It is interesting to compare the polarization response of power line and that of conducting short, thin cylinder. Figure 1.4(a) and Figure 1.4(b) show the polarization response for the cylinder oriented horizontally and Figure 1.4(c) and Figure 1.4(d) for the cylinder oriented vertically. Figure 1.4(e), and Figure 1.4(f) show the polarization response for power line #1 oriented horizontally. The plots for the cylinder were generated using simulated data (scattering matrix) and the plots for the power line were generated using the measured data. The plots show that the maximum co-polarized response occur at vv-polarization for the power line and vertically-oriented cylinder while the minimum response is at hh-polarization for the power line and vertically-oriented cylinder. In all three cases, the minimum cross-polarization response at vv- and hh-polarization. The polarization response of power line was expected to be similar to that of horizontal-oriented cylinder. Because the strands in the power line are arranged more horizontally rather than vertically. However the plots show that the response for the power line is rather similar to that of vertically-oriented cylinder.

1.3 Thesis Overview

This thesis is comprised of 7 chapters. Chapter 2 focuses on the results obtained from the radar back scatter measurement of power lines. Polarimetric backscatter measurements on a variety of power-line samples are performed. Using the polarimetric backscatter features of the power-lines, caused by its braided structure, a detection algorithm for detecting power-lines in a strong clutter background is developed and the feasibility is tested.

In Chapter 3, follows with analytical backscatter model of power lines. This model is a high frequency technique based on an iterative physical optics approach and polarimetric radar backscattering behavior of power lines of arbitrary strand arrangement is predicted using the model. The validity of the model was verified by comparing the calculated RCS with the measured data at 94 GHz.

In Chapter 4, statistical analysis of the detection algorithm is studied. The detection algorithm is based on the comparison between co- and cross-polarized coherence of clutter and that of a power line. The accuracy of the coherence estimation depend on the number of samples and analytical expression for the computation of false alarm (FA), probability of detection (PD), and number of samples (N) is formulated.

In Chapter 5 deals with the real aperture radar (RAR) images of a simulated flight scene. In-situ measurements of power lines with trees in the background were performed at Willow Run facilities of the University of Michigan simulating actual scenarios those might be encountered by flying helicopters. The collected data was processed to assess the performance of the detection algorithm.

Chapter 6 describes Power Line Detection Simulator developed in this thesis work. So far in the previous chapters the performance of the detection algorithm was examined under laboratory conditions and using a number of actual MMW SAR images. However one of the goals in this investigation is to examine the performance of a radar for the mission. A radar simulator was developed and the performance of the detection algorithm is tested using the simulator.

Chapter 7 deals with the results of this investigation, as well as suggestions for the potential research.

CHAPTER 2

MEASURED RESULTS OF POWER LINES AT MILLIMETER-WAVE FREQUENCIES

2.1 Introduction

High voltage power lines and their supporting towers create hazardous conditions for low-flying aircrafts and helicopters. Army aviation and other services have an urgent need for an automated system to alarm pilots of the existence, direction and the distance of nearby power line cables. In the past, a number of approaches including millimeter-wave radars have been proposed for detecting power lines [4]–[6]. An electro-optical laser approach is currently being pursued as a solution to this problem. Despite many advantages offered by such system including fine resolution and compactness, there are a number of major limitations including: 1) limited range, 2) significant atmospheric attenuation under inclement weather conditions , and 3) limited ability to automate the wire detection warning for pilots. As a results of these limitations, the laser systems have not preceded beyond the technology demon-

stration phase. Like electro-optical laser systems, relatively compact radar systems can be constructed at millimeter-wave frequencies, however, their performance are not limited by bad weather conditions. In this Chapter, the feasibility of power line detection using millimeter-wave radars is revisited. In [4], it is concluded that since significant backscatter exists only over narrow aspect angles near normal incidence at discrete Bragg directions, it is not possible to detect power lines with a high probability, especially in the presence of background clutter.

It is true that in a real radar environment, the presence of clutter may increase the false alarm rate to an extent which would impair target detectability. Radar polarimetry is usually used to improve the probability of detection and to reduce the false alarm rate [32]. For distinguishing a target in background clutter, structure dependent polarimetric features of the target must be characterized and employed in target detection. Power lines are made of strands of wires in helical arrangement and this can be exploited for detecting the power lines in a clutter background. At high frequencies, the effects of helicity and periodicity of power line surface features become important factors in the scattering behavior of power lines. Existence of cross-polarized component in the radar backscatter usually provides a unique target signature. Because of tilted grooves on the power line surface which can support corner reflector type multiple reflection, it is expected that a considerable cross-polarized backscatter will be generated. These effects are investigated in more details in this Chapter based on which a polarimetric detection algorithm is developed.

Four different power line samples of different diameters and strand arrangement were chosen and their backscatter responses were measured and compared with those

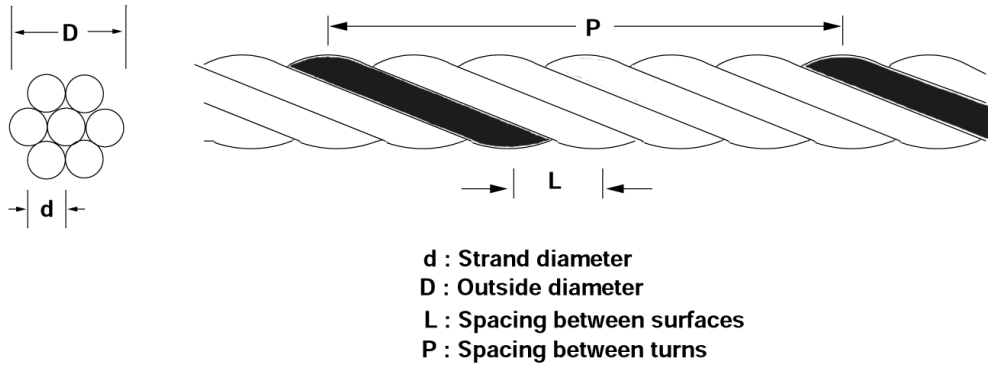

Figure 2.1: Geometry and important structural parameters of a power line.

of metallic cylinders having length and diameters identical to the length and diameters of the power line samples. Backscatter behavior of wet and frozen power lines are also reported to demonstrate the effect of a thin layer of water and ice on the polarimetric response of power lines. The polarimetric detection algorithm developed in this investigation is based on the expected coherence relation between the co- and cross-polarized backscatter component of power lines which allows target detection under a poor signal-to-clutter ratio. To examine the degree of coherence between the co- and cross-polarized backscatter, histograms of backscatter measurements at different aspect angles, were obtained by moving the antenna footprint along the power lines and by rotating the power lines about their axes. Finally, the success of the detection algorithm is tested by measuring the backscatter from a power line in the presence of a strong backscatter clutter.

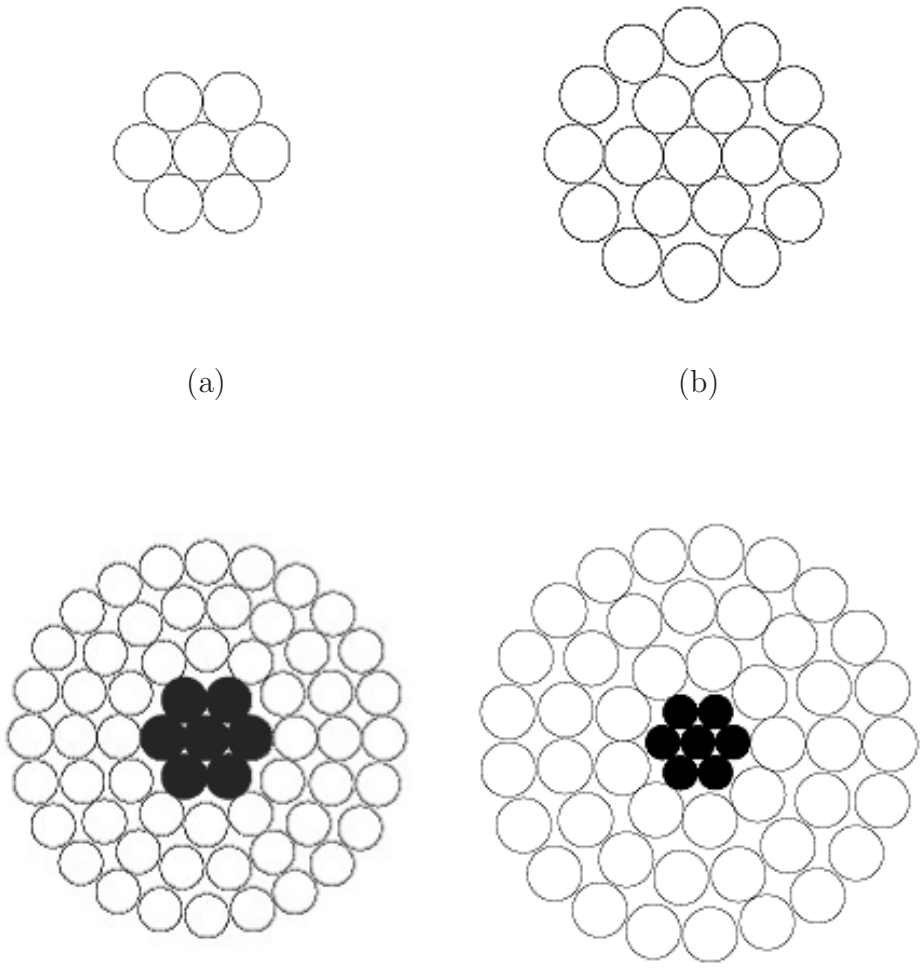

(a) (b)

(c) (d)

Figure 2.2: Cross section of power line samples. (Shaded parts represent steel strands.)(a)Power line #1 (b)Power line #2 (c)Power line #3 (d)Power line #4

Table 2.1: Geometrical specifications of the power lines

No.	Al/Copper		Steel		D [cm]	P [cm]	L [cm]
	# of St.	d [cm]	# of St.	d [cm]			
1	7	0.400	-	-	1.20	14.60	1.95
2	19	0.446	-	-	2.22	23.5	1.52
3	54	0.337	7	0.337	3.01	35.56	2.00
4	45	0.446	7	0.301	3.52	40.65	2.40

2.2 Experimental Setup

Polarimetric backscatter measurements of the power line samples were performed at 94 GHz using the University of Michigan millimeter-wave fully polarimetric radar system. This radar is a stepped frequency radar capable of transmitting a linear chirped signal with a bandwidth of 1 GHz and can be operated either in coherent or coherent-on-receive modes [45]. For the measured results reported in this study the coherent mode was used. Significant isolation between the transmit and receive channels are achieved using two separate antennas for the transmitter and receiver. However the transmitter antenna has a wider beamwidth to minimize parallax problem and the targets are positioned far enough from the radar so that the radar measurements are nearly in the backscatter direction. The block diagram of the measurement setup for collecting polarimetric RCS data is shown in Figure 2.3. The core of the system is an

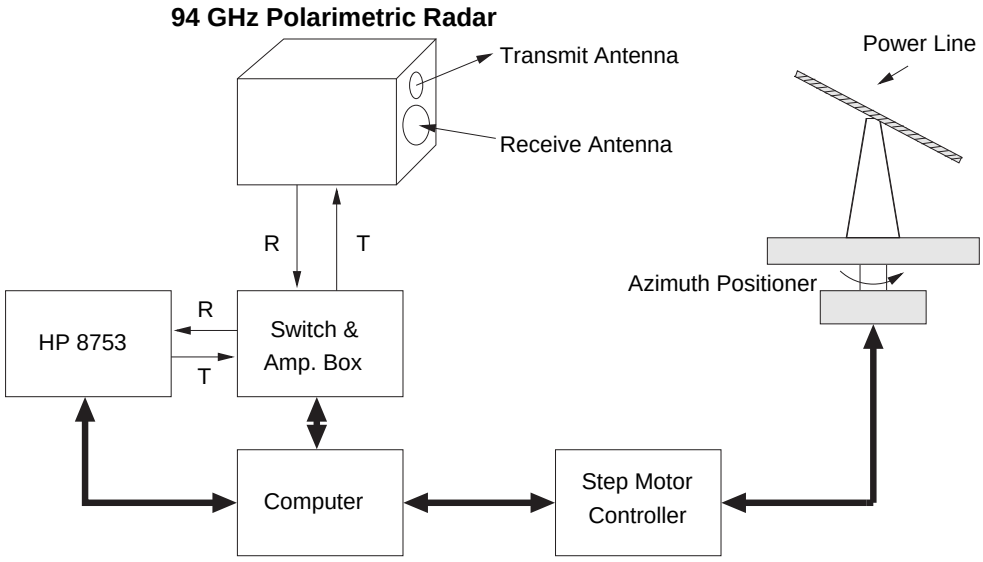

Figure 2.3: Measurement setup.

HP-8753C vector network analyzer with both phase and amplitude measurement capability and a 100 dB dynamic range. The ability of the network analyzer to generate the time domain response from the frequency response allows removal of unwanted signals from the desired target response. To measure the backscatter response of the power line samples with high signal to background ratio for all incident angles, the power lines were mounted on a U-shaped Styrofoam structure which is designed for very low radar backscatter response at the target range. The polarimetric radar cross section of the mount was measured for the angular range -10° to 50° with 0.1° steps. It was observed that the RCS level of the mount never exceeded -45 [dBsm] for all polarizations and aspect angles. To further reduce the backscatter from the mounting

structure, the backscatter from the mount was coherently subtracted from that of the target and the mount. To facilitate backscatter measurement at different incident angles a precision computer controlled turntable with an accuracy of a fraction of a tenth of a degree was used.

One important issue in polarimetric RCS measurements is the calibration. In this procedure the systematic errors, such as channel imbalances and antenna cross-talks are removed and the data is radiometrically scaled. The measured polarimetric data are calibrated using a 7.6-cm metallic sphere and a depolarizing target according to the procedure outlined in [45]. It should be noted here that since power lines are targets of infinite extent (their length are usually larger than the antenna footprint) radiometric calibration is not well defined because of the magnitude and phase variation of the antenna footprint over the target. Hence the absolute radiometric calibration is not possible and the measurements are system dependent. The RCS values reported in this Chapter are obtained assuming the power line is a point target located at the antenna boresight. The accuracy of the calibration technique has been determined to be ± 0.5 dB in magnitude and $\pm 5^{\circ}$ in phase [45]. To ensure the accuracy of the measured results the calibration procedure was performed at the beginning and at the end of each power line measurement.

Backscatter response of a power line is mainly characterized by the size and arrangement of the outer layer of the constituent strands. Four typical power line samples were selected. Figure 2.1 shows the geometry of a typical power line and Figure 2.2 shows the cross section of the power line samples. In the Figure, the shaded parts represent the steel strands. The conducting wires are wound around a core in a

helical fashion forming a periodic structure. It should be noted that the periodicity of the structure is smaller than the pitch of the helix and depends on the number of strands on the outer layer. The structural information and dimensions of the four different power lines used in these experiments are listed in Table 2.1. The diameters of the power lines range from 1.2 cm to 3.52 cm and their stand diameters vary from 0.34 cm to 0.45 cm. As is shown in Table 2.1, the surface period of these power lines, varying from 1.2 cm to 3.52 cm, depends on the pitch, stand diameter, and the number of strands on the outer layer. The power lines used in the RCS measurements were about a meter long positioned at about 12 meters from the radar system. The half-power-beam-width (HPBW) of this radar is 1.4° producing a footprint of about 30 cm at the target position. The cable lengths, and the target distance are chosen so that there is no considerable radar backscatter from the power lines ends.

The targets were positioned in the horizontal plane, and their radar backscatter responses were measured in the radar antenna principal plane. This configuration is similar to that of a radar system on low-flying aircraft heading towards a power line in the horizontal plane. Angular RCS measurements were performed by rotating power lines in the principal plane. In cases where the power line is not in the principal plane, circular symmetry of the power line can be used to obtain the scattering matrix of the power line from those measured in the principal plane. Once scattering matrix of a power-line is known in principal plane, scattering matrix in any arbitrary plane can be obtained from

$$\begin{aligned} \mathbf{S} &= \begin{bmatrix} S_{vv} & S_{vh} \\ S_{hv} & S_{hh} \end{bmatrix} \\ &= \begin{bmatrix} \cos\psi & -\sin\psi \\ \sin\psi & \cos\psi \end{bmatrix} \mathbf{S}_p \begin{bmatrix} \cos\psi & \sin\psi \\ -\sin\psi & \cos\psi \end{bmatrix} \end{aligned} \tag{2.1}$$

where $\mathbf{S}_p$ is the scattering matrix of the power-line in the principal plane. The coordinate frame rotation, ψ is given as following equation by the incident angle(θ) and polar direction(ϕ) of the power-line axis.

$$\psi = \tan^{-1}\left[\cos\theta \tan\phi\right] \tag{2.2}$$

In addition to power line samples, the radar backscatter responses of four smooth metallic cylinders having lengths and diameters identical to those of the power lines were measured to identify the effects of braiding on the polarimetric backscatter response. The power lines and cylinders were measured over the angular range -10 to 50 degrees with a fine angular resolution (steps of 0.1 degrees). To reduce the noise floor of the system, 8 traces at each target position were acquired and averaged coherently. The backscatter measurement for each power line was repeated to ensure measurement consistency.

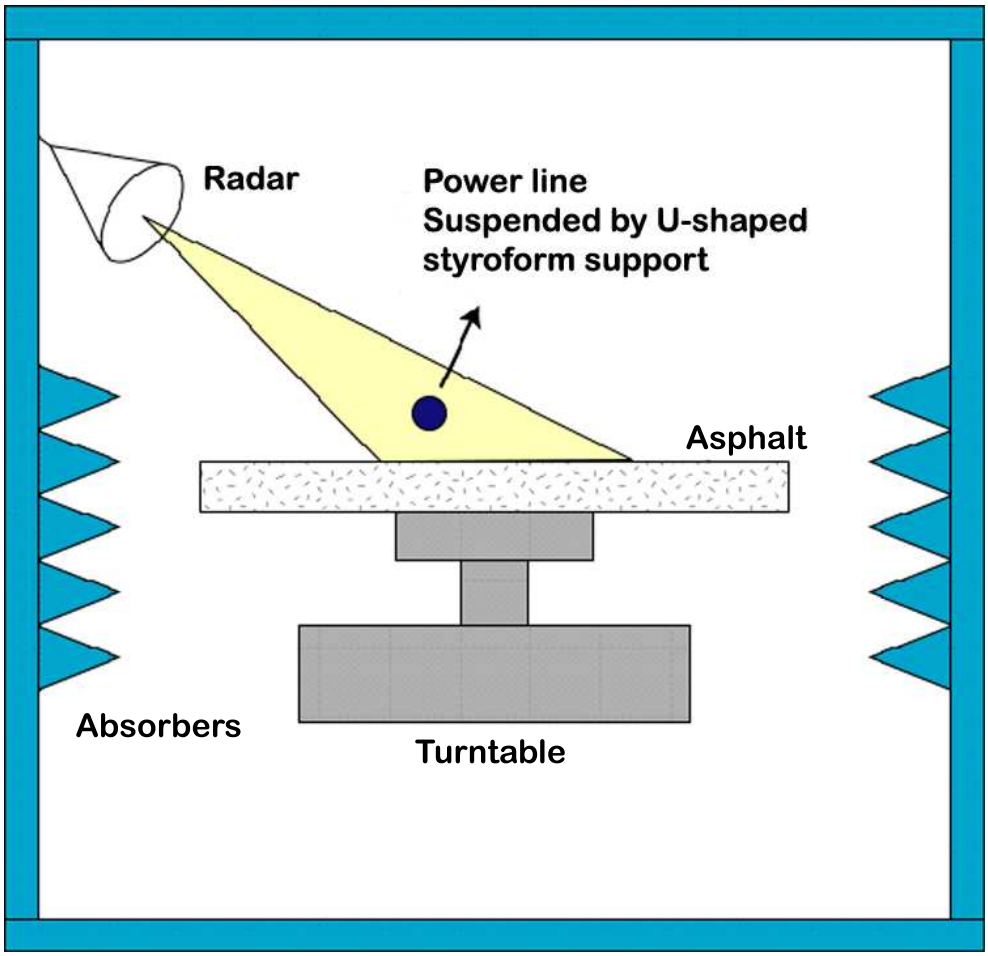

Figure 2.4: Measurement setup for power line with asphalt as background clutter.

Figure 2.5: Power line #4 in a background clutter(Douglas fur tree).

2.3 Experimental Results

In this section a summary of the polarimetric backscatter behavior of power lines is given. As mentioned earlier, backscatter of the power line samples were determined experimentally under three different surface conditions : dry, wet, and frozen. Figures 2.6(a)-2.6(f) show the polarimetric radar backscatter responses of the four power lines and two smooth cylinders under dry surface conditions. Comparing Fig-

ures 2.6(a) and 2.6(b) with Figures 2.6(e) and 2.6(f) significant differences between the backscatter response of power lines and their counterpart smooth cylinders are seen. Cylinder backscatter exists only at normal incidence and no cross-polarized backscatter is generated whereas power lines generate considerable backscatter in all polarizations and over a wide range of incidence angles. Strong backscatter peaks occur at normal incidence and at certain discrete incidence angles. These peaks are known as Bragg modes in the backscatter direction caused by the constructive interference of backscatter from each period of the power line surfaces. At millimeter-wave frequencies where $d > \lambda$, the periodic structure produces significant backscatter at

$$\theta_n = \sin^{-1}\left(\frac{n\lambda}{2L}\right) \tag{2.3}$$

where λ is the wavelength and L is the period. The measurements show that the Bragg scattering ceases to exist at incident angles larger than 15°. This corresponds to incidence angles beyond which specular points on the power line surface disappear [4]. But, there are still considerable co- and cross-polarized backscatter for power lines #2, #3, and #4 at incidence angles larger than 15°. This is attributed to the fact that power line #1 is geometrically more accurate than the others since the number of constituent strands are far fewer than the rest and the copper strands are very tightly wound together. The strands of the outer layer of power lines #2–#4 are aluminum and are somewhat loose creating a quasi-periodic surface. The degree of disorder increases with the increase in the number of strands and therefore the backscatter level of power line #4 at high incidence angles is higher than the others. This is also demonstrated using a numerical analysis [29]. Important

characteristics of power line backscatter behavior are summarized as follows. At the off-specular angles, σ_{vv} is much stronger than the backscatter at other polarizations and increases with increasing the cable diameter D and strand diameter d. At Bragg directions co-polarized backscatters are much stronger than the cross-polarized component, however, at higher incidence the cross-polarized component is stronger than σ_{hh} and weaker than σ_{vv}. The dominance of σ_{vv} at large incidence angles may be attributed to the almost horizontal grooves on the surface of power lines. It is shown that transverse electric (TE) electromagnetic waves (in this case vertical polarizations) can couple into the horizontal grooves (a TEM wave is formed in the groove) whereas for a TM wave (horizontal polarization) the grooves behave as waveguide operating below cutoff frequencies. [49]. For the most part, the co-polarized RCS can be attributed to single reflection from the power line surface. On the other hand the cross-polarized component is predominantly generated by the multiple reflections from the adjacent strands. Basically the grooves on the power line surface support dihedral type double reflections. It is known that tilted dihedral can generate strong cross-polarized backscatter [48].

The polarimetric backscatter responses of the power lines were also measured under wet surface condition to investigate the effect of a water layer on the power lines. To maintain the wetness condition throughout the RCS measurements, the power lines were sprayed with water frequently. The backscatter of the wet and dry power lines at vertical polarization are compared in Figures 2.7(a)-2.7(d). The results show that for the thin power line, the RCS is increased at high incidence angles when the surface is made wet and for other power lines the RCS decreased slightly. Similar

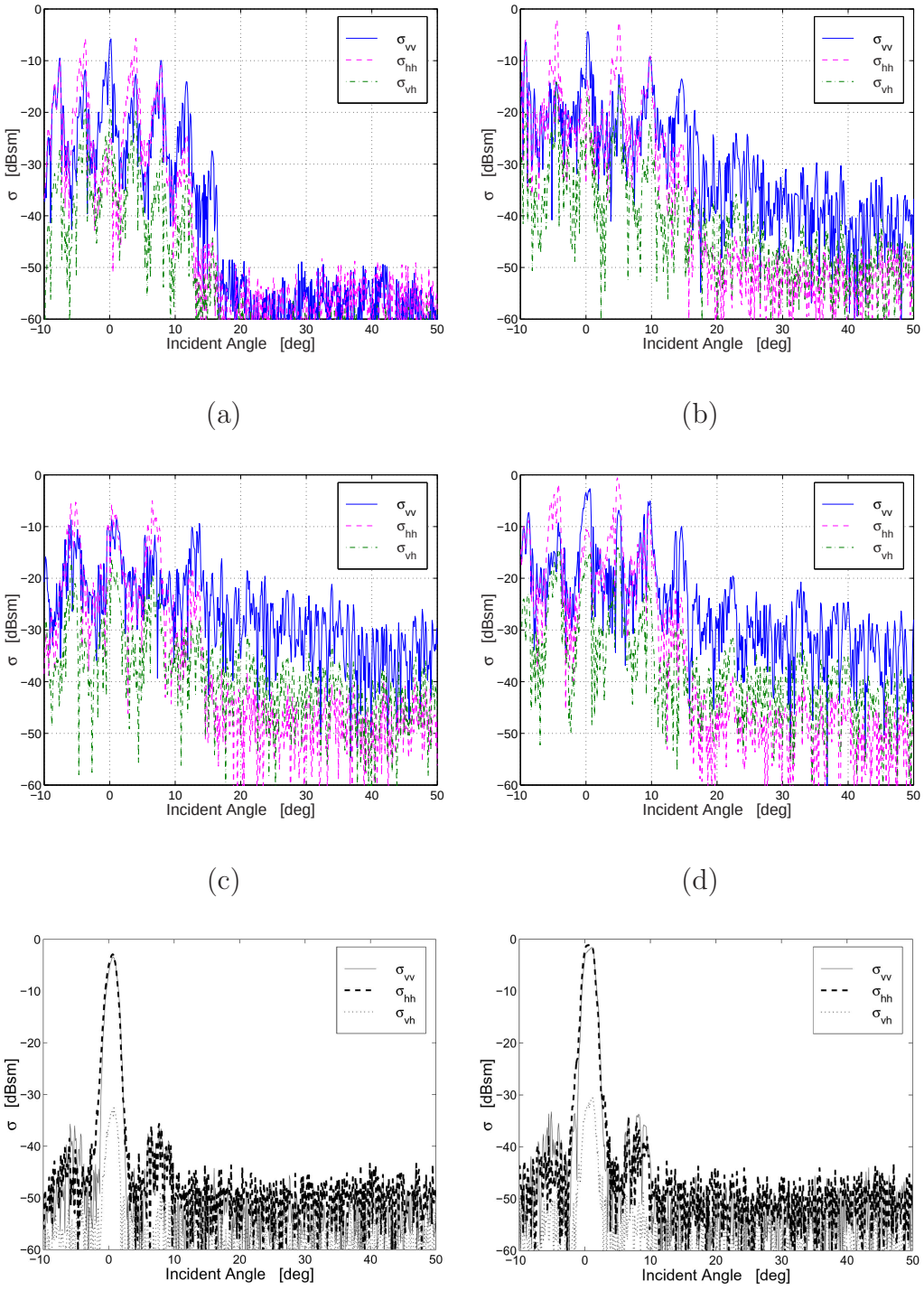

Figure 2.6: Polarimetric backscatter responses of the four power line samples used in this study and two cylinder counterpart of power line #1 and #2. (a)power line #1 (b)power line #2 (c)power line #3 (d)power line #4 (e)Cylinder #1 (f)Cylinder #2

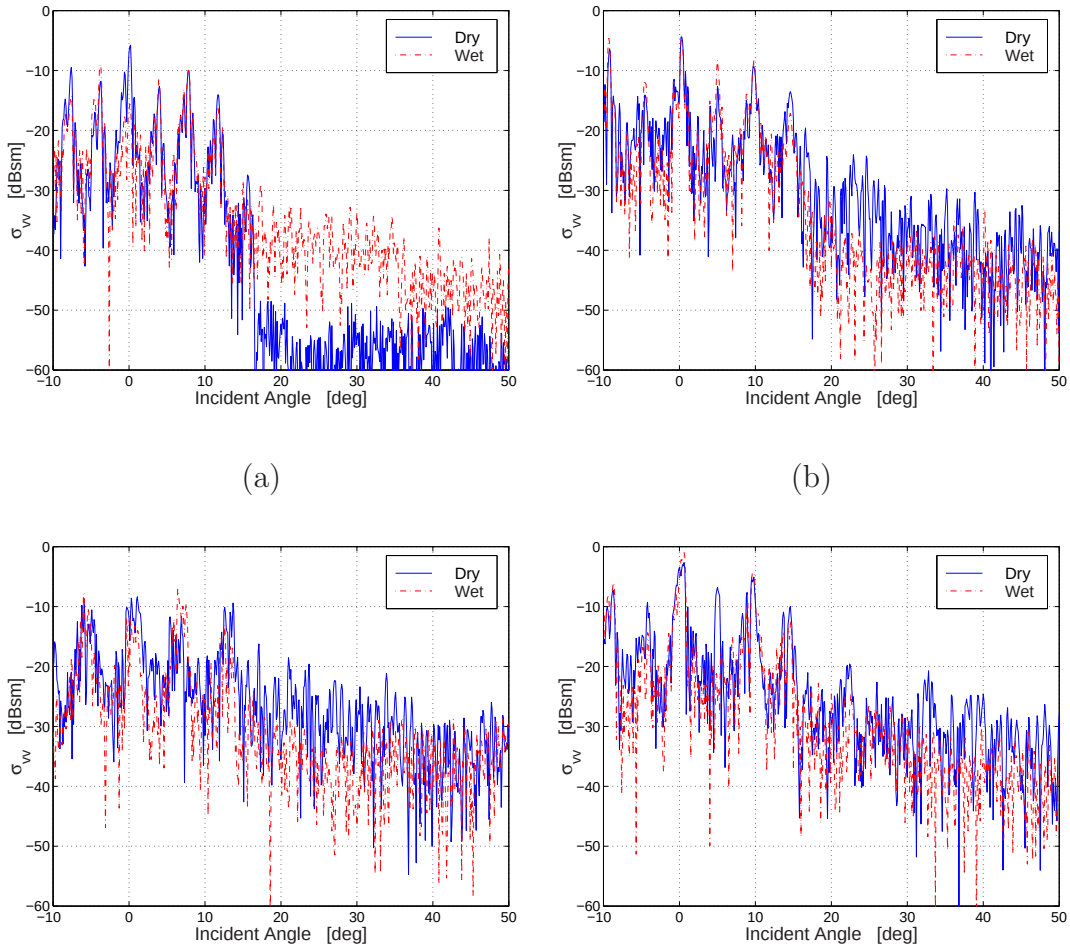

Figure 2.7: VV-polarized backscatter responses of the four power line samples covered with a thin layer of water. (a)power line #1 (b)power line #2 (c)power line #3 (d)power line #4

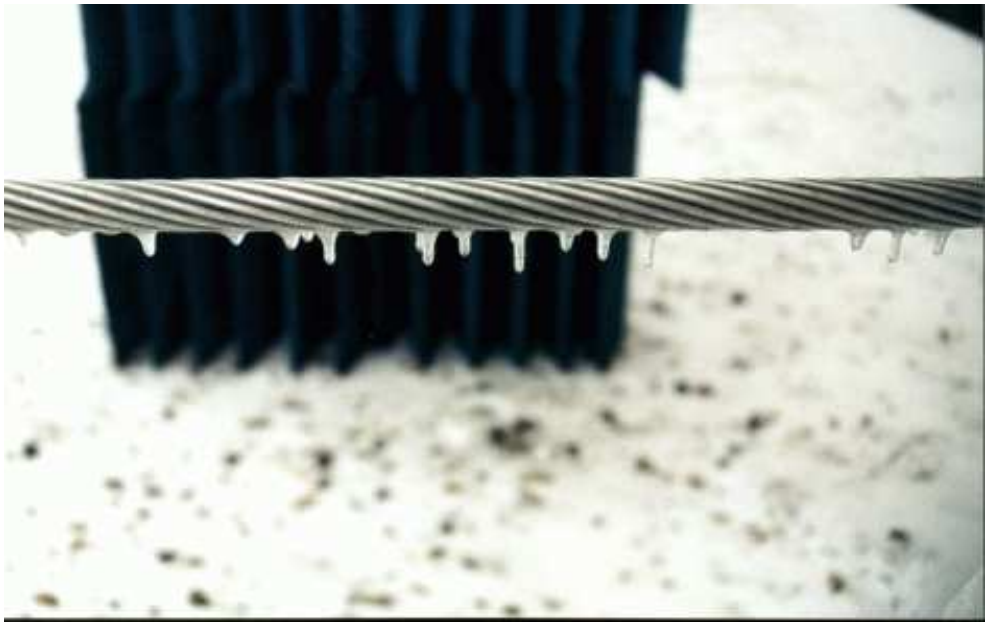

Figure 2.8: A picture of power line #2 covered with a layer of ice(thickness $\approx$ 1 mm) during the backscatter measurements.

results were obtained for other polarizations as well. It was also noticed that when the cracks between the wire strands are filled with water the backscatter RCS is reduced considerably. The latter case can only happen under continuous and relatively heavy rain as the power line structures cannot retain the water.

To complete the experimental aspects of the radar phenomenology of power lines, polarimetric backscatter measurements of the samples covered with a layer of ice were also performed. The radar and target positioner were set up outdoor during a very cold day. The surface of the power lines were sprayed with water and let to freeze. A layer of ice with an average thickness of about 1 mm was formed on the surface of the lines. Due to gravitational force on dripping water some short icicles were also formed

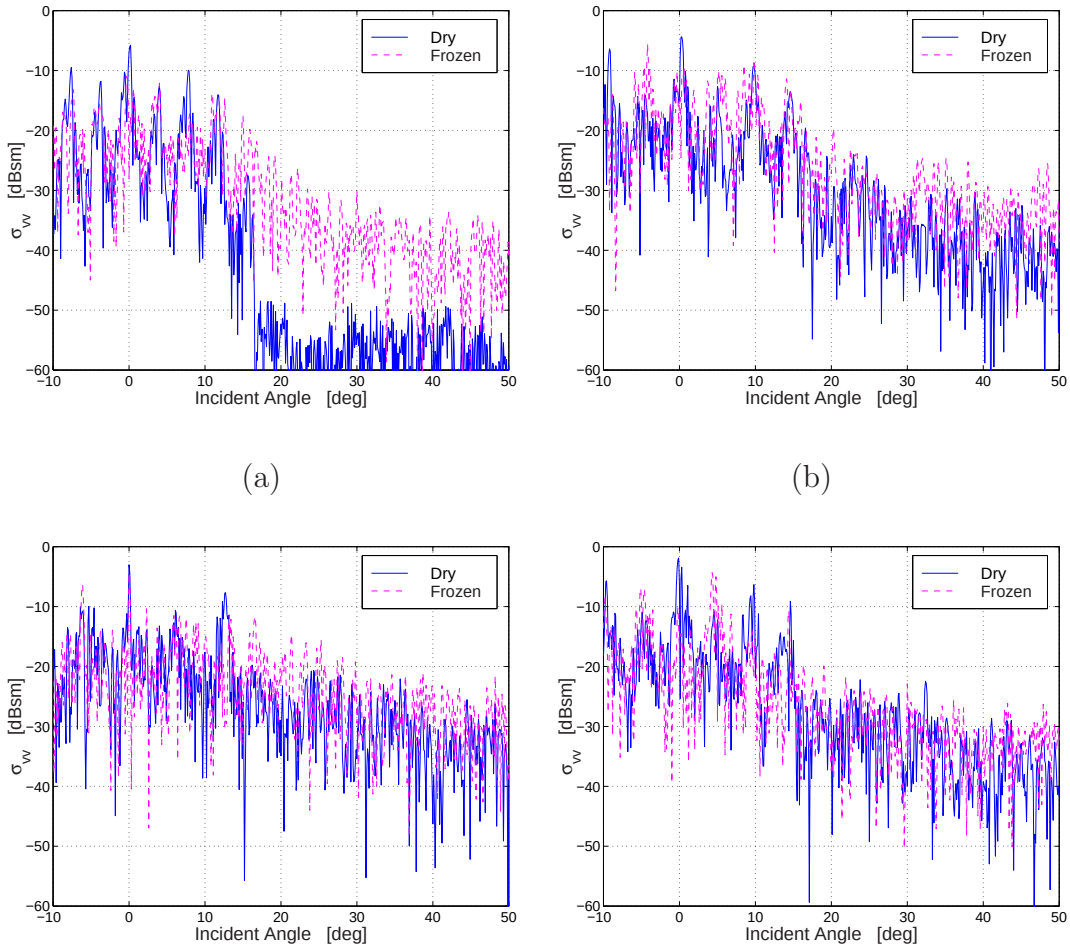

Figure 2.9: VV-polarized backscatter responses of the four power line samples covered with a layer of 1–mm–thick ice. (a)power line #1 (b)power line #2 (c)power line #3 (d)power line #4

on the lower surface of horizontal power line samples. Figure 2.8 shows the picture of an ice-covered power line used in the backscatter measurements. It is found from the measured results that the RCS of ice-covered power lines are slightly lower than the RCS of dry power lines at angles close to normal incidence (less than 15°) but the RCS increased for higher angles of incidence as shown in Figures 2.9(a)-2.9(d). This behavior was observed for all the power line samples and for all polarization configurations (VV, VH, and HH). In general, water and ice layers modify the RCS by modifying the surface reflectivity and effective surface roughness. As mentioned before, a layer of ice or water lowers the RCS level by few decibels for low incidence angles and increases the RCS level at high incidence angles. Hence it can be concluded that the probability of detection is not significantly affected when the cable is covered with a layer of water or ice.

As will be discussed in the next section, the proposed detection algorithm relies on the coherence between co- and cross-polarized backscatter of power lines. For ideal situations, that is, perfect power line structure and fixed incident angle, the backscatter is deterministic and therefore the co-and cross-polarized backscatter are perfectly correlated. However, in practice, there are imperfections in the structure and slight variations in incidence angle due to the radar antenna pattern. Hence it is important to examine the coherence between co- and cross-polarized backscatter by measuring the polarimetric backscatter statistics. The backscatter statistics are generated by moving a relatively small footprint (about 30 cm) over a long piece of power line and rotating the power line about its axis while keeping the aspect angle almost constant. Histograms are generated from 50 independent measurements and

six different aspect angles. The phase and magnitude of the co- and cross-polarized backscatter at 30° incidence are shown in Figure 2.10(a) and 2.10(b). Although there are fluctuations in the magnitude and phase of σ_{vv} and σ_{vh}, the fluctuations are almost perfectly correlated. The histograms of the magnitude and phase of $S_{vv}S_{vh}^{*}$ are also shown in Figures 2.10(c), 2.10(d).

2.4 Detection algorithm

Detection of power lines using a conventional W-band radar seems only possible over narrow aspect angles where Bragg modes exist. In this situation, there may be enough signal-to-clutter ratio for detecting power line. However, at angles where there exists no strong backscatter from the power line, signal-to-clutter ratio is very low and conventional radar systems would fail to detect power lines. In practice the backscatter from background vegetation or rough surfaces, within the same range as the power line, may drastically exceed the backscatter from the power line itself. This was the reason for abandoning the idea of using conventional non-polarimetric millimeter wave radars for power line detection. To circumvent this difficulty, we resorted to radar polarimetry and a statistical detection algorithm for improving the signal-to-clutter ratio.

Theoretical and experimental investigations show that the co- and cross-polarized component of backscatter of distributed targets with azimuthal symmetry are statistically uncorrelated[32]. In other words $\langle S_{vv}S_{vh}^{*}\rangle$ and $\langle S_{hh}S_{vh}^{*}\rangle$ vanishes for almost all distributed targets provided that footprint is much larger than the field correla-

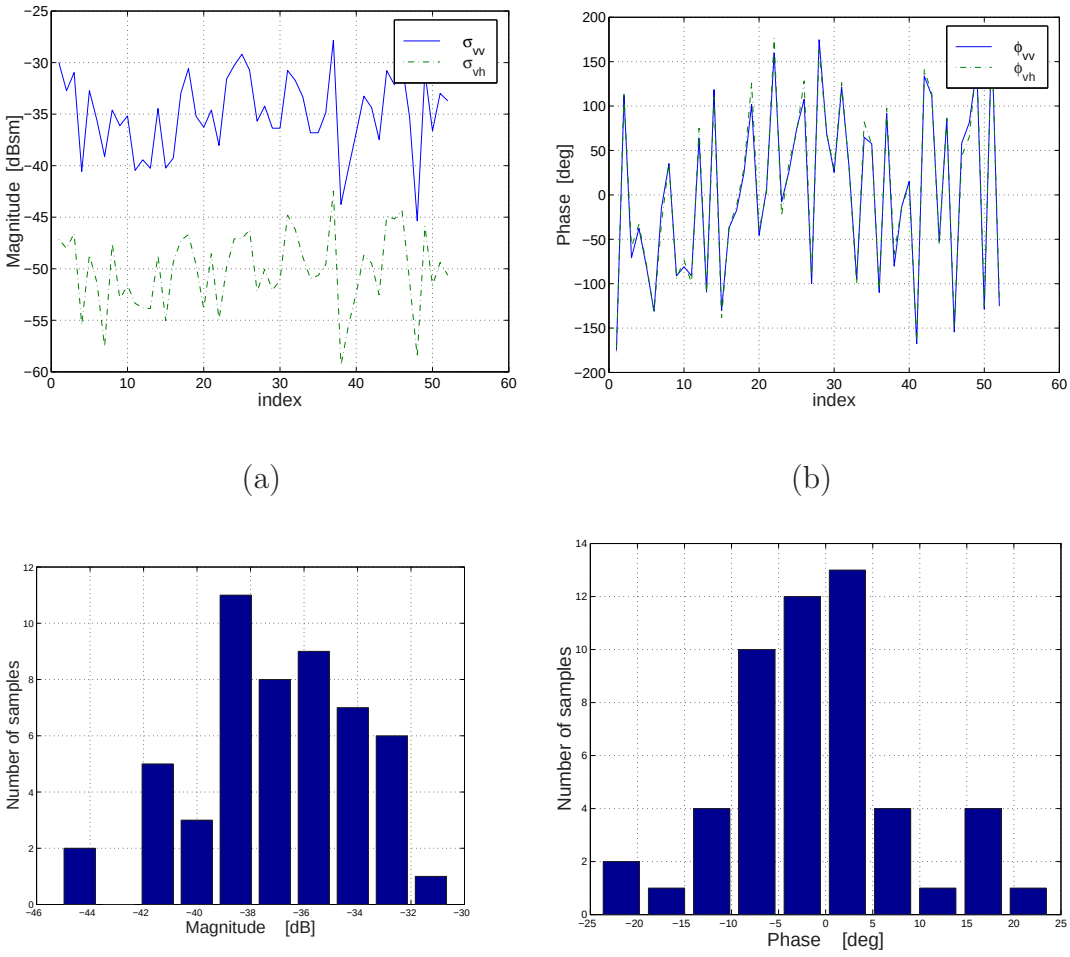

(a) (b)

(c) (d)

Figure 2.10: Coherence test of a power line #4 at incident angle 30°. Magnitude(a) and phase(b) fluctuations as a function of independent measurements for VV and VH backscatter. Also shown is the magnitude(c) and phase(d) of $S_{vv}S_{vh}^{*}$.

tion length in the random medium. However, as shown in the previous section, for power lines $\langle S_{vv}S_{vh}^{*}\rangle$ does not vanish. Measuring $\langle S_{vv}S_{vh}^{*}\rangle$, instead of $\langle S_{vv}S_{vv}^{*}\rangle$ for example, should improve detection probability drastically. For example, if a radar with sufficient fine range resolution is used, then for any given direction a relatively large number of independent backscatter measurements can be gathered that would allow for estimating $\langle S_{vv}S_{vh}^{*}\rangle$. Radar backscatter of power lines in the presence of a distributed target whose backscatter is much higher than that of the power line alone were measured and the algorithm was applied to the gathered data for four different aspect angles. Two distributed targets were chosen. One was a Douglas fur tree and the other was an asphalt surface. The statistics of the RCS of the distributed targets alone were obtained by rotating the targets. The statistics of the RCS of the power lines with a clutter background were obtained by positioning the power line at a desired aspect angle on a fixed platform and rotating the distributed target (see Figure 2.4 and Figure 2.5). For the incident angles which are larger than 20°, RCS of the clutter was found to be much larger than that of the power line alone. For these situations, any conventional detection algorithm fails to detect the power line. Ensemble averaging was achieved by rotating the distributed target (121 angles) and using frequency decorrelation of backscatter response over a 1 GHz bandwidth used in these experiments. Figure 2.4 and Figure 2.5 show the measurement setup used to generate the statistics of the backscatter response of the distributed target and the power line. Table 2.2 shows the backscatter power for three conventional polarizations (σ_{vv}, σ_{vh}, σ_{hh}) and the covariance between VV and VH of the tree alone and the tree plus the power line at four different aspect angles. (0°, 10°, 20°, and 30°) The

Table 2.2: The backscatter power in conventional channels and the ensemble averages of co- and cross-polarized response of a Douglas fur tree and power line #4.

	$\langle S_{vv}S_{vv}^* \rangle$	$\langle S_{vv}S_{vh}^* \rangle$	$\langle S_{vh}S_{vh}^* \rangle$	$\langle S_{hh}S_{hh}^* \rangle$
Tree alone	-20.6	-42.3	-27.5	-21.2
Tree & power line(0 deg)	-2.4	-8.7	-14.7	-17.4
Tree & power line(10 deg)	-8.7	-16.6	-23.3	-12.3
Tree & power line(20 deg)	-21.0	-30.1	-29.9	-23.1
Tree & power line(30 deg)	-22.2	-31.5	-29.9	-23.1

Table 2.3: The backscatter power in conventional channels and the ensemble averages of co- and cross-polarized response of asphalt and power line #4.

	$\langle S_{vv}S_{vv}^* \rangle$	$\langle S_{vv}S_{vh}^* \rangle$	$\langle S_{vh}S_{vh}^* \rangle$	$\langle S_{hh}S_{hh}^* \rangle$
Asphalt alone	-29.8	-43.0	-36.5	-32.9
Asphalt & power line(0 deg)	-12.9	-20.8	-27.6	-19.3
Asphalt & power line(10 deg)	-21.7	-30.8	-34.6	-23.8
Asphalt & power line(20 deg)	-25.1	-32.6	-34.3	-33.3
Asphalt & power line(30 deg)	-27.8	-35.6	-35.2	-33.4
Asphalt & power line(40 deg)	-29.4	-36.6	-35.8	-33.7

first two angles were chosen along the Bragg directions where there are significant backscatter and the other two angles were chosen where there are weak backscatter from the power line itself. It is obvious that along the Bragg directions, the power line can easily be detected. However, at other angles the backscatter in conventional channels are far below the clutter (signal-to-clutter ratio < -10 dB). The ensemble average of the cross product for the distributed target alone is of the order of -43 dB whereas $\langle S_{vv} S_{vh}^{*} \rangle$ for the power line and the tree is around -31dB which is 12 dB higher than the tree alone. Similar results were obtained when a rough asphalt surface was used as the clutter and the results are shown in Table 2.3.

2.5 Conclusions

In this chapter, polarimetric radar backscatter measurements of typical power line samples were performed and the effect of braiding on the backscatter response was investigated. The effects of a layer of water or ice on the polarimetric backscatter response were also investigated. It was shown that significant Bragg backscatter exists only for incidence angles below 15°. It was also shown that considerable backscatter exist in VV and VH channels at larger incidence angles which is mostly generated by the geometrical imperfections of power line structures. Based on the observed behavior of the polarimetric backscatter responses, a polarimetric detection algorithm was developed using the existence of correlation between VV and VH backscatter from power lines. The validity of the algorithm for detecting power lines in a strong clutter background was demonstrated under laboratory conditions. The result indicates that for sufficiently large number of independent samples, it is possible to improve the signal-to-clutter ratio by a factor of 20 dB.

CHAPTER 3

A RADAR CROSS SECTION MODEL FOR POWER LINES AT MILLIMETER-WAVE FREQUENCIES

3.1 Introduction

High voltage power lines and their supporting towers are considered as a major safety hazard for helicopters and other low flying aircrafts. Because of their low observability, in the U.S. alone, tens of helicopter collisions with power lines are reported [1]. To prevent these accidents, development of small size, low cost, millimeter-wave collision avoidance radar system is being considered. In Chapter 2, we proposed a detection algorithm that makes use of polarimetric backscatter statistics of distributed targets and power lines at W–band frequencies. To examine the performance of such algorithms, a thorough knowledge of scattering behavior of different power lines with different structural parameters such as strand arrangements and strand diameter is

needed. Such comprehensive RCS characterization experimentally seems very difficult if not impossible. The literature concerning analytical evaluation of RCS of power lines are limited to simple models proposed by Rembold [5], and Al–Khatib [4]. Rembold used long wire (smooth cylinder) model which is valid only at microwave frequencies (X-band and below). On the other hand the model developed by Al–Khatib is a very high frequency model based on geometrical optics (GO) approximation. Unlike Rembold's model the GO model is able to account for the effect of periodic structure of power lines. Using this model, Al–Khatib was able to predict the existence and locations of Bragg backscatter generated by the power line structure. Due to the fundamental limitations in GO approximation, this model is incapable of predicting the cross–polarized backscatter and differentiating the possible differences that may exist between the co–polarized backscatter (S_{vv} and S_{hh}) responses.

Because of its simplicity, Physical Optics (PO) model is widely used for the analysis of RCS of complex targets at high frequencies. Like GO, PO approximation is valid at high frequencies and cannot predict the cross–polarized backscatter for perfectly conducting targets. However, the concept of tangent plane approximation used in the PO approximation may be employed repeatedly to get more accurate results. The induced electric current on the surface of a perfectly conducting (PEC) body is proportional to the total tangential magnetic field. In the PO approach, the induced current is approximated by $\mathbf{J}_{po} = 2\,(\hat{n} \times \mathbf{H}_i)$ where $\mathbf{H}_i$ is the incident magnetic field. The field produced by this current does not include the effect of multiple scattering which gives rise to cross–polarized backscatter. Experimental results show [8, 30] that at high frequencies (W–band and higher) the effect of multiple scattering on the

surface of power lines becomes significant. The so–called multiple scattering is caused by the periodic helical arrangement of wire strands. From a simple geometrical optics point of view the existence of cross–polarized backscatter caused by multiple scattering can be attributed to the tilted dihedral shape grooves that exist between adjacent wire strands. Accurate polarimetric backscatter behavior of power line structure can be determined by resorting to numerical full–wave analysis. In Section 3.2 an integral equation for the induced surface current density is derived that makes use of a periodic dyadic Green's function. This integral equation is than used as a basis for the iterative PO model. In Section 3.3 the formulation for the iterative PO model is described where the traditional PO current is used as a source of radiation for computing the second order PO current on the surface. The iterative PO model allows for prediction of angular RCS response of power lines when illuminated by plane waves and spherical waves. Numerical simulations and comparison with measurements at W–band frequencies are presented in Section 3.4. Also the effect of irregularities on the periodic arrangements of strands on the RCS is examined.

3.2 Formulation of Dyadic Green's Function for Power Lines

The geometry of a power line and its associated coordinate system is shown in Figure 3.1. Let us consider a plane wave propagating along $\hat{k_i} = k_{xi}\hat{x} + k_{yi}\hat{y} + k_{zi}\hat{z}$

direction whose electric field is represented by

$$\mathbf{E}^i = \hat{p} e^{ik_0 \hat{k_i} \cdot \mathbf{r}} \tag{3.1}$$

where $\hat{p}$ denotes the polarization vector. Since the incident field is plane wave and the surface of the power line is periodic along z-axis, the induced surface electric current distribution is also periodic except for a progressive phase factor $e^{ik_0 k_{iz} z}$. Hence the current on the nth period can be expressed in terms of the current on the period near the origin as:

$$\mathbf{J}(\mathbf{r}'_n) = \mathbf{J}(\mathbf{r}'_0) e^{ik_0 k_{iz} nL} \tag{3.2}$$

where L is the period and

$$\mathbf{r}'_n = \mathbf{r}'_0 + nL\hat{z}. \tag{3.3}$$

Subdividing the surface of the scatterer into infinite number segments each having a length L, the total scattered field can be computed using the free–space Green's function and is given by

$$\mathbf{E}^s(\mathbf{r}) = ik_0 Z_0 \sum_{n=-\infty}^{+\infty} \int_{S_n} \bar{\bar{\mathbf{G}}}(\mathbf{r}, \mathbf{r}'_n) \cdot \mathbf{J}(\mathbf{r}'_n)\, d\mathbf{r}'_n \tag{3.4}$$

where $\mathbf{r}'_n \in S_n$ and Z_0 is the free–space intrinsic impedance. By inserting (3.2) and (3.3) into (3.4), and interchanging the order of integration and summation, (3.4) can be rewritten as

$$\mathbf{E}^s(\mathbf{r}) = ik_0 Z_0 \int_{S_0} \left[\sum_{n=-\infty}^{+\infty} \bar{\bar{\mathbf{G}}}(\mathbf{r}, \mathbf{r}'_0 + nL\hat{z}) e^{ik_0 k_{iz} nL} \right] \cdot \mathbf{J}(\mathbf{r}'_0)\, d\mathbf{r}'_0 \tag{3.5}$$

The quantity inside the bracket is the dyadic Green's function for periodic structures and is given by

$$\bar{\bar{\mathbf{G}}}_p(\mathbf{r}, \mathbf{r}') = (\bar{\bar{\mathbf{I}}} + \frac{1}{k_0^2} \nabla\nabla) \sum_{n=-\infty}^{+\infty} g(\mathbf{r}, \mathbf{r}'_0 + nL\hat{z}) e^{ik_0 k_{iz} nL} \tag{3.6}$$

where $g(\mathbf{r}, \mathbf{r}')$ is the free–space scalar Green's function given by

$$g(\mathbf{r}, \mathbf{r}') = \frac{1}{4\pi} \frac{e^{ik_0|\mathbf{r}-\mathbf{r}'|}}{|\mathbf{r}-\mathbf{r}'|}. \tag{3.7}$$

Expressing $g(\mathbf{r}, \mathbf{r}')$ in terms of its two–dimensional Fourier expansion and employing the identity

$$\frac{1}{\pi} \int_{-\infty}^{+\infty} \frac{e^{i[k_y(y-y')+k_{nx}|x-x'|]}}{k_{nx}} dk_y = H_0^{(1)} \left(k_0 \sin\theta_n \, |\vec{\rho} - \vec{\rho}'|\right) \tag{3.8}$$

where

$$k_{nx} = \sqrt{k_0^2 - \left(\frac{2\pi n}{L} + k_0 k_{iz}\right)^2 - k_y^2}$$

$$|\vec{\rho} - \vec{\rho}'| = \sqrt{(x-x')^2 + (y-y')^2}$$

$$\sin\theta_n = \sqrt{1 - (\frac{n\lambda}{L} + k_{iz})^2}$$

the periodic Green's function can be written as

$$\bar{\bar{\mathbf{G}}}_p(\mathbf{r}, \mathbf{r}') = (\bar{\bar{\mathbf{I}}} + \frac{1}{k_0^2} \nabla\nabla) \, g_p(\mathbf{r}, \mathbf{r}') \tag{3.9}$$

where

$$g_p(\mathbf{r}, \mathbf{r}') = \frac{i}{4L} \sum_{n=-\infty}^{+\infty} H_0^{(1)}(k_0 \sin\theta_n \, |\vec{\rho} - \vec{\rho}'|) e^{ik_0 \cos\theta_n (z-z')}. \tag{3.10}$$

The summation in (3.10) converges very rapidly as the argument of the Hankel function becomes pure imaginary for large values of n. The equation (3.9) can be written in a matrix form as

$$\bar{\bar{\mathbf{G}}}_p(\vec{r},\vec{r}') = \frac{i}{4L}\sum_{n=-\infty}^{+\infty} \begin{bmatrix} 1+\frac{1}{k_0^2}\frac{\partial^2}{\partial x^2} & \frac{\partial^2}{\partial x\partial y} & ik_0\cos\theta_n\frac{\partial}{\partial x} \\ \frac{\partial^2}{\partial x\partial y} & 1+\frac{1}{k_0^2}\frac{\partial^2}{\partial y^2} & ik_0\cos\theta_n\frac{\partial}{\partial y} \\ ik_0\cos\theta_n\frac{\partial}{\partial x} & ik_0\cos\theta_n\frac{\partial}{\partial y} & \sin^2\theta_n \end{bmatrix} \times e^{ik_0\cos\theta_n(z-z')}H_0^{(1)}(k_0\sin\theta_n\,|\vec{\rho}-\vec{\rho}'|) \tag{3.11}$$

where

$$\frac{\partial}{\partial x}H_0^{(1)}(k_0\sin\theta_n\,|\vec{\rho}-\vec{\rho}'|) = -k_0\sin\theta_n H_1^{(1)}(k_0\sin\theta_n\,|\vec{\rho}-\vec{\rho}'|)\frac{x-x'}{|\vec{\rho}-\vec{\rho}'|}$$

$$\frac{\partial}{\partial y}H_0^{(1)}(k_0\sin\theta_n\,|\vec{\rho}-\vec{\rho}'|) = -k_0\sin\theta_n H_1^{(1)}(k_0\sin\theta_n\,|\vec{\rho}-\vec{\rho}'|)\frac{y-y'}{|\vec{\rho}-\vec{\rho}'|}$$

$$\begin{aligned}\frac{\partial^2}{\partial x^2}H_0^{(1)}(k_0\sin\theta_n\,|\vec{\rho}-\vec{\rho}'|) = &-k_0^2\sin^2\theta_n H_0^{(1)}(k_0\sin\theta_n\,|\vec{\rho}-\vec{\rho}'|)\frac{(x-x')^2}{|\vec{\rho}-\vec{\rho}'|^2} \\ &-k_0\sin\theta_n H_1^{(1)}(k_0\sin\theta_n\,|\vec{\rho}-\vec{\rho}'|)\frac{(x-x')^2-(y-y')^2}{|\vec{\rho}-\vec{\rho}'|^3}\end{aligned}$$

$$\begin{aligned}\frac{\partial^2}{\partial y^2}H_0^{(1)}(k_0\sin\theta_n\,|\vec{\rho}-\vec{\rho}'|) = &-k_0^2\sin^2\theta_n H_0^{(1)}(k_0\sin\theta_n\,|\vec{\rho}-\vec{\rho}'|)\frac{(y-y')^2}{|\vec{\rho}-\vec{\rho}'|^2} \\ &-k_0\sin\theta_n H_1^{(1)}(k_0\sin\theta_n\,|\vec{\rho}-\vec{\rho}'|)\frac{(x-x')^2-(y-y')^2}{|\vec{\rho}-\vec{\rho}'|^3}\end{aligned}$$

$$\begin{aligned}\frac{\partial^2}{\partial x\partial y}H_0^{(1)}(k_0\sin\theta_n\,|\vec{\rho}-\vec{\rho}'|) = &-k_0^2\sin^2\theta_n H_0^{(1)}(k_0\sin\theta_n\,|\vec{\rho}-\vec{\rho}'|)\frac{(x-x')(y-y')}{|\vec{\rho}-\vec{\rho}'|^2} \\ &+2k_0\sin\theta_n H_1^{(1)}(k_0\sin\theta_n\,|\vec{\rho}-\vec{\rho}'|)\frac{(x-x')(y-y')}{|\vec{\rho}-\vec{\rho}'|^3}\end{aligned}$$

The scattered magnetic field can be obtained from (3.5) by taking curl of the electric field and is given by

$$\mathbf{H}^s(\mathbf{r}) = \int_{S_0} \nabla\times\,\bar{\bar{\mathbf{G}}}_p(\mathbf{r},\mathbf{r}')\cdot\mathbf{J}(\mathbf{r}_0')\,d\mathbf{r}_0'.$$

Noting that $\nabla \times \bar{\bar{\mathbf{G}}}_p(\mathbf{r},\mathbf{r}') = \nabla g_p(\mathbf{r},\mathbf{r}') \times \bar{\bar{\mathbf{I}}}$ and the induced electric current is proportional to the total tangential magnetic field, *i.e.* $\mathbf{J}(\mathbf{r}) = \hat{n} \times (\mathbf{H}^i + \mathbf{H}^s)$, a magnetic field integral equation for the current can be obtained and is given by:

$$\mathbf{J}(\mathbf{r}) = 2\left(\hat{n}(\mathbf{r}) \times \mathbf{H}^i(\mathbf{r})\right) + 2 \oint_{S_0} \left(\hat{n}(\mathbf{r}) \cdot \nabla g_p(\mathbf{r},\mathbf{r}')\right) \mathbf{J}(\mathbf{r}')\, d\mathbf{r}' \tag{3.12}$$

where S_0 specifies the surface of power line over one period and $\oint_{S_0}$ denotes the principal value integral. The explicit form of $\nabla g_p(\mathbf{r},\mathbf{r}')$ can easily be obtained and is given by

$$\begin{aligned} \nabla g_p(\mathbf{r},\mathbf{r}') &= \frac{ik_0}{4L} \sum_{n=-\infty}^{+\infty} \Big[-\sin\theta_n H_1^{(1)}(k_0 \sin\theta_n \,|\vec{\rho} - \vec{\rho}'|) \frac{(\vec{\rho} - \vec{\rho}')}{|\vec{\rho} - \vec{\rho}'|} \\ &\quad + i\cos\theta_n H_0^{(1)}(k_0 \sin\theta_n \,|\vec{\rho} - \vec{\rho}'|)\hat{z} \Big] e^{ik_0 \cos\theta_n (z - \hat{z})} \end{aligned} \tag{3.13}$$

Integral equation (3.12) can be solved numerically for the induced electrical current density $\mathbf{J}(\mathbf{r})$ using the standard method of moments. Once $\mathbf{J}(\mathbf{r})$ is determined the scattered electric field in the far–field region can be obtained from

$$\mathbf{E}^s(\mathbf{r}) = ik_0 Z_0 \int_{S_0} \bar{\bar{\mathbf{G}}}_{pf}(\mathbf{r},\mathbf{r}') \cdot \mathbf{J}(\mathbf{r}')\, d\mathbf{r}' \tag{3.14}$$

where $\bar{\bar{\mathbf{G}}}_{pf}(\mathbf{r},\mathbf{r}')$ is the far–field approximation of the periodic Green's function given by (3.9). The explicit expression for $\bar{\bar{\mathbf{G}}}_{pf}(\mathbf{r},\mathbf{r}')$ can be obtained by noting that $\nabla = \nabla_t + ik_0 \cos\theta_n \hat{z}$ and the fact that in far–field $\nabla_t \simeq ik_0 \sin\theta_n \hat{k}_\perp^s$ where

$$\hat{k}_\perp^s = \cos\varphi_s \hat{x} + \sin\varphi_s \hat{y}$$

denotes the direction of observation point. Hence

$$\begin{aligned} \bar{\bar{\mathbf{G}}}_{pf}(\mathbf{r},\mathbf{r}') &= \frac{i}{4L} \sum_{n \in N} \Big[\bar{\bar{\mathbf{I}}} - \sin^2\theta_n \hat{k}_\perp^s \hat{k}_\perp^s - \sin\theta_n \cos\theta_n (\hat{k}_\perp^s \hat{z} + \hat{z}\hat{k}_\perp^s) - \cos^2\theta_n \hat{z}\hat{z} \Big] \\ &\quad \cdot H_0^{(1)}(k_0 \sin\theta_n \rho) e^{ik_0 \cos\theta_n z} e^{-ik_0 (\sin\theta_n \vec{\rho}_0{}' \hat{k_s} + \cos\theta_n z')} \end{aligned} \tag{3.15}$$

where N denotes a set of integers for which $\sin\theta_n$ is real (these denote the observable bistatic Bragg directions). It should be emphasized that the far–field approximation (3.14) is valid so long as $\sin\theta_n \neq 0$.

3.3 Physical Optics Model

At low frequencies where typical dimensions of scatterers are comparable to or less than a wavelength, the integral equation given by (3.12) can be used to obtain an exact solution using the method of moments. But power lines are electrically large at 94 GHz and the numerical method would require exorbitant computer memory and computation time. For example, a power line with an overall diameter of 3.5 cm, surface periodicity of 2.4 cm, and strand diameter of 0.446 cm must be discretized into approximately 5×10^4 small patches which results in 2×10^5 unknowns (real and imaginary parts of two unknown surface current density) at 94 GHz. Implementation of MOM for this example is not possible with ordinary computers. Besides for studying the effects of non–uniform illumination and surface irregularities where periodic Green's function can no longer be used, the required computation time and computer memory would far exceed the existing computer capabilities. To alleviate this problem while maintaining a high degree of accuracy, an approximate solution based on physical optics is used. The iterative physical optics is applied using both the periodic and free–space Green's function. The periodic Green's function is appropriate for plane wave illumination assuming a perfect surface periodicity. It can also be used for scattered field evaluation when the power line is illuminated by a

non–uniform plane wave by expanding the incident field in terms of a continuous spectrum of plane waves and using superposition. The free–space Green's function allows the computation of RCS of power lines with quasi–periodic surface.

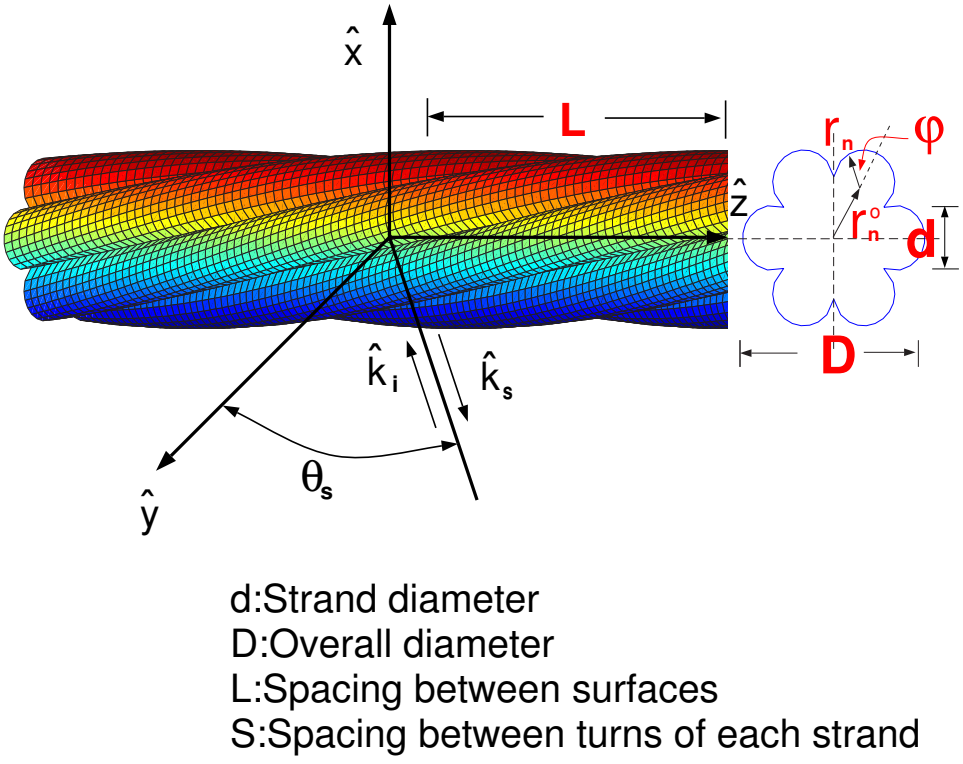

Figure 3.1: Geometry of a power line and its important parameters, $\hat{k}_i$ denotes the direction of incidence field.

Figure 3.1 shows the geometry of a typical power line in the principal plane of a radar antenna. As mentioned earlier a power line is made up of a number of steel strands (placed at the core) and aluminum wire strands with diameter d wound together in a helical fashion. Depending on the number of wires on the outer surface, the overall diameter of the cable (D), and the pitch of the helix (P), the period of the surface (L) can be determined. A mathematical description of the surface is needed for either MOM or iterative physical optics solution. Consider a power line with N strands at the outer surface (see Figure 3.1), after some inspections, a point on the surface of this cable may be represented by

$$\mathbf{r} = \mathbf{r}_o^n + \mathbf{r}_n \qquad n = 1, 2, ..., N \tag{3.16}$$

where

$$\mathbf{r}_o^n = \left(\frac{D-d}{2}\right)\cos\frac{2\pi n}{N}\hat{x} + \left(\frac{D-d}{2}\right)\sin\frac{2\pi n}{N}\hat{y} \tag{3.17}$$

$$\begin{aligned}\mathbf{r}_n \;=\; & \left(\frac{d}{2}\cos\frac{2\pi n}{N}\cos\varphi - \frac{d\sqrt{(\pi D)^2+P^2}}{2P}\sin\frac{2\pi n}{N}\sin\varphi\right)\hat{x} \\ & + \left(\frac{d}{2}\sin\frac{2\pi n}{N}\cos\varphi + \frac{d\sqrt{(\pi D)^2+P^2}}{2P}\cos\frac{2\pi n}{N}\sin\varphi\right)\hat{y}\end{aligned} \tag{3.18}$$

Here, as mentioned before, d, D, and P are strand diameter, cable overall diameter and the helix pitch respectively and φ is a parameter indicating the angle between $\mathbf{r}_n$ and $\mathbf{r}_0^n$. Finally the 3–D parametric representation of a power line can be represented as

$$R = \left[r_x\cos\frac{2\pi z}{P} - r_y\sin\frac{2\pi z}{P}, \quad r_x\sin\frac{2\pi z}{P} + r_y\cos\frac{2\pi z}{P}, \quad z\right] \tag{3.19}$$

where r_x and r_y are the x and y component of $\mathbf{r}$ respectively. Figure 3.1 shows the surface of a power line with 6 outer strands generated by equation (3.19). The

starting point in formulating the approximate numerical solution based on PO is the magnetic field integral equation given by (3.12). In this approximation the following observations are in order. Most power lines are wound in a manner so that $\frac{D}{P} \ll 1$, and therefore $\hat{n} \cdot \hat{z} \ll 1$. Also at high frequencies where the radius of curvature is larger than the wavelength the quantity $\hat{n} \cdot \frac{(\vec{\rho}-\vec{\rho}')}{|\vec{\rho}-\vec{\rho}'|} \ll 1$ for values of $\vec{\rho}'$ sufficiently close to $\vec{\rho}$. Hence the principal value integral in (3.12) is small compared to $\hat{n} \times \mathbf{H}^i$. Table 2.1 in Chapter 2 shows the geometrical parameters of various cables used in power distribution and transmission. To the zeroth order of approximation, the integral in (3.12), can be ignored which results in the traditional physical optics current ($\mathbf{J}(\mathbf{r}) \simeq \mathbf{J}_0(\mathbf{r}) = 2\,(\hat{n} \times \mathbf{H}^i)$). Expanding the surface current in terms of a perturbation series and using (3.12), it can be shown that

$$\mathbf{J}^{(n)}(\mathbf{r}) = 2 \oint\!\!\!\!\!\!\int_{S_0} [\,\hat{n}(\mathbf{r}) \cdot \nabla g_p(\mathbf{r}, \mathbf{r}')]\, \mathbf{J}^{(n-1)}(\mathbf{r})\, d\mathbf{r}' \tag{3.20}$$

where $\mathbf{J}^{(n)}$ is the nth order physical optics currents. To study the RCS of power lines for non–uniform illumination and/or when the surface is not perfectly periodic, (3.20) should be modified by replacing $g_p(\mathbf{r}, \mathbf{r}')$ with the free–space scalar Green's function $g(\mathbf{r}, \mathbf{r}') = \frac{1}{4\pi} \frac{e^{ik|\mathbf{r}-\mathbf{r}'|}}{|\mathbf{r}-\mathbf{r}'|}$ and the limit of the integral should be changed to include the entire lit area. The explicit expression for the higher order physical optics current when free–space scalar Green's function is used is given below.

$$\mathbf{J}^{(n)}(\mathbf{r}) = 2 \oint\!\!\!\!\!\!\int_{lit\ area} [\hat{n}(\mathbf{r}) \cdot (\mathbf{r} - \mathbf{r}')]\, (ik - \frac{1}{|\mathbf{r} - \mathbf{r}'|}) \frac{e^{ik_0|\mathbf{r}-\mathbf{r}'|}}{4\pi\,|\mathbf{r} - \mathbf{r}'|^2}\, \mathbf{J}^{(n-1)}(\mathbf{r})\, d\mathbf{r}' \tag{3.21}$$

Once the PO current to any desired order is obtained, the scattered field in the

far–field region can be obtained from

$$\mathbf{E}^s(\mathbf{r}) = \frac{ik_0 Z_0}{4\pi}\frac{e^{ikr}}{r}\int_{lit\ area}(\bar{\bar{\mathbf{I}}} - \hat{k}^s\hat{k}^s)\cdot\mathbf{J}(\mathbf{r})e^{-ik_0\hat{k}_s\cdot\mathbf{r}'}\,d\mathbf{r}' \tag{3.22}$$

The scattered field can be expressed in terms of the incident field by:

$$\mathbf{E}^s = \frac{e^{ik_o r}}{r}[\mathbf{S}]\,\mathbf{E}^i, \tag{3.23}$$

where [**S**] is the scattering matrix, from which the scattering cross section, σ, can be obtained. The scattering cross section is defined as:

$$\sigma_{ij} = 4\pi\,|S_{ij}|^2 \tag{3.24}$$

with $i, j = v, h$.

3.4 Numerical and Experimental Results

In this section, the validity of the proposed physical optics model is examined by comparing simulated results with backscatter measurements of different power line samples at 94 GHz. Also a sensitivity analysis is carried out to study the effects of different geometrical parameters of power lines. The backscatter experiments were conducted on four different power line samples whose parameters are listed in Table 2.1 of Chapter 2. The detailed experimental procedure and an extensive set of backscatter measurements of different power lines under varieties of physical conditions are reported in a recent paper by the authors [30]. Here we briefly describe the experimental setup. A stepped–frequency radar operating at 94 GHz was used to perform the backscatter measurements at a distance of about 12 m. The half–power beamwidth of the receive antenna is 1.4° which produce a footprint of about

30 cm at the target range. The systematic errors in the polarimetric backscatter measurements, which are caused by the antenna crosstalk and channel imbalances, are removed using a calibration procedure that uses two external calibration targets [45]. Since the length of power lines are larger than the extent of antenna footprint, the RCS values reported are functions of the radar parameters. The values reported here are obtained assuming that power line is a point target located at the antenna boresight. The power line samples were placed in the horizontal plane and their polarimetric backscatter responses were measured in the principal plane of the radar antenna. The angular RCS patterns were obtained over the angular range -10° to 50° with a fine angular resolution 0.1°. Before comparing the analytical results with measured quantities a sensitivity analysis is carried out to examine the convergence of the iterative PO solution and the effect of the size of the footprint on the backscatter response. Assuming a plane wave illumination, Figures 3.2(a)–3.2(c) shows the contribution to the backscatter of the first–order and second–order PO currents for power line #1. In this case a cable length of 0.3 m and a center frequency 93.5 GHz are assumed. It is shown that for the co–polarized components the first–order PO solution accurately predicts the backscatter whereas the dominant source of cross–polarized component is the second–order PO currents. In fact the second order contribution is about 20 dB below the first order. Similarly the third order is of the same order of magnitude smaller than the second order. This also indicates that no higher order currents are needed to predict the polarimetric RCS response of power lines. The direction of significant backscatter readily can be predicted from the periodic dyadic

Green's function and is given by

$$\theta_n = \sin^{-1}\left(\frac{n\lambda}{2L}\right). \tag{3.25}$$

It is shown that levels of backscatter for Bragg modes beyond 15° incidence are reduced significantly. This is due to the fact that the specular points in backscatter direction cease to exist beyond 15° incidence. Next we examine the effect of the antenna footprint size on the RCS level and angular pattern. For this simulation we use again the geometry of power line #1 and consider a radar with Gaussian beam at a distance of 12 meters from the power line. Two cases corresponding to two beamwidths are considered: 1) a half–power beamwidth of 1.4° corresponding to the beamwidth of the radar used in the experiment, and 2) a half–power beamwidth of 0.7°. The lit area for the antenna with beamwidth 0.7° is half of that of the 1.4° beamwidth antenna and therefore we expect the RCS of the former be 6 dB lower than the latter. Figure 3.3 compares the VV backscatter response of the power line for the two spherical wave illumination. For these simulation free–space Green's function formulation was used. It is shown that the RCS pattern for each Bragg mode widens and the peak value drops (more than 6 dB) which are caused by the spherical phase front and non–uniform amplitude variations. The same effects are also observed when the RCS of a finite length (30 cm) cable illuminated by a plane wave is compared with the RCS of the same cable illuminated by the 1.4° beamwidth antenna. This comparison is shown in Figure 3.4 for vertical polarization. Figures 3.5(a)–3.5(d) show the comparison between the complete second–order PO model results with those measured using the University of Michigan 94 GHz scatterometer. The

overall agreement between calculated and measured cross–polarized backscatter radar cross section is very good. The slight discrepancies may be attributed to imperfection in the geometry of the power lines. There is a noticeable increase in the level of measured backscatter responses at angles larger than 15°.

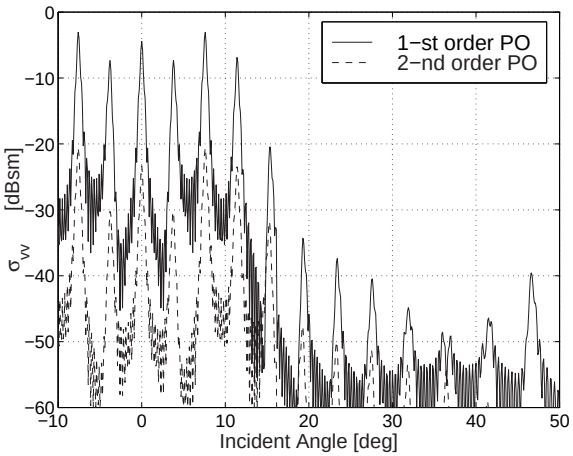

(a)

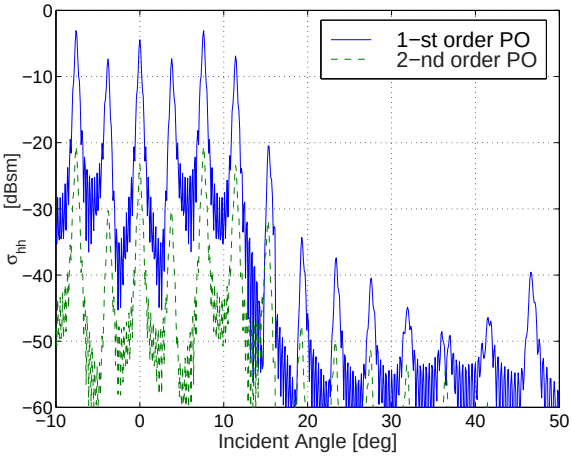

(b)

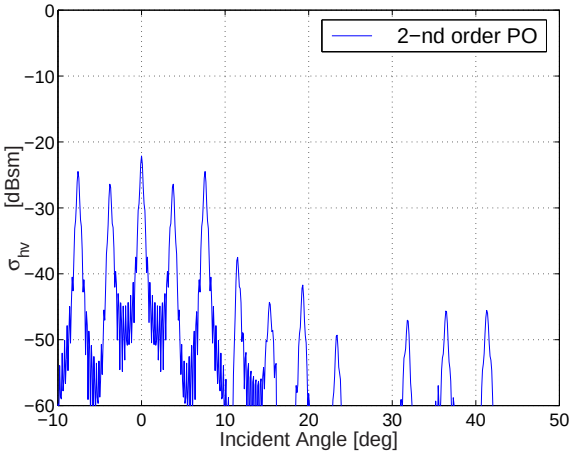

(c)

Figure 3.2: RCS of power line #1 produced by PO. The first and second order solutions are shown for the plane wave illumination of a 90 cm long cable. It is shown that the second order response is about 15 dB lower than the first order for VV and HH. (a)VV polarized response (b)HH polarized response (c)HV polarized response

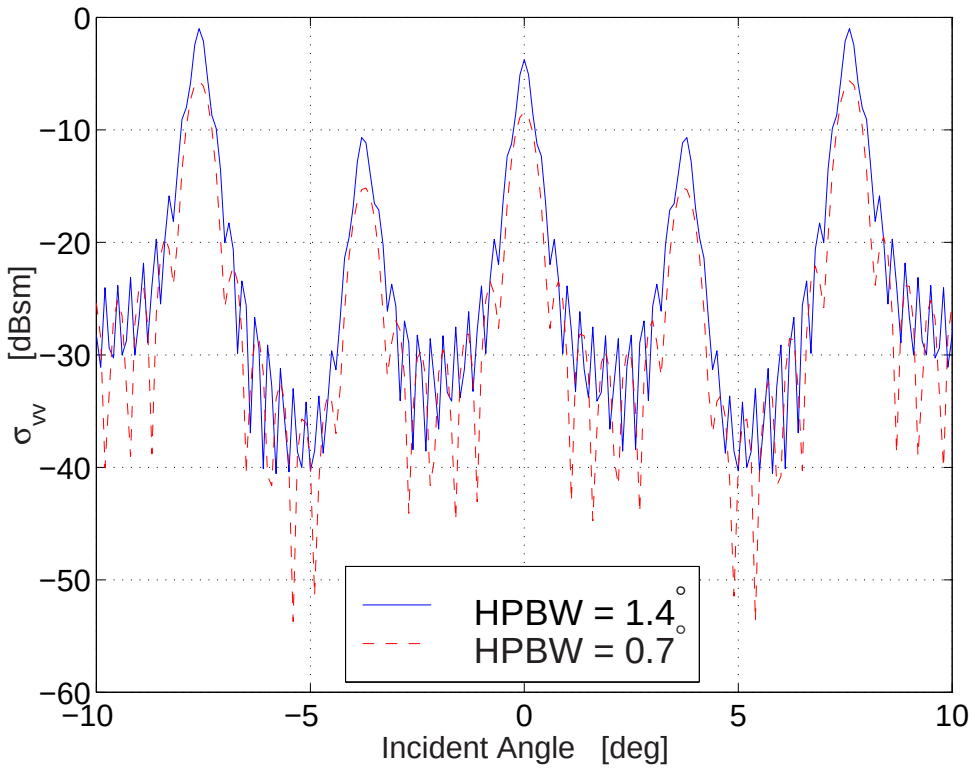

Figure 3.3: RCS of cable #1 when illuminated with an antenna with beamwidth 1.4° and 0.7° at a distance 12 m.

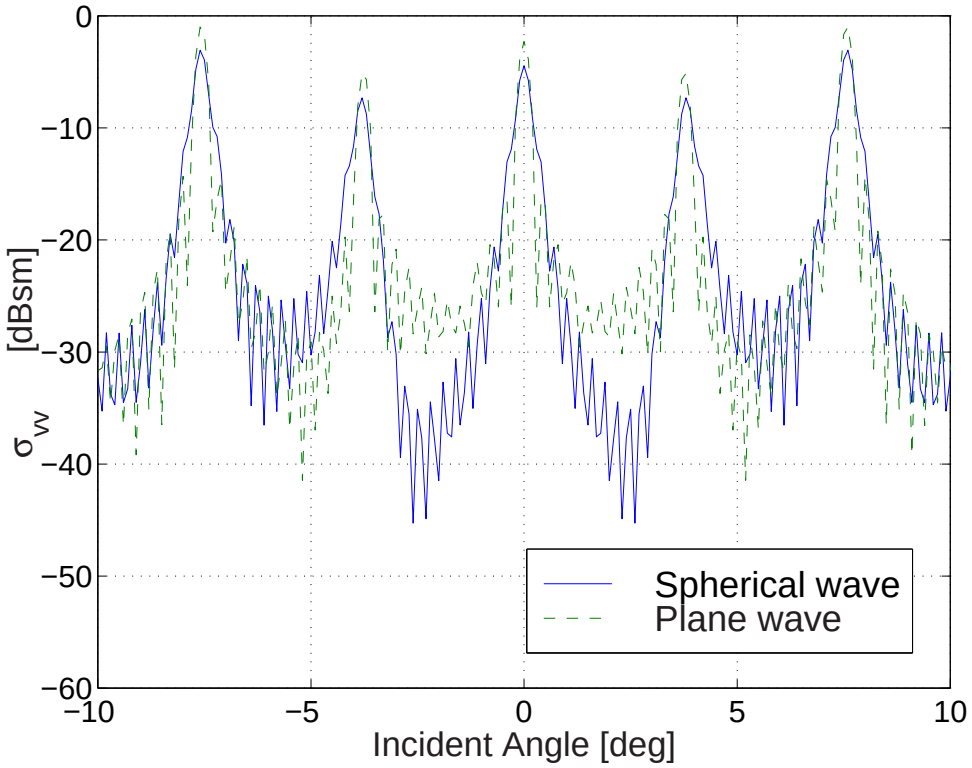

Figure 3.4: Comparison of RCS for plane wave illumination over finite length 30 cm and a spherical wave illumination assuming plane wave incidence observed by an antenna with a Gaussian beam and beamwidth 1.4° at a range 12 m from the power line. The 3–dB footprint is 30 cm in this case. Range=12 (m), Beamwidth=1.4°

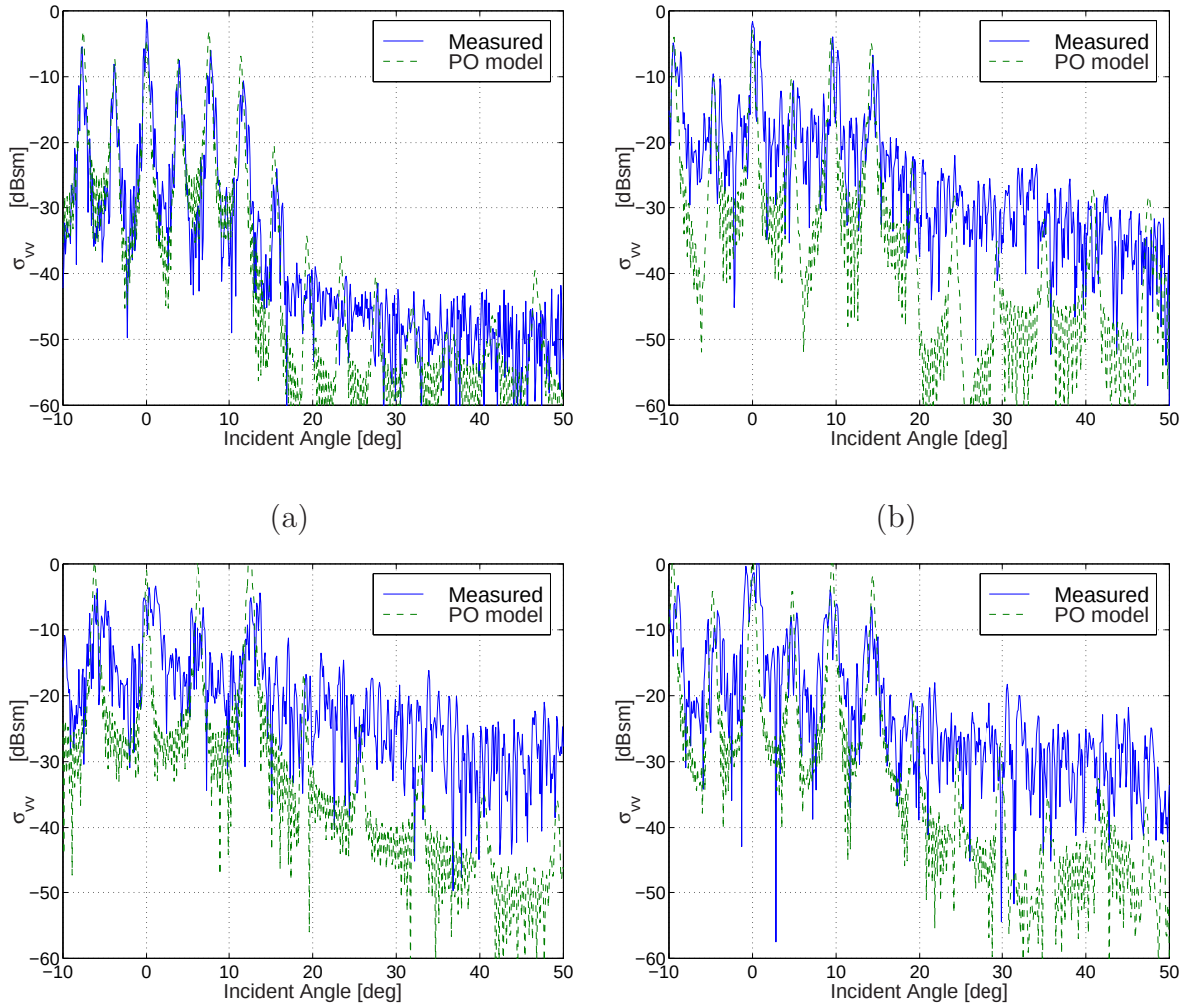

Figure 3.5: Comparison of the simulated (assuming a Gaussian Beam) and measured VV polarized backscatter responses of the four power line samples used in this study (a)power line #1 (b)power line #2 (c)power line #3 (d)power line #4

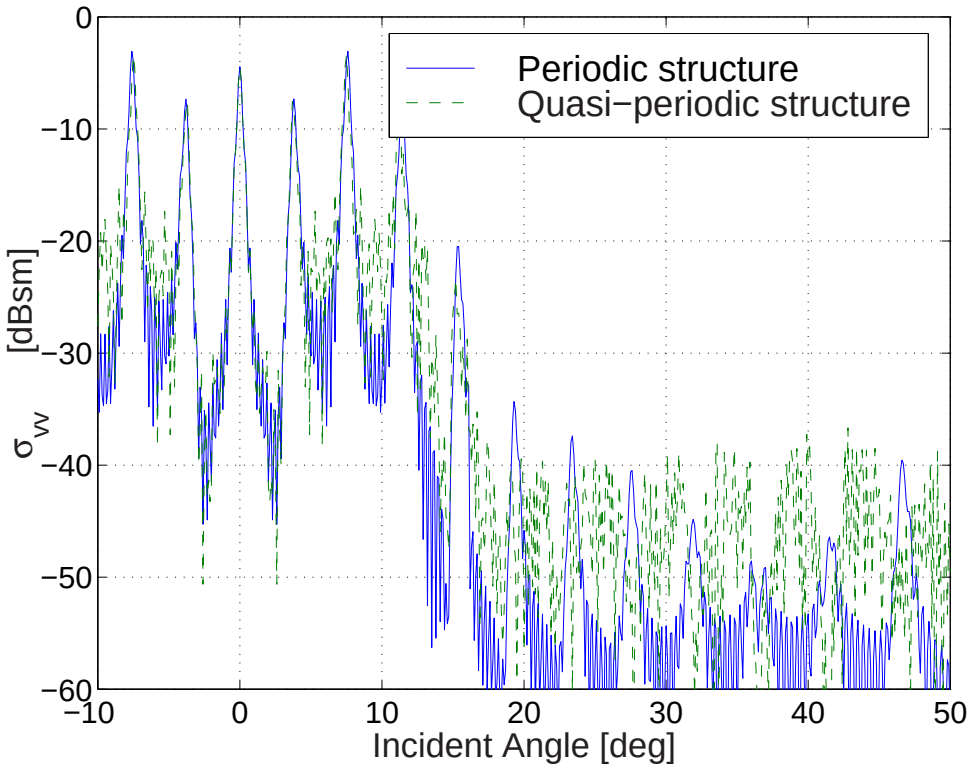

Figure 3.6: Effect of surface irregularity for power line #1. In this simulation the power line structure is modified by inserting gaps between adjacent strands. The size of the gaps are randomly distributed from zero to 1/20 of the strand diameter.

Flexing and straightening of power line cables perturbs the periodic arrangement of the outer strands. At W–band frequencies a movement of outer strands as small as 0.5 mm can have a significant impact on its RCS pattern. To simulate the effect of surface irregularities a variable gap (spacing) with a mean of about 1/20 of the strand diameter was inserted between adjacent strands randomly. A Gaussian distribution was used to specify the gap width. Figure 3.6 shows the RCS patterns of cable #1 for a perfect periodic and quasi–periodic surface structure. In this case a non–

uniform illumination for the antenna with a beamwidth 1.4° is used. The quasi–periodic structure shows also noticeable increase in the backscatter level at incident angles larger than 15° and some variations in the peak values of the RCS along the Bragg directions. The effect of the surface irregularities was most evident from the backscatter measurement of power line #4 as this cable has 21 outer aluminum strands that are loosely wound. Figure 3.5(d) shows the measured and simulated σ_{vv} of power line #4 where the simulated results are those of a periodic structure with a non–uniform illumination similar to the incident field.

Another parameter of practical importance to be considered is the effect of power line sag on its backscatter response. When designing high voltage power lines, it is essential to determine the stress and sag of the conductor for several reasons. A power line cable when suspended between two towers conforms to a curve known as catenary. The parameters of this function are determined by the physical parameters of the cable such as weight per unit length the mechanical properties of the strands, the span of the supporting towers, and the environmental effects such as temperature and the existence of an external load such as ice. To simulate the effect of power line sag on its RCS, simulation of RCS of power line #1 suspended between two steel towers 250 m apart at -5° Celsius with an ice load of 0.65 kg/m is considered. This configuration generates a displacement of about 6.6 m in the middle. The profile for the power line is simulated and shown in Figure 3.8. The temperature and the ice load were selected to simulate deeper sag which is expected to exhibit more influence on the power line RCS. Here a comparison is made between the backscatter response of a curved and a straight power line. RCS of the line is calculated for two different

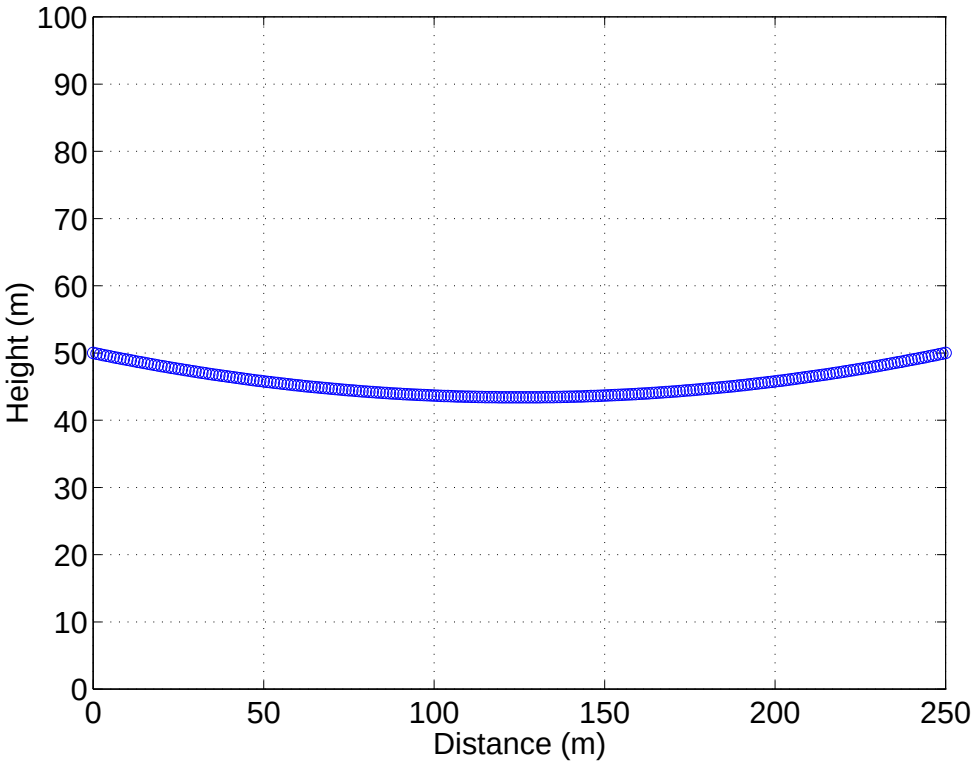

Figure 3.7: A profile of a suspended power line(150-Alfe-6-ACSR) under an ice load. Span=250 (m), Tower height=50(m), Ice load=0.65 kg/m.

ranges, 100 m, and 500 m, using a real beam antenna with beamwidth of 1.4°. The center of the radar beam is chosen at a distance 10 m from the left–end of the cable. At normal incidence the footprint sizes for 100 m and 500 m are 2.4 m and 12 m respectively. Figures 3.8(a) and 3.8(b) show the comparison between the RCS of a straight and a curved cable at 100 m and 500 m respectively. The main effect of the sag on power line RCS is observable on RCS level of Bragg backscatters at incidence angles lower than 17°. It is shown that a suspended cable has RCS values about 5 dB lower than that of a straight cable at normal incidence and at the third Bragg direction (about 8° from normal incidence), and slightly higher values at other Bragg angles. Since there still exist strong backscatter for near–normal aspect angles, the detectability will not be affected much by the curvature of power lines.

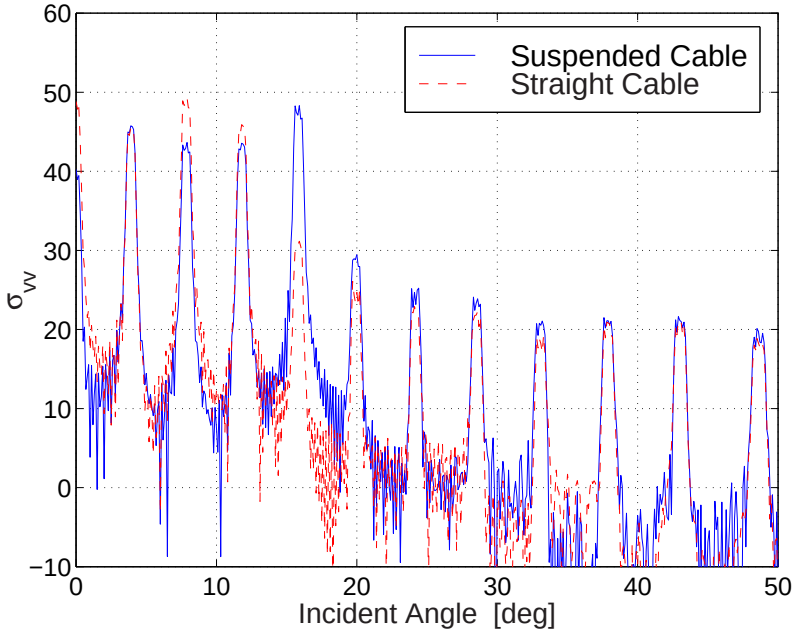

(a)

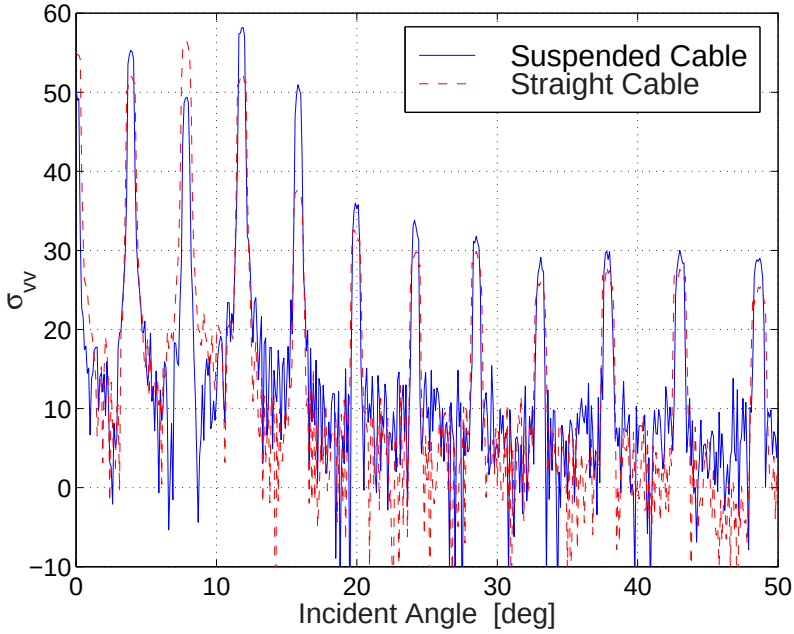

(b)

Figure 3.8: Effect of sag on the radar backscattering response. Span=250 (m), Sag=6.6(m), Radar beam=1.4°. The center of the antenna beam is located 10 m away from the left-end of the cable. (a)Range = 100 (m) (b) Range = 500 (m)

3.5 Conclusions

Electromagnetic scattering formulation for braided cables and power lines is formulated in this Chapter. Magnetic field integral equation in conjunction with periodic Green's function is developed as a basis for the calculation of the scattered field. This formulation together with the method of moment presents a viable approach for the field calculation at frequencies up to Ku–band beyond which it becomes numerically inefficient. An approximate solution based on iterative physical optics approximation was proposed as an alternative for millimeter–wave frequencies. Through comparison with experimental data at 94 GHz, it was shown that the iterative PO solution up to second order is capable of predicting the polarimetric backscatter responses of power line cables. This solution was used in a sensitivity analysis to study the effect of different geometrical parameters of power lines on their polarimetric backscatter response.

CHAPTER 4

EXTRACTION OF POWER LINE MAPS FROM MILLIMETER-WAVE POLARIMETRIC SAR IMAGES

4.1 Introduction

The use of helicopters for military and civilian applications is ever increasing. The civilian applications cover a broad range including rescue operations, air ambulance, recreation, construction, etc.. Helicopters also have a broad range of applications in military. They provide superiority over rugged battle fields and constitute a formidable force against armored vehicles and heavy artillery. Operation of these fast low-flying machines, however, is highly limited under poor visibility. The major safety problem is the collision with man-made and natural obstacles such as towers, power lines and mountains. Due to the existing poor safety records of helicopters, strict safety regulations have been put in place to ensure helicopters stay grounded

under conditions of bad visibility even in emergencies. A reliable and all-weather collision warning system rectifies this deficiency. Because of their compact size and all-weather operation capability, millimeter-wave radar systems have been proposed for this purpose [5]. However, detection of hazardous targets in the radar scene is a complicated task and is the subject of many ongoing investigations.

A hazardous target of particular interest is an overhead high voltage power line. A typical scenario of a helicopter approaching a power line in a strong clutter background is depicted in Figure 4.1. In the past, several approaches for detecting nearby power line cables have been proposed which include optical and infrared sensors [4, 6]. The detection of power lines, independent of frequency of the sensor, is very challenging since the cross section of these cables are rather small. In many practical situations where there is a significant clutter background the power line signal-to-clutter ratio is very low. The polarimetric backscatter behaviors of power line cable have been modelled in the Chapter 3 where it is shown that at millimeter-wave frequencies significant backscatter exists only at normal incidence and along certain directions known as Bragg backscatter directions [29]. The spacing between Bragg backscatter directions depends on the cable dimensions (surface period) and the radar wavelength. Nevertheless, it is shown that none of the Bragg modes contribute significantly at incidence angles beyond 15 degrees. The level of backscatter drops significantly at higher angles which is why the detection of power lines using conventional radars is not possible. Experimental results at Ka- and W-band also show the trends predicted by the model [8, 30].

The problem of power line detection with poor signal-to-clutter was first consid-

ered in [8] where a polarimetric detection algorithm was proposed. The performance of this algorithm was demonstrated under laboratory conditions and the results were reported in [30]. In this chapter the performance of the algorithm is further examined using polarimetric SAR images at 35 GHz. The motivation behind this investigation is twofold: 1) to examine the accuracy of the polarimetric algorithm using real data, and 2) to demonstrate the feasibility of mapping power line networks using remote sensing data. While the location of power lines are well documented in friendly areas, knowledge of their exact location in unfriendly regions is often inaccurate and in some cases is not available. In what follows first a brief description of the polarimetric detection algorithm is given. Then the general behavior of polarimetric response of clutter at millimeter-wave frequencies is considered. In Section 4.4 an analytical approach for performance evaluation of the algorithm is presented. In this section the relationship between the required number of independent samples for a given false alarm rate in terms of radar aspect angle and power line backscatter level is developed. In Section 4.5, the performance of detection algorithm in detecting power lines in 35 GHz radar images is presented.

4.2 Detection Algorithm

In this section, the basic concept of the polarimetric detection algorithm is reviewed. As mentioned earlier, the detection of power lines, either in radar images or when a real aperture radar is used, is hampered by poor signal-to-clutter ratio. In traditional detection algorithms, detection is made by simply comparing the mea-

sured radar backscatter to a detection threshold. Hence for detection, the magnitude of power line backscatter should be larger than the threshold value which is usually higher than the mean value of the clutter backscatter coefficient. However, this condition is not met when the aspect angle of the power line is away from near-normal incidence direction. In this situation, there exists no strong backscatter from the power line and the signal-to-clutter ratio is very low. In practice, the backscatter from background vegetation or rough surfaces within the same range as the power line, may drastically exceed the backscatter from the power line. This is why conventional non-polarimetric millimeter wave radars cannot be used for power line detection. To circumvent this difficulty, we resorted to radar polarimetry and proposed a statistical detection algorithm to improve the signal-to-clutter ratio.

Theoretical and experimental investigations have shown that the co- and cross-polarized components of backscatter of distributed targets with azimuthal symmetry are statistically uncorrelated [32]. In other words $\langle S_{VV}S_{HV}^{*}\rangle$ and $\langle S_{HH}S_{HV}^{*}\rangle$ vanish for almost all distributed targets provided that the footprint is much larger than the field correlation length in the random medium. However, as was shown in [30] the co- and cross-polarized component of backscatter from power lines are highly correlated ($\langle S_{VV}S_{HV}^{*}\rangle \neq 0$). Measuring $\langle S_{VV}S_{HV}^{*}\rangle$, instead of $\langle |S_{VV}S_{VV}^{*}|^{2}\rangle$ for example, should improve detection probability drastically.

To circumvent the difficulties associated with radiometric calibration, normalized cross correlation, or namely coherence γ between two radar backscattering components, S_{HV} and S_{VV}, can be used. The coherence between VV and HV channel is

defined by

$$\gamma = \frac{\langle S_{VV} S_{HV}^{*} \rangle}{\sqrt{\langle |S_{VV}|^2 \rangle \langle |S_{HV}|^2 \rangle}} \,. \tag{4.1}$$

Assuming that the process is ergodic, the estimate of the coherence can be obtained by substituting the ensemble averages in the above expression with spatial averages. The coherence is estimated from linear section of the image along which a power line sections may exist. A threshold detection level is then chosen for the coherence estimate which depends on the required false alarm rate and probability of detection. The choice of S_{VV} instead of S_{HH} stems from the fact that the backscatter from power lines (away from normal incidence) for VV polarization is higher than that of HH polarization [30]. However, in situations where fully polarimetric data is available both coherence values can be used for detection of power lines. The probability of detection is a function of number of independent samples, the values of the backscattering coefficient, and the backscatter level of the power line itself. This subject is discussed in detail in Section 4.4.

4.3 Backscatter Behavior of Clutter and Power Lines at Millimeter-Wave Frequencies

As mentioned earlier the probability of detection and the false alarm rate of power lines depend on the backscatter level of clutter background and its statistics. The radar backscatter behavior of clutter in the millimeter-wave frequencies is very important in the design and understanding of the power line detection radar system.

Because scattering effects in these frequencies are unique it is not possible to simply scale the microwave radar backscatter behaviors to these millimeter-wave frequencies.

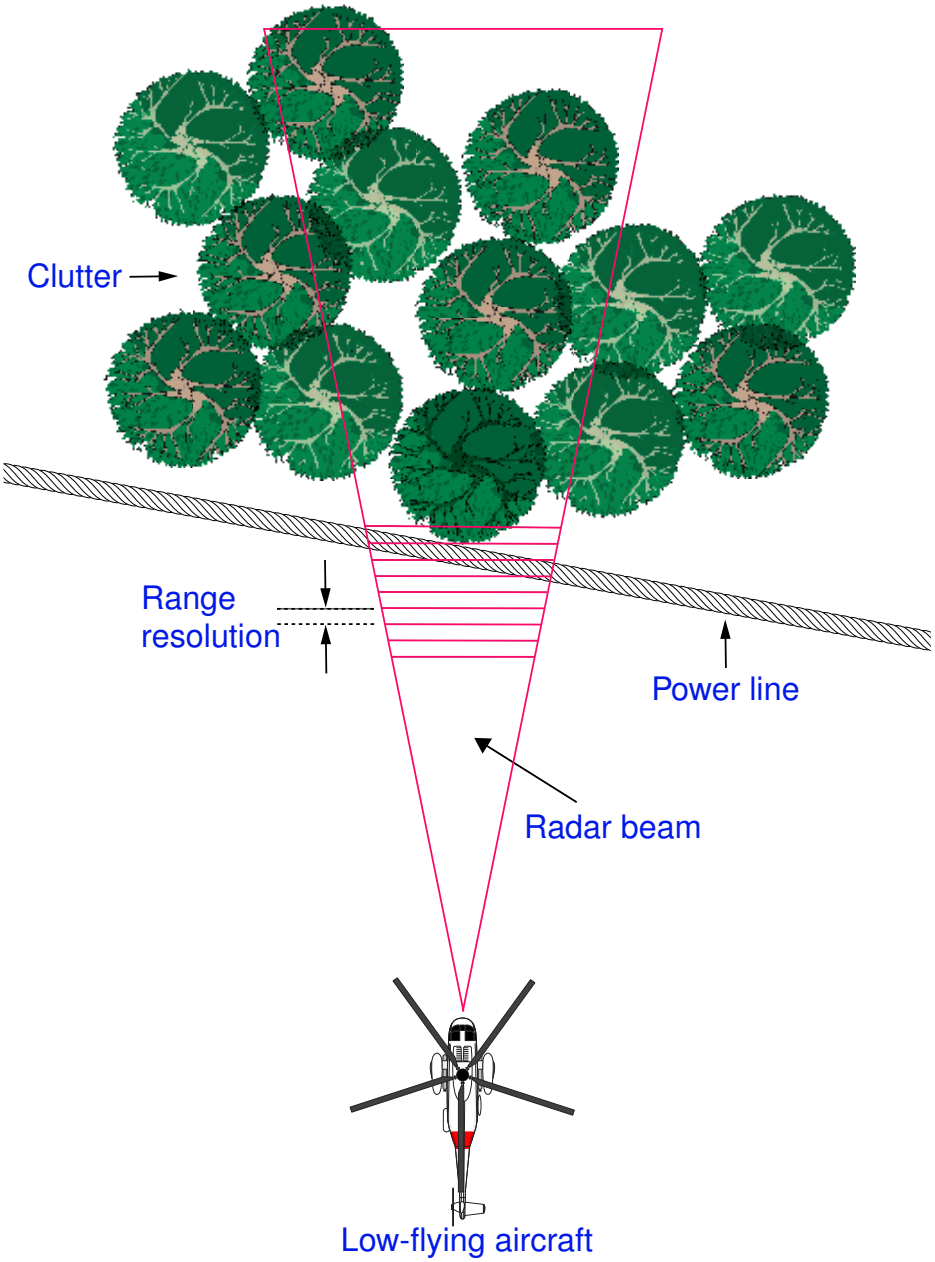

Figure 4.1: A scenario of a helicopter approaching a power line in a strong clutter background

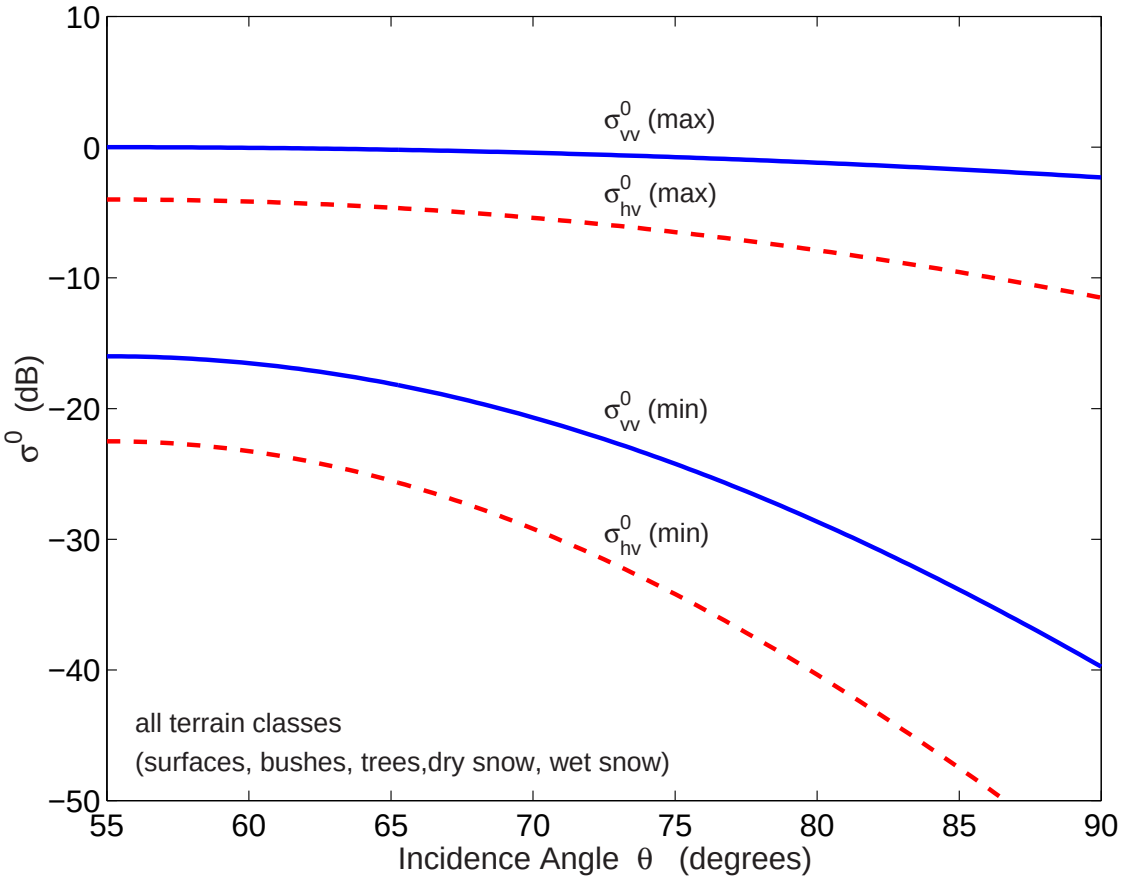

Figure 4.2: Dynamic range of σ^0 for terrain at 94 GHz. The maximum and minimum curves represent the upper and lower bound among all measured values reported in [10] and [16].

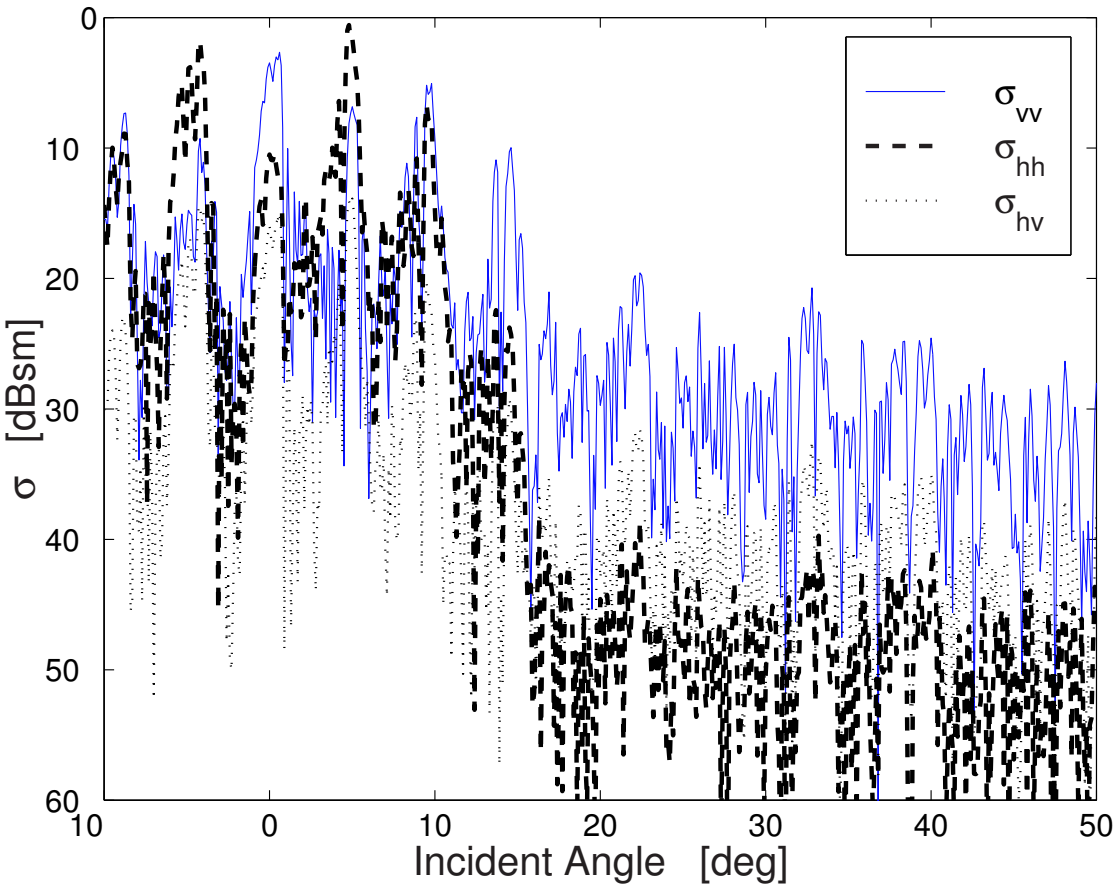

Figure 4.3: Angular RCS response of a power line at 94 GHz

Over the past two decades significant amount of effort has been devoted towards characterizing the backscatter behavior of radar clutter at millimeter-wave frequencies. These activities in general can be categorized into two groups: 1) experimental characterization of clutter backscatter behavior, and 2) theoretical modelling of clutter backscatter. A comprehensive overview of these activities is beyond the scope of this chapter, however, a brief discussion related to the problem at hand is provided here. The spectral, angular, and polarimetric behavior of clutter backscatter depends on the clutter type and its physical parameters. Apart from the urban areas, radar clutter may be categorized into three general groups: 1) surfaces, 2) short vegetation and shrubs, and 3) tall vegetation. Backscatter from surfaces at millimeter-wave frequencies is composed of surface scattering and volume scattering [34, 35, 36]. Surfaces, such as bare soil surfaces, asphalt, gravel, concrete, etc., are heterogeneous media composed of particles of different permittivity whose dimensions are comparable to the wavelength at millimeter-wave frequencies. Depending on the surface roughness and extinction in the medium the surface scattering or volume scattering may be dominant. At microwave frequencies surface scattering is dominant but at millimeter-wave frequency region both component exist. Volume scattering is comparable to surface scattering for dry soil while volume scattering component is negligibly small compared to the surface scattering component. The volume scattering depends on the height statistics of the interface between air and the surface. It also depends on the size and distribution of inclusions in the ground and dielectric constant of the host material. The backscatter level decreases with increasing the incidence angle and decreasing the frequency.

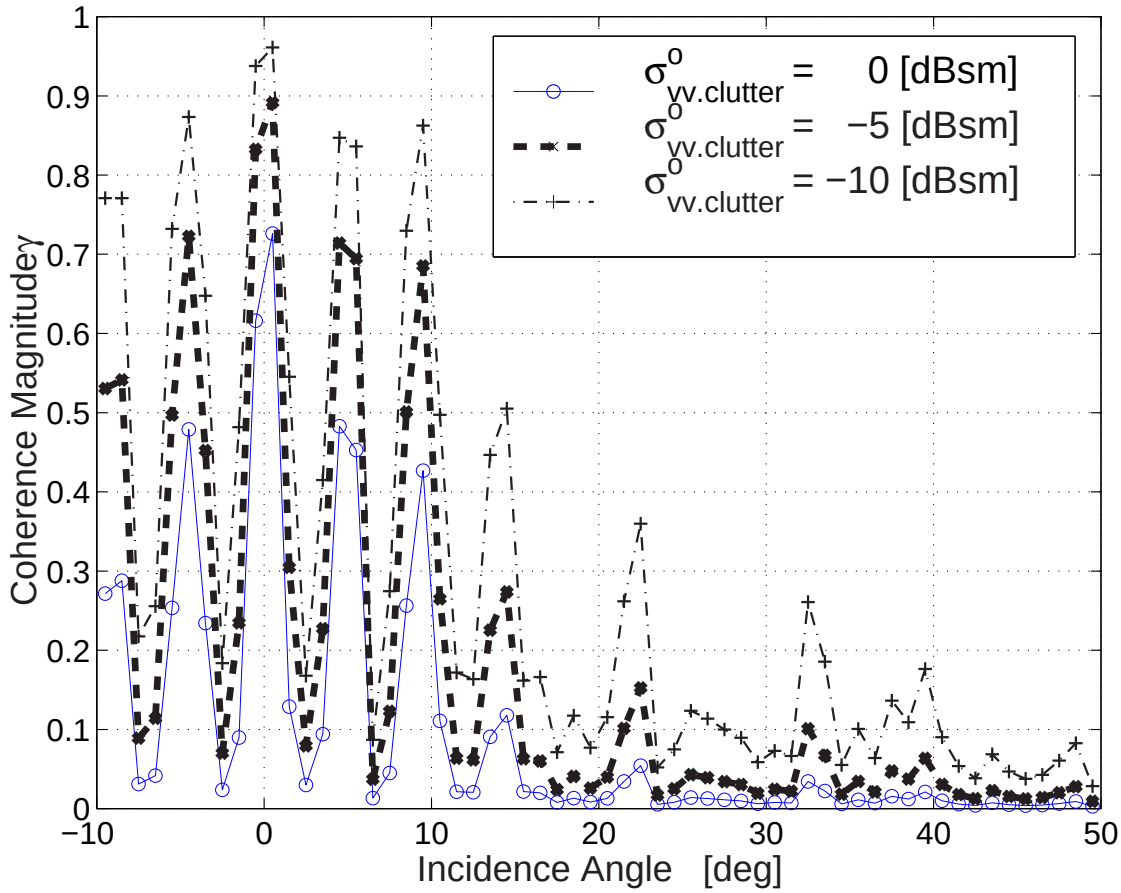

Figure 4.4: Coherence of the power line shown in Figure 4.3 in different background clutter with $\sigma^0_{HV}/\sigma^0_{VV} = -10dB$.

Wet surfaces demonstrate markedly lower backscatter level and low cross-polarized to co-polarized backscatter ratio. The backscatter of surfaces covered with snow is dominated by the volume scattering from the snow [35, 36, 37]. The level of backscatter of a snow pack decreases with the snow wetness and is a relatively strong function of frequency. The radar backscatter from snow changes significantly when snow goes through melting/refreezing cycles. Thus snow should be classified into two groups, in terms of radar backscattering, wet snow and frozen (dry) snow. The backscatter level is low when wet and high when snow is refrozen. Radar backscatter from wet snow are 8 to 10 dB lower than that of refrozen snow at 35 GHz. 95 GHz snow data are 5 dB higher than 35 GHz snow data. 95 GHz refrozen snow produces 10 dB higher radar backscattering than 95 GHz wet snow. Refrozen snow has high level of σ^o at both 35 GHz and 94 GHz frequencies for high grazing angles ($>$ 30 degrees). This generates tough environment for target detection. Metamorphic snow which possesses larger ice particles exhibit higher backscatter. Co-polarized backscattering coefficient as high as +1 dB for dry snow and -1 dB for wet snow and cross- to co-polarized ratio of -5 dB has been reported in the literature [37]. Due to high extinction rate in vegetation, backscatter from most vegetation media emanates from the particles near the interface between the canopy and air. The dependence of backscatter to frequency, at millimeter-wave frequencies, is very weak. Usually the level of backscattering coefficients for VV and HH polarizations is similar. Vegetation media also produce significant cross-polarized component, only 4-5 dB below the co-polarized components. Experimental results have shown that for incidence angles higher than 30°, the co-polarized backscattering coefficients at W-band hardly exceed

0 dB and this upper value is reduced for near grazing incidence to about -5 dB. The lower bound which is produced by impenetrable surfaces with relatively smooth surface roughness exhibit backscatter levels around -15 dB and have a much faster rate of decrease with incidence angle. For these surfaces the ratio of cross-polarized to co-polarized backscattering coefficients can be anywhere between -10 dB to -15 dB. Figure 4.2 shows the upper and lower bound of σ°_{VV} and σ°_{HV} obtained from measurements of different clutter types at 94 GHz [40].

Radar backscatter behavior of power lines have also been studied extensively over the past few years [29, 8, 30]. As mentioned earlier the backscatter up to 15° off normal incidence is dominated by strong Bragg scattering. Away from normal incidence, the backscatter is dropped significantly. However, due to surface irregularity (deviations from perfect periodicity) there are measurable backscatter power at angles beyond 15° incidence. Figure 4.3 shows the polarimetric backscatter of a power line with diameter 3.52 cm at 94 GHz [30]. The power line was illuminated by an antenna having a footprint of about 30 cm on the cable. It is observed that σ_{VV} is much higher than σ_{HV} and furthermore considerable cross-polarized backscatter is produced. This is the main reason for choosing the coherence between VV and HV component of backscatter as the detection parameter.

4.4 Coherence Estimation

The proposed detection algorithm is based on a comparison between the co- and cross-polarized coherence of clutter and that of a power line. In practice the coherence

is estimated from the average of a finite number of the measured samples (pixels) of the random variable. Hence the estimate itself is a random variable which in most cases has the same mean as the original random variable with a much smaller variance. In this particular case where the normalized correlation coefficient is always a positive quantity, the ensemble average of the coherence estimate is always larger than the coherence ($\langle\hat{\gamma}\rangle > \gamma$). For example the clutter coherence is zero and the mean coherence estimate is a positive quantity. In order to quantify the false alarm rate (FAR) and the probability of detection (PD), probability density functions (pdf) of clutter coherence and coherence of pixels including power line segments are needed.

Assuming the clutter statistics is described by a Gaussian process, the pdf of the estimate of co- and cross-polarized coherence can be derived analytically. Suppose N pixels are used to estimate the coherence, then the pdf of ($\hat{\gamma}$) is given by [41],

$$p(\hat{\gamma}) = 2(N-1)(1-\gamma^2)^N\hat{\gamma}(1-\hat{\gamma}^2)^{N-2}F(N,N;1;\gamma^2\hat{\gamma}^2) \tag{4.2}$$

where γ is the coherence and F is the hypergeometric function also known as the Gauss' hypergeometric function [39]. For clutter where $\gamma = 0$, the pdf given by (4.2) simplifies significantly and is given by:

$$p(\hat{\gamma}) = 2(N-1)\hat{\gamma}(1-\hat{\gamma}^2)^{N-2}. \tag{4.3}$$

For pixels including power line segments, the coherence is a function of power line backscatter as well as clutter backscattering coefficients. Adding the clutter backscatter of a pixel ($\sigma^o A$) to that of the power line incoherently, it can easily be

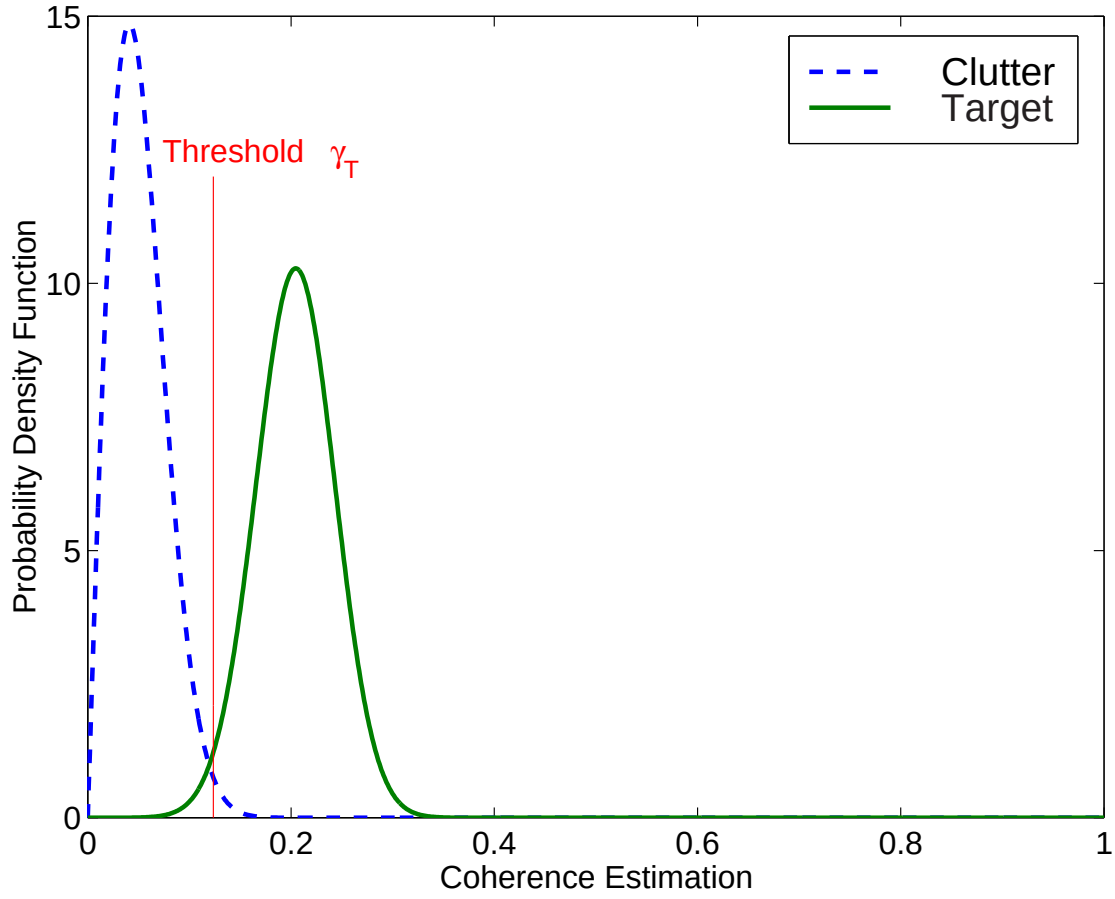

Figure 4.5: Probability density function of clutter ($\gamma = 0$) and power line in clutter ($\gamma = 0.2$) using N =300 independent samples. A threshold level is also shown. The areas under curves beyond γ_T are the FAR and PD.

shown that the coherence of pixels including power line segments is given by

$$\gamma = \frac{|\sigma^p_{VV,HV}|}{\sqrt{(\sigma^\circ_{VV}A + \sigma^p_{VV})(\sigma^\circ_{HV}A + \sigma^p_{HV})}} \tag{4.4}$$

where $\sigma^p_{VV,HV} = 4\pi S_{VV}S^*_{HV}$, σ^p_{VV}, and σ^p_{HV} are, respectively, the cross correlation between VV and HV backscatter, and VV and HV radar cross section of the power line segment in each pixel. Also σ°_{VV} and σ°_{HV} are the clutter backscattering coefficients and A is the pixel area. Substitution of (4.4) in (4.2) provides the pdf for the estimate of coherence for pixels that include the power line. Using the measured polarimetric backscatter data from the power line whose RCS is shown in Figure 4.3 the coherence of the power line #3 in different clutter backgrounds is shown in Figure 4.4. Here it is assumed that the radar pixel is 30 $cm \times 30$ cm and the clutter cross- to co-polarized ratio $\sigma^\circ_{HV}/\sigma^\circ_{VV} = -10dB$. It should be pointed out here that since the increase in the power line RCS with decreasing the resolution is slower than the increase in pixel area, radars with finer resolutions provide higher coherence for pixels which include power lines.

Successful detection and false alarm rate depend on the separation between the mean values of clutter and power line coherence estimate and on the narrowness of their density functions. Fortunately closed form solutions for the moments of coherence estimate exist. The first and second moments are given by:

$$< \hat{\gamma} >= \frac{\Gamma(N)\Gamma(3/2)}{\Gamma(N+1/2)}\ {}_3F_2(3/2, N, N; N+1/2, 1; \gamma^2)(1-\gamma^2)^N,$$

$$< \hat{\gamma}^2 >= \frac{1}{N}\ {}_3F_2(2, N, N; N+1, 1; \gamma^2)(1-\gamma^2)^N.$$

where ${}_pF_q$ is the generalized hypergeometric series and Γ is the gamma function. Noting that ${}_3F_2(2, N, N; N+1, 1; 0) = 1$, the mean and the second moment of the

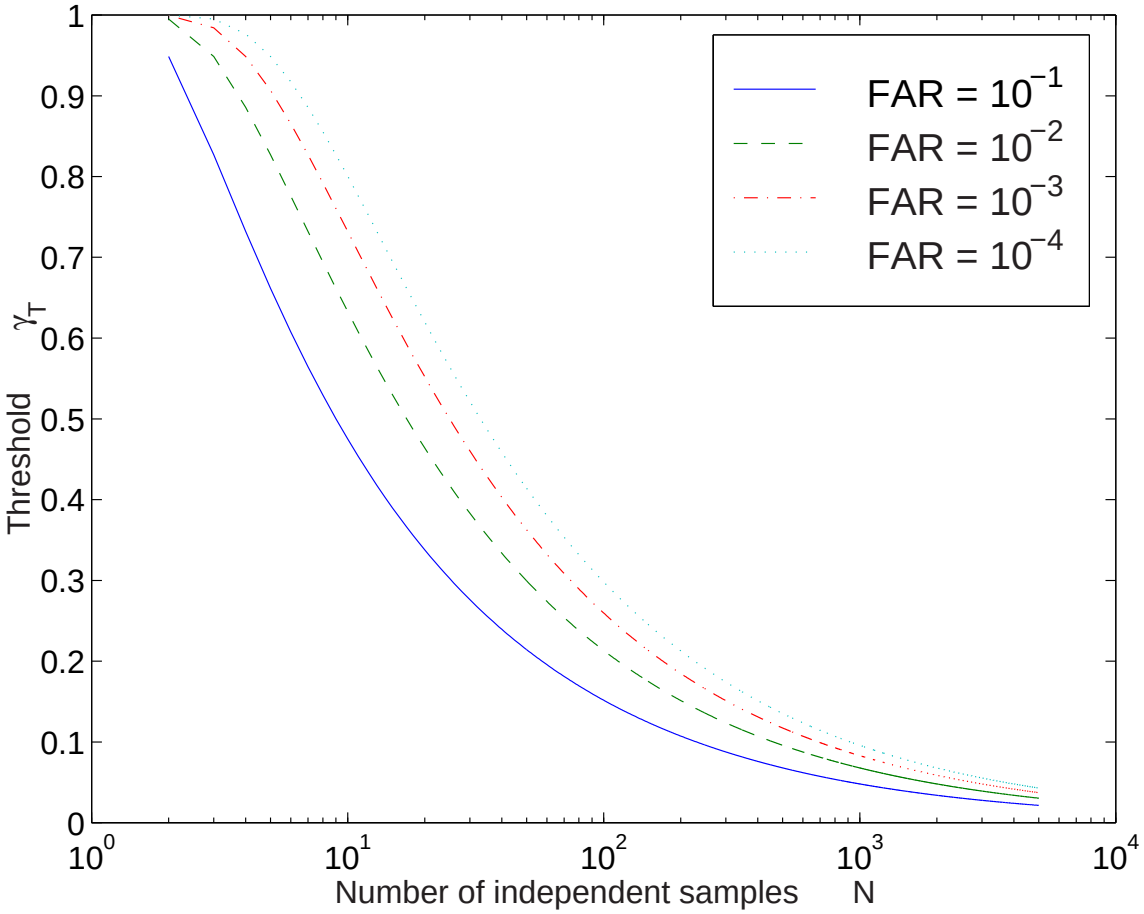

Figure 4.6: Threshold level as a function of number of independent samples for different values of FAR.

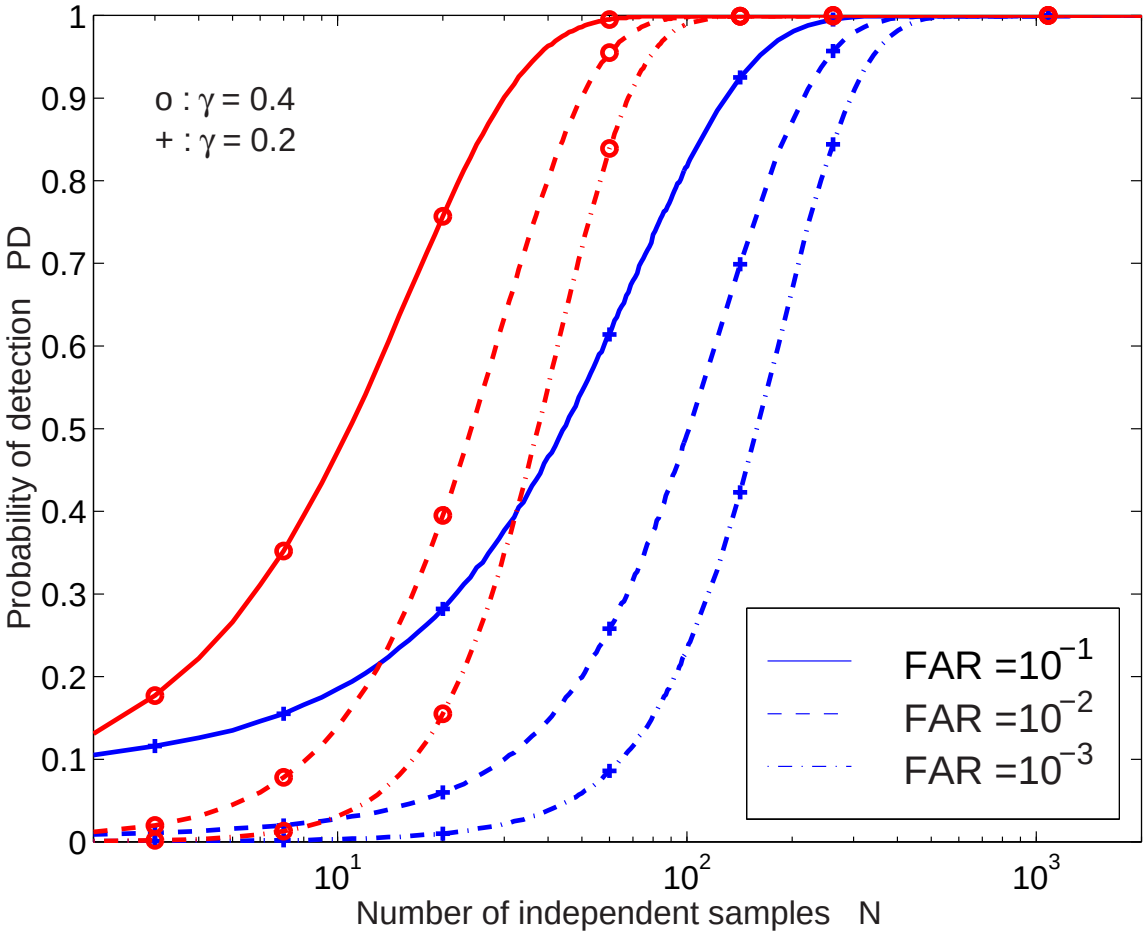

Figure 4.7: Probability of detection as a function of number of independent samples and for different values of FAR and coherence values of power lines in clutter.

coherence estimate of the clutter simplify to:

$$< \hat{\gamma} >= \frac{0.8862\Gamma(N)}{\Gamma(N+1/2)}, \qquad < \hat{\gamma}^2 >= \frac{1}{N}$$

which are only a function of number of independent samples. Using the large argument expansion of gamma function (Stirling formula), the mean of the coherence estimate for large $N > 10$ may be evaluated from:

$$< \hat{\gamma} >= \frac{0.8862}{\sqrt{N}}.$$

In this case the standard variation is simply equal to $0.463/\sqrt{N}$.

To demonstrate the procedure for the calculation of the false alarm rate and the probability of detection let us assume that $N = 300$ pixels are available for estimating the coherence and the coherence of pixels with power line is $\gamma = 0.2$. Figure 4.5 shows the pdfs of the clutter and power line for this example. Also shown in this Figure is a threshold (γ_T) above which power line detection is flagged. The percentage of the time (probability) that the clutter coherence exceed the threshold level is the false alarm rate and the probability that power line coherence is above the threshold level is the probability of detection. There is a trade off between the false alarm rate and the probability of detection. The lower is the false alarm rate the lower would be the probability of detection. The false alarm rate (FAR) can explicitly be related to the threshold level and the number of independent samples using (4.3)

$$FAR = 2(N-1)\int_{\gamma_T}^{1} \hat{\gamma}(1-\hat{\gamma}^2)^{N-2} d\hat{\gamma}\,,$$

which renders the following relationship:

$$\gamma_T = \sqrt{1 - FAR^{\frac{1}{N-1}}}\,.$$

In a similar manner the probability of detection (PD) can be computed from (4.2)

$$PD = 1 - 2(N-1)(1-\gamma^2)^N \int_0^{\gamma_T} \hat{\gamma}(1-\hat{\gamma}^2)^{N-2} F(N, N; 1; \gamma^2\hat{\gamma}^2) d\hat{\gamma}\,. \tag{4.5}$$

Unfortunately a simple closed form for (4.5) cannot be obtained; however, using the series expansion representation of the hypergeometric function the probability of detection in terms of a chosen FAR and number of independent samples can be obtained from

$$\begin{aligned} PD &= 1 - (N-1)(1-\gamma^2)^N \sum_{k=0}^{\infty} \sum_{j=0}^{N-2} \left(\frac{(N+k-1)!\gamma^k}{(N-1)!k!} \right)^2 \frac{(N-2)!}{(N-j-2)!j!(j+k+1)} \\ &\quad \cdot \left(1 - FAR^{\frac{1}{N-1}}\right)^{(j+k+1)} \end{aligned} \tag{4.6}$$

Usually γ_T is a relatively small number (< 0.2) and only few terms in k are sufficient for calculating PD. Figure 4.6 shows the threshold level as a function of number of independent samples for different values of FAR. Also Figure 4.7 shows the PD as a function of number of independent samples and different values of FAR and γ.

4.5 Performance of Detection Algorithm

The performance of the polarimetric detection algorithm at W-band frequencies was demonstrated under laboratory conditions earlier [30]. In this section, the performance of the algorithm is examined using polarimetric data acquired by a millimeter-wave synthetic aperture radar. As discussed in the previous section the FAR and the PD are functions of the number of available independent samples and the coherence of pixels which include the power line. Referring to Figure 4.5, it is obvious that the coherence of the pixels with power lines is a function of clutter

backscattering coefficients, power line aspect angle, and the power line RCS. RCS of power lines increases with increasing frequency especially at aspect angles beyond 15° for normal (see typical RCS values at Ka-band and W-band reported in [8] and [30]). However, the backscattering of clutter at millimeter-wave frequency is not a strong function of frequency, therefore, the higher is the radar frequency the higher will be the coherence of pixels with power lines.

The only polarimetric millimeter-wave SAR data available are those acquired by the Lincoln Laboratory Ka-band polarimetric SAR [44]. Figure 4.10 shows Lincoln Laboratory's high- resolution multi-polarization Synthetic Aperture Radar (SAR) mounted under a Gulfstream aircraft. This radar is a fully polarimetric, air-to-ground SAR that operates stripmap mode with a +90-degree squint angle; that is, the radar points +90 degrees relative to the velocity vector. The transmitter alternates between H-pol and V-pol, while H-pol and V-pol are simultaneously processed in the receiver. The radar transmits at a 3-kHz rate, so that the same-polarization pulse repetition frequency (PRF) is 1.5 kHz. This radar operates at the center frequency of 33 GHz and has a bandwidth of 500 MHz. The radar antenna beamwidth is 2° and can provide radar images with resolution of 30 cm× 30 cm. In order to investigate the behavior of radar clutter at low grazing incidence, the Lincoln Lab Ka-band SAR was flown at low altitudes and a large number of polarimetric SAR images were acquired. Among these seven images which included power lines were identified and selected for the performance assessment of the algorithm. High resolution aerial photograph of radar scenes are also available. Using the aerial photographs the radar images were chosen so that they contained a wide range of clutter types and power line aspect

Figure 4.8: An aerial photograph of a test site.

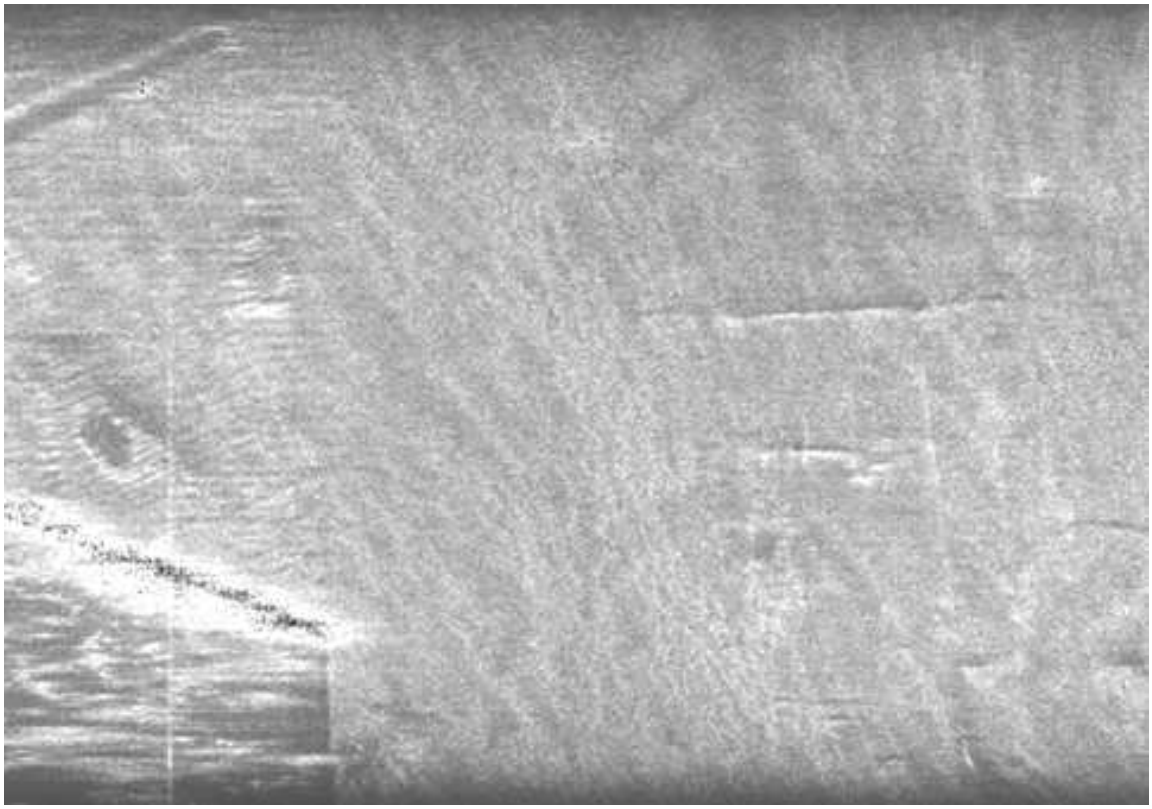

Figure 4.9: An example of SAR image including a power line section before detection.

Figure 4.10: The Lincoln Laboratory's Ka-Band high-resolution fully polarimetric Synthetic Aperture Radar (SAR) used to collect the SAR imageries used in this work. The radar is mounted below a fuselage of a Gulfstream aircraft. System parameters: frequency 33 GHz, resolution (SAR) 1 ft $\times$ 1 ft, beamwidth 2°, polarization isolation 1000/1, sensitivity (SAR mode) (7 km range) S/N = 10 for 0.001 m^2 RCS.

angles. Suspended power lines between two towers conform to a catenary whose sag in the middle is a function of tower separation, tensile strength, temperature, and ice loading. This sag can be as high as 6 m. For high incidence angels, depending on the radar range resolution, power lines are mapped as a straight lines between the two towers. For example a power line with 6 m sag in the middle is within one range resolution of 30 cm for incidence angles higher than 85°. Using the photo images, the

location of towers and power lines were identified in the radar scenes. (See Figure 4.9). The scattering matrices of 21 linear regions, 2 pixel wide and almost 1000 pixel long ($N \approx 2000$), in the seven radar images along the power line segments were extracted. Also similar scattering matrices were extracted from clutter regions within each image. The results are summarized in Table 4.1 where the backscatter power in VV and HV channels together with VV-HV and HH-HV coherence and their sum for both power line and clutter regions are reported. In all cases examined backscattering coefficient of clutter $\sigma^0_{VV} < -10dB$ and the ratio of cross- to co-polarized backscatter $\sigma^0_{HV}/\sigma^0_{VV} < -10dB$. Use of any single or combined backscatter power does not result in an effective detection. On the other hand the proposed detection algorithm based on co- to cross-polarized backscatter coherence clearly identifies the power lines in all 21 regions. In these examples the signal-to-clutter ratio ranges from 2 to 10 depending on the power lines and their background clutter. As expected, signal-to-clutter ratio for power lines illuminated at low aspect angles is higher than those illuminated at high aspect angles. Figures 4.8 and Figure 4.9 show a typical aerial photograph and the corresponding SAR image that includes a power line. Power lines are not visible, however, the tower supporting the power line are somewhat discernible. Figure 4.9 shows the same SAR image after the detection process where the location of power lines are indicated.

4.6 Conclusions

Problem of power line detection in polarimetric SAR images was considered in this chapter. Performance of a statistical polarimetric detection algorithm was evaluated using seven polarimetric SAR scenes at Ka-band. Analytical formulations for the calculation of false alarm rate and probability of detection in terms of number of independent samples and the coherence of pixels which include power line were obtained. It was shown that the PD and FAR are both improved by increasing the frequency and decreasing the resolution of the SAR system. It was also shown that the power line coherence decreases at higher aspect angles (angle between flight path and power line direction) which results in lower PD. In the examples considered here, the detection algorithm successfully identified all 21 power line segments in the SAR images.

		(1) $\langle\lvert S_{vv}\rvert^2\rangle$	(2) $\langle\lvert S_{vh}\rvert^2\rangle$	(3) $\frac{\langle S_{vv}S_{vh}^*\rangle}{\sqrt{\langle\lvert S_{vv}\rvert^2\rangle\langle\lvert S_{vh}\rvert^2\rangle}}$	(4) $\frac{\langle S_{hh}S_{hv}^*\rangle}{\sqrt{\langle\lvert S_{vv}\rvert^2\rangle\langle\lvert S_{vh}\rvert^2\rangle}}$	(5) (3) + (4)
Image 1	Power line 1	3.80e-2	2.73e-3	6.13e-2	4.74e-2	1.08e-1
	Power line 2	2.69e-2	1.68e-3	8.43e-2	4.18e-2	1.02e-1
	Power line 3	4.05e-2	2.91e-3	6.26e-2	3.96e-2	1.19e-1
	Clutter 1	4.14e-2	2.29e-3	2.01e-2	1.18e-2	2.59e-2
	Clutter 2	3.98e-2	2.59e-3	1.12e-2	2.48e-2	1.78e-2
	Clutter 3	2.77e-2	1.81e-3	4.07e-2	3.11e-2	6.96e-2
Image 2	Power line 1	4.23e-2	3.14e-3	6.62e-2	5.80e-2	1.22e-1
	Power line 2	3.84e-2	3.19e-3	7.54e-2	6.44e-2	1.38e-1
	Power line 3	4.37e-2	3.16e-3	8.07e-2	6.08e-2	1.38e-1
	Clutter 1	2.39e-2	1.74e-3	6.22e-3	2.02e-2	2.58e-2
	Clutter 2	4.08e-2	2.60e-3	1.07e-2	4.36e-2	4.15e-2
	Clutter 3	1.56e-2	1.21e-3	2.93e-2	3.75e-2	6.55e-2
Image 3	Power line 1	3.07e-02	2.62e-0	2.45e-01	3.11e-01	5.50e-01
	Power line 2	2.47e-02	2.58e-03	1.73e-01	1.76e-01	3.39e-01
	Power line 3	2.65e-02	2.68e-03	1.86e-01	2.68e-01	4.30e-01
	Clutter 1	1.75e-02	2.08e-03	6.19e-02	2.65e-02	6.35e-02
	Clutter 2	1.87e-02	1.89e-03	2.74e-02	1.23e-02	3.65e-02
	Clutter 3	1.86e-0	2.03e-03	6.57e-02	4.46e-02	2.13e-02
Image 4	Power line 1	4.31e-02	2.65e-03	4.19e-01	4.17e-01	8.16e-01
	Power line 2	1.88e-02	2.07e-03	1.89e-01	2.16e-01	4.04e-01
	Power line 3	3.89e-02	2.78e-03	4.30e-01	4.73e-01	8.82e-01
	Clutter 1	9.97e-03	1.71e-03	7.62e-02	6.40e-02	1.09e-01
	Clutter 2	9.04e-03	1.63e-03	5.17e-02	2.95e-02	5.83e-02
	Clutter 3	1.03e-02	1.69e-03	4.63e-02	5.03e-02	8.70e-02
Image 5	Power line 1	4.23e-02	3.25e-03	1.67e-01	1.54e-01	3.06e-01
	Power line 2	2.84e-02	2.73e-03	5.33e-02	4.99e-02	1.02e-01
	Power line 3	4.87e-02	2.98e-03	2.27e-01	2.39e-01	4.51e-01
	Clutter 1	2.82e-02	2.32e-03	3.75e-02	1.81e-02	4.71e-02
	Clutter 2	2.86e-02	2.58e-03	3.62e-02	5.56e-02	6.21e-02
	Clutter 3	2.03e-02	2.05e-03	4.18e-02	4.58e-02	5.48e-02
Image 6	Power line 1	2.47e-02	2.46e-03	9.48e-02	7.23e-02	1.53e-01
	Power line 2	1.40e-02	1.76e-03	1.31e-01	1.09e-01	2.24e-01
	Power line 3	1.92e-02	2.06e-03	1.06e-01	5.02e-02	1.42e-01
	Clutter 1	1.10e-02	1.90e-03	3.70e-02	4.20e-02	1.44e-02
	Clutter 2	1.25e-02	1.83e-03	4.49e-02	8.46e-02	4.03e-02
	Clutter 3	1.05e-02	1.53e-03	7.77e-02	7.43e-02	2.17e-02
Image 7	Power line 1	8.50e-3	2.14e-3	4.72e-2	7.99e-2	1.23e-1
	Power line 2	9.59e-3	2.15e-3	8.17e-2	9.23e-2	1.73e-1
	Power line 3	1.24e-2	2.38e-3	1.76e-1	8.11e-2	2.57e-1
	Clutter 1	7.53e-3	1.89e-3	1.70e-2	2.62e-2	1.54e-2
	Clutter 2	7.53e-3	1.88e-3	3.12e-2	3.78e-2	6.83e-2
	Clutter 3	7.08e-3	1.87e-3	2.78e-2	1.65e-2	3.49e-2

Table 4.1: Performance of the proposed polarimetric detection algorithm. For each image compare the first 3 entries of column (5) with the next 3 entries. It is also shown that detection based on the comparison of backscatter power of clutter and power line is not possible.

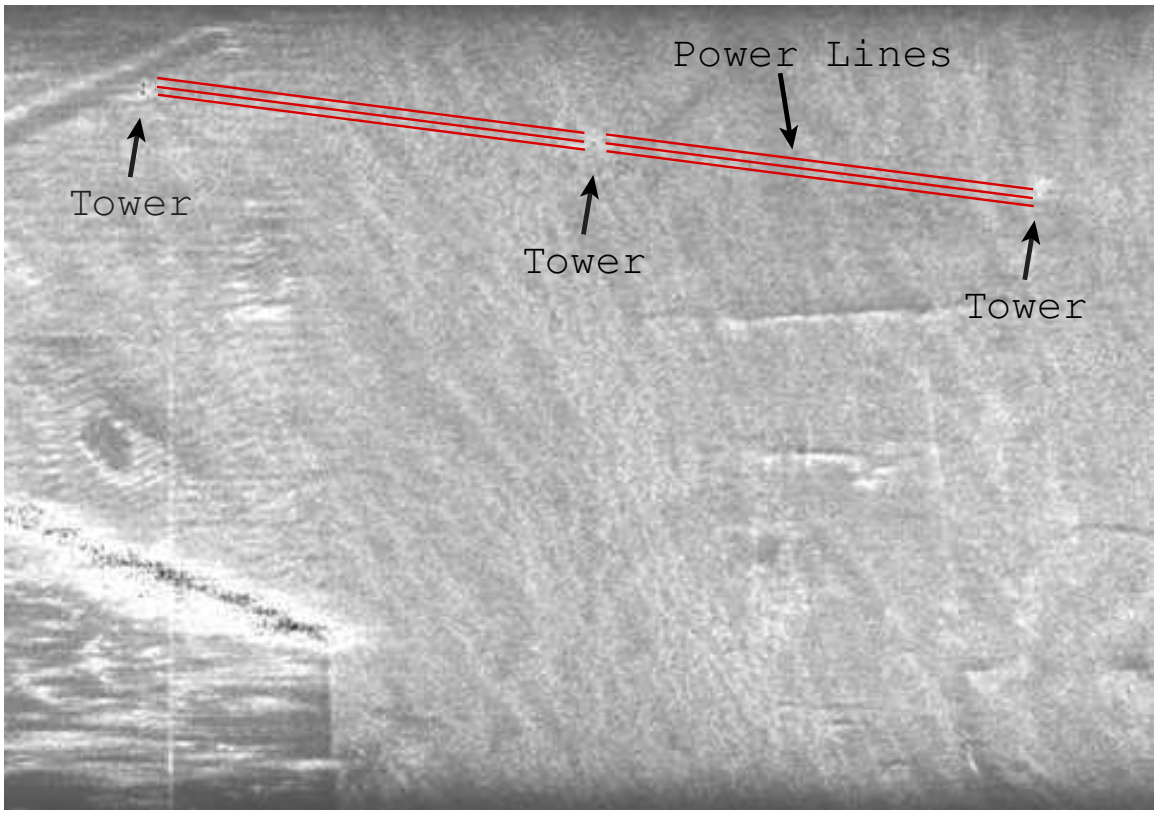

Figure 4.11: The SAR image shown in Figure 4.9 after detection of power lines.

CHAPTER 5

MILLIMETER-WAVE RADAR SIMULATOR FOR POWER LINE DETECTION

5.1 Introduction

With recent advancements in semiconductor technologies, reliable and relatively inexpensive millimeter-wave (MMW) radars are now attainable. Since millimeter-wave radar enjoy a number of advantages over other sensors, namely, high resolution, nearly all-weather capabilities, and compactness, they become viable sensors for many Reconnaissance, Surveillance, and Target Acquisition (RSTA) missions, especially at near grazing incidence.

Similar to other sensors, the successful application of MMW radars is measured by its ability to detect targets in the presence of clutter. In particular, power lines pose a real threat of collision to low-flying aircrafts and helicopters due to their very low backscatter cross-section, both at visible and millimeter-wave (MMW) wavelengths.

In this Chapter, we propose a technology for making power lines visible using millimeter-wave radar and special processing algorithms. A simulator is developed to test the idea in various real-world scenarios.

The work in the previous Chapters includes work on the initial algorithm using

simulation with SAR (Synthetic Aperture Radar) images, where the concept was validated with theoretical model of the power line backscatter for many different power lines under different conditions, including precipitation and vegetation clutter. These measurement have given us confidence in our original concept and a simulator was developed that is based on a real-aperture radar flying above a landscape with a power line cutting across it.

The details of simulator are given in Section 5.2, and Section 5.3, show typical simulation run, with the detection of the power line clearly shown. Lastly, Section **??** summarizes and gives the proposed idea for improving the simulator in the future.

5.2 Near-Grazing Millimeter-Wave Simulator

5.2.1 Simulator Introduction

Development of the simulator is based on the idea of simulating the motion and radar of a low-flying helicopter. A clutter map of an area is generated, and a power line is positioned anywhere within the scene. The helicopter then flies over the scene, collecting polarimetric backscatter data for each radar pulse and forming an image based on averaging data from successive pulse. In this way, as the helicopter flies over the scene a fairly detailed image is built up.

The clutter map of the scene consists of a raster image with images that specify the kind of clutter at each location. For instance, in the present simulation we have water, (a river) road, grass, and trees. The power line is placed into this clutter map separately and is not rasterized in any way. The backscatter from the tower is not yet

included in this simulator. Given the map , we can now specify a route over which the helicopter flies as if on a reconnaissance mission.

5.2.2 Simulator Algorithm

In order to accurately simulate the received power due to a transmitted pulse, we start with radar equation [54]:

$$P_r = \frac{P_t G^2 \lambda^2 \sigma_t}{(4\pi)^3 R^4} \tag{5.1}$$

where the power received, P_r, is equal to the power transmitted, P_t, scaled by the two-way antenna gain, G^2, the wavelength-squared, which is referred to the center frequency of the radar and the radar cross section of the target, σ_t, all divided by the range spreading loss factor, where R is range to the target. Because the radar knows R for each because it knows the round-trip time it can compensate for this factor in its processing algorithm, and present normalized powers to the pilot. Similarly for all the other parameters except for the target's radar cross section, σ_t. Hence, the radar simulator comes down to using the radar cross section (RCS) of each target in order to form an image. For the vegetation clutter, this further reduces to using the area-normalized radar backscatter coefficient, σ^o, which is reported in the literature for various targets.

However, in order to allow this algorithm to work, we do not receive the power but the complex amplitude of the pulse. Hence we work with complex scattering matrix of a target as specified in the following equation [32]:

$$\begin{bmatrix} E_v^r \\ E_h^r \end{bmatrix} = \frac{1}{4\pi R^2} \begin{bmatrix} S_{vv} & S_{hv} \\ S_{vh} & S_{hh} \end{bmatrix} \begin{bmatrix} E_v^t \\ E_h^t \end{bmatrix} \tag{5.2}$$

where the subscript h and v refer to the linear polarization of the electric field either horizontal or vertical respectively. In this equation the received electric field is equated to a scaled version of the transmitted electric field, where the matrix of S-terms is known as the scattering matrix where each element is complex. The radar is assumed to measure all these complex quantities.

For the pixels where there is also a power line, the backscatter values for the clutter and power line must be summed. This can be accomplished with the following equation:

$$s_{total} = s_{clutter} + 4\pi A\, S_{powerline} \tag{5.3}$$

where $s = S/4\pi A$ is an area-normalized scattering matrix element (with the area being that of the map pixel), and $S_{powerline}$ is due to the total backscatter from the power line with any area normalization.

The above procedure allows us to calculate the normalized scattering matrix elements, s, for each pixel of the radar. Now we discuss what is involved in calculating the image data that the radar would generate, and how we can use successive images to reduce speckle as the helicopter continues to fly.

Several assumptions are made at this stage: (1) the radar element is same as the power line: (2) the radar incidence angle on the clutter is nearly grazing, and so we use the same mean backscatter values: (3) the elevation beamwidth is ignored: (4)

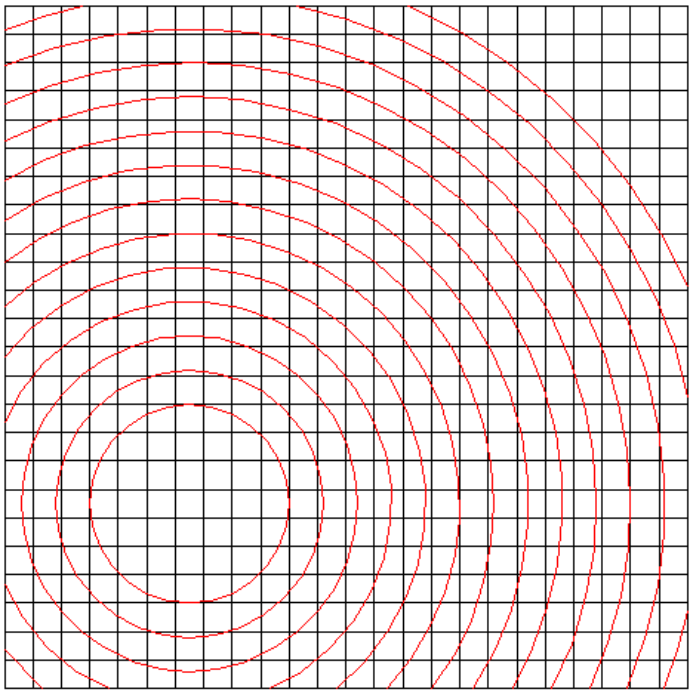

Figure 5.1: Map raster in black overlain with radar grid in red. This shows that value for each radar pixel is derived from the backscatter of the clutter in one or more map pixels.

there is propagation loss through the vegetation: there is no propagation loss through the vegetation; and (5) the radar does not move while collecting data; its location is the same for transmitting and receiving pulse.

Given the radar location, we can imagine a range-theta grid spreading out from that origin across the raster landscape. For each grid cell in the range-theta grid we can calculate the clutter scattering matrix values as a simple sum of those from each of map grid cells that it overlays. (See Figure 5.1)

In this way, we can calculate the scattering matrix values for every grid cell in the range-theta grid. We now resample this grid to the map grid, so we have our best guess as to the scattering matrix value for each grid of our map. At this stage we store these values in different form, called the Mueller Matrix, which facilitate the averaging we plan on doing in the next step. The modified Mueller matrix (hereafter known as the Mueller Matrix) is given by [55]:

$$\mathcal{L}_m = \begin{bmatrix} \langle |S_{vv}^2| \rangle & \langle |S_{vh}^2| \rangle \\ \langle |S_{hv}^2| \rangle & \langle |S_{hh}^2| \rangle \\ 2\langle \mathcal{R}e\{S_{vv}^* S_{hv}\} \rangle & 2\langle \mathcal{R}e\{S_{vh}^* S_{hh}\} \rangle \\ 2\langle \mathcal{I}m\{S_{vh}^* S_{vv}\} \rangle & 2\langle \mathcal{I}m\{S_{vh}^* S_{hh}\} \rangle \end{bmatrix}$$
$$\begin{bmatrix} \langle \mathcal{R}e\{S_{vh}^* S_{vv}\} \rangle & -\langle \mathcal{I}m\{S_{vh}^* S_{vv}\} \rangle \\ \langle \mathcal{R}e\{S_{hh}^* S_{hv}\} \rangle & -\langle \mathcal{I}m\{S_{hh}^* S_{hv}\} \rangle \\ \langle \mathcal{R}e\{S_{vv}S_{hh}^* - S_{vh}S_{hv}^*\} \rangle & \langle \mathcal{I}m\{S_{vh}S_{hv}^* - S_{vv}S_{hh}^*\} \rangle \\ \langle \mathcal{I}m\{S_{vv}S_{hh}^* - S_{vh}S_{hv}^*\} \rangle & \langle \mathcal{R}e\{S_{vv}S_{hh}^* - S_{vh}S_{hv}^*\} \rangle \end{bmatrix} \tag{5.4}$$

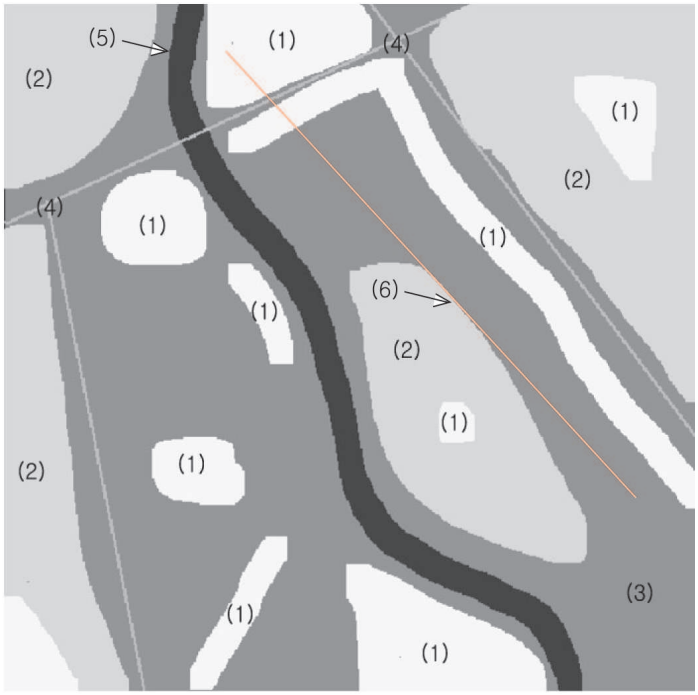

Figure 5.2: Map raster showing the different classes of clutter: (1) trees (2) grass (3) bare soil (4) roads (5) water (6) power line

where the $\langle \cdot \rangle$ denotes ensemble average. When the helicopter moves to the next position in its flight path we repeat the process, but this time we average the new Mueller Matrix values in the map grid with the previous values. In this way we can remove speckle through this averaging process, which is a fairly standard method for de-speckling radar data.

It turns out that one of these matrix entries is very special when averaged for natural targets it tends toward zero, but not for man-made targets, such as a power line. Given that we know the amount of averaging we have done for each pixel, we can develop a detection algorithm that levels each pixel as a power line, or not with a known detection probability. This special Mueller Matrix entity is: $S_{vv}S_{vh}^{*}$, where $(\cdot)^{*}$ represents complex conjugation. The intuition for why averaging this

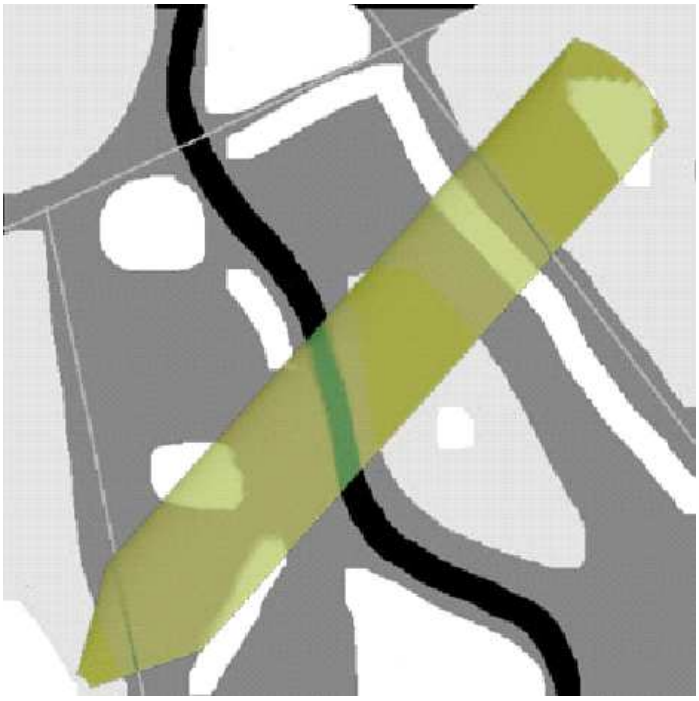

Figure 5.3: Map raster showing the normalized backscattered power values after complete simulation. This simulation was performed at 35 GHz and the *hh*-polarized power was mapped to the red channel. The original map is also displayed in gray scale for context. Note that the power line is not visible.

drives it to zero for vegetation but not for man-made targets is as follows. This value represents a kind of correlation between the backscatter at a co-polarized and a cross-polarized direction. For vegetation, this correlation gets washed out due to the variety of branch and leaf angles in any natural vegetation, especially from different illumination directions and different vegetation shape due to wind. For man-made targets, and in particular for power lines, there is very little variety in angles between scattering centers, and so this value stays at a relatively high level despite changes in viewing geometry.

The remainder of the simulation merely continues to compute single-look real-aperture radar images and average them in with the current estimate for each map

pixel. A sample simulation is shown in Section 5.3. Because the accurate simulation of the power line is critical, we now give an overview of our work in measuring real power lines under various conditions.

5.3 Simulation

This Section shows the results from a sample simulation. We detail the landscape used, the power line, and the helicopter parameters that went into the simulation. Then we will show some snapshots at different times during the simulation, showing the progress of the helicopter over the landscape and the eventual detection of the power line.

The map raster we used is shown in Figure 5.2. This represents a 10 Km $\times$ 10 Km region. The five clutter types used are: water (river), roads, bare soil, grass, and trees. This landscape was drawn by hand. The pixel size is 10 meters square. We use 35 GHz as our operating frequency, hence we used data from our efforts in near-grazing MMW phenomenology [30] as our average Mueller Matrix values for each of the clutter types.

The power line was inserted into the map raster as one straight segment cutting across the landscape as shown in red in Figure 5.2.

Figure 5.3 shows backscattered power data after the helicopter flight is over. The effects of speckle can be seen along the edges where the averaging stays fairly low due to lack of repeated illumination by the radar. Here the power values are noisy enough that the classification algorithm performs poorly. Thankfully, this is fairly

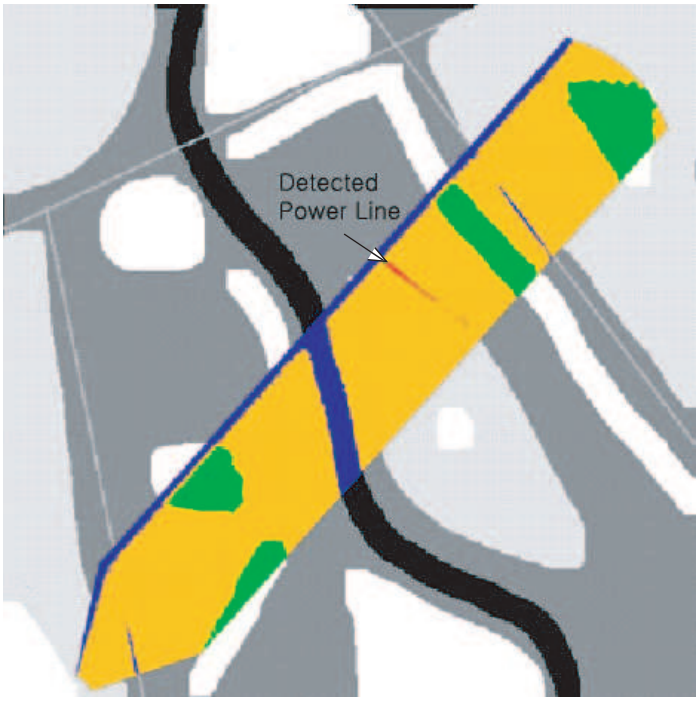

Figure 5.4: Map raster showing the land-cover classified map based on the radar data after a complete simulation. Blue is flat vegetation (water, roads), brown is bare soil, yellow is grass, green is trees, and red is the detected power line. The original map is also displayed in grey-scale for context.

small and hence inconsequential part of the data. As can be seen the data toward the center of the radar beam is the least noisy. Figure 5.4 shows the classified data after the helicopter flight is over. The classification accuracy of the clutter for the clutter is quite good with trees, short vegetation, and water being accuracy separated. The signal-to-clutter ratio for the power line at vv-polarization is 0 dB, and hence is undetectable in the power data. Despite this, use of the detection metric allows the power line to be easily detected as shown in red after 50 or more pulses are averaged. Note that not all of the power line was detected. This is due to incidence angle effects and more work need to be done for improving the detection of power lines.

5.4 Conclusions

It is believed that this simulator shows that the idea has promise for future implementation on operational helicopters. Future work should be concentrated on making simulator more realistic; (1) include elevation antenna pattern effects, and hence include local incidence angle effects for the clutter and include elevation changes in the ground; (2)include correlated speckles based on a realistic model; (3) include losses through vegetation; (4) include natural "texture" in clutter backscattered values; and (5) add buildings and other man-made structures and the ability to discern power lines as different than these other man-made targets.

CHAPTER 6

MILLIMETER-WAVE REAL APERTURE IMAGING RADAR FOR COLLISION AVOIDANCE

6.1 Introduction

Collision avoidance is of great concern to all aircraft, requiring the detection of hazardous terrain or obstacles in sufficient time for clearance maneuvers. The collision avoidance is even more demanding for helicopters, as their unique capability result in excessive operations at low-altitude, near to terrain and other obstacles. Among all the obstacles, power lines are most difficult to detect due to their small radar cross sections. Millimeter-wave polarimetric radar satisfies many of the criteria required of a sensor in high performance power line detections. The short wavelength, compared to microwave radar provides high resolution measurements. Millimeter-wave radar are also able to operate in adverse weather and environment conditions compared to optical sensors such as lasers. With modern signal processing technique and advances in the semiconductor technology, it is possible to locate/detect targets at greater distance than other sensors with high degree of accuracy. The high bandwidth of millimeter-wave radar allows measurement of sufficient range and resolution

to maintain high quality radar operation. Extra information can be extracted from the polarization of radar signal to enable targets of interest discriminated from clutter.

In this study, a 94 GHz high resolution polarimetric real aperture imaging radar is built and its perception capability in traffic environment is demonstrated. It was shown that radar images can be acquired, which represent a highly information basis for the interpretation of the traffic scenes. A detailed discussion of the radar system's design and performance is presented in this Chapter. Hardware aspect of the system is discussed as well as the software for the radar operation and radar image processing. Images are generated for the simulated traffic scenes: (1)a scene of civilian vehicles and pedestrians, (2)a scene of military vehicle convoys, (3)a scene of gravel road, (4)a scene of power line with background clutter of summer vegetation, (5)a scene of power line with background clutter of winter vegetation. The imaging performance of the traffic scenes are investigated.

6.2 System Description and Signal Processing

In this Section, radar hardware and signal processing technique used for the generation of polarimetric radar images from traffic scenes are discussed. In general, polarimetric radar can be categorized into three major groups : (1) coherent radars, (2) incoherent radars, and (3) coherent-on-receive radars. Phase-coherence measurement is not possible when the radar platform is moving, as the fluctuation of radar platform is comparable or even greater than the wavelength of the radar operating frequency (94 GHz). The coherent-on-receive mode is radar polarimetric configura-

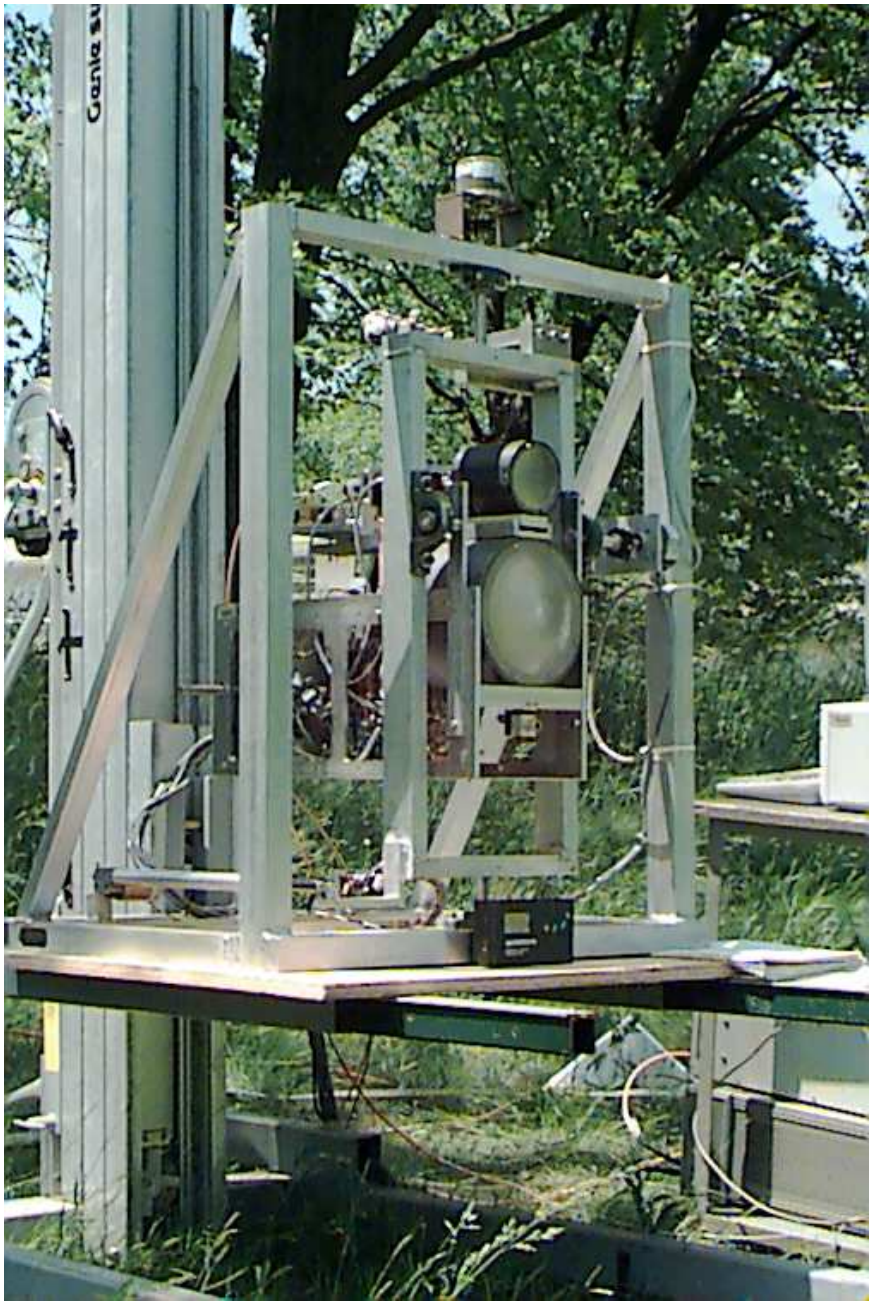

Figure 6.1: The University of Michigan 94 GHz fully polarimetric radar system set up in the Willow Run Airport test site for generating images of traffic scenes with power line.

tion where instead of measuring the scattering matrix, modified Mueller matrix is measured. In this thesis, the polarimetric imaging radar is operated in this mode. The scattering matrix is obtained form this modified Mueller matrix and the system is immune to the fluctuation of the radar platform. From the scattering matrix data, radar backscattering for any set of transmit- and receive-polarization pair can be calculated. The concept of the coherent-on-receive radar is briefly discussed here. By defining a set of orthogonal directions ($\hat{v}$, $\hat{h}$) in a plane perpendicular to the direction of propagation, the component of the scattered field $\mathbf{E}^s$ from a given target can be related to the components of the incident wave $\mathbf{E}^i$ through the scattering matrix of the target, i.e.,

$$\mathbf{E}^s = \frac{e^{ik_0 r}}{r} \begin{bmatrix} S_{vv} & S_{vh} \\ S_{hv} & S_{hh} \end{bmatrix} \mathbf{E}^i \tag{6.1}$$

where k_0 is the propagation constant and r is the range from the target to the receive antenna. In general, the polarization state of the transmitted wave can be any arbitrary elliptical polarization. An elliptically polarized wave can be characterized by two angles known as the rotation angle (ψ) and ellipticity angle (χ). It is also shown that the modified Stokes vector $\mathbf{F}_m(\psi, \chi)$ provides an alternative but equivalent representation of wave polarization and that scattered (received) modified Stokes vector $\mathbf{F}_m^r$ can be related to the incident (transmitted) Stokes vector via the modified Mueller matrix, $\mathbf{L}_m$.

$$\mathbf{F}_m^r = \frac{1}{r^2}\mathbf{L}_m\mathbf{F}_m^t \tag{6.2}$$

with

$$\mathbf{L}_m = \begin{bmatrix} |S_{vv}|^2 & |S_{vh}|^2 & Re(S_{vh}^* S_{vv}) & -Im(S_{vh}^* S_{vv}) \\ |S_{hv}|^2 & |S_{hh}|^2 & Re(S_{hh}^* S_{hv}) & -Im(S_{hv}^* S_{hh}) \\ 2Re(S_{vv}S_{hv}^*) & 2Re(S_{vh}S_{hh}^*) & Re(S_{vv}S_{hh}^* + S_{vh}S_{hv}) & -Im(S_{vv}S_{hh}^* - S_{vh}S_{hv}) \\ 2Im(S_{vv}S_{hv}^*) & 2Im(S_{vh}S_{hh}^*) & Im(S_{vv}S_{hh}^* + S_{vh}S_{hv}) & Re(S_{vv}S_{hh}^* - S_{vh}S_{hv}) \end{bmatrix}$$

For a given transmit polarization specified by the rotation angle ψ_t and ellipticity angle χ_t, the antenna modified Stokes vector $\mathbf{A}_m^t$ is given by $\mathbf{F}_m^t$ notarized by total intensity I_0

$$\mathbf{A}_m^t = \frac{\mathbf{F}_m^t}{I_0} = \begin{bmatrix} \frac{1}{2}(1 + \cos 2\psi_t \cos 2\chi_t) \\ \frac{1}{2}(1 - \cos 2\psi_t \cos 2\chi_t) \\ \sin 2\psi_t \cos 2\chi_t \\ \sin 2\chi_t \end{bmatrix} \tag{6.3}$$

A similar definition applies to $\mathbf{A}_m^r$ for the receive antenna, and in terms of the tow vectors, the polarization synthesis equation is given by,

$$\sigma^0(\psi_r, \chi_r; \psi_t, \chi_t) = 4\pi \mathbf{A}_m^r \mathbf{T}\mathbf{L}_m\mathbf{A}_m^t \tag{6.4}$$

where $\mathbf{T}$ is a transformation matrix given by,

$$\mathbf{T} = \begin{bmatrix} 1 & 0 & 0 & 0 \\ 0 & 1 & 0 & 0 \\ 0 & 0 & 1/2 & 1 \\ 0 & 0 & 0 & -1/2 \end{bmatrix}. \tag{6.5}$$

At lease 4 measurements should be made to build the modified Mueller matrix with 16 entries. Four different polarizations can be chosen; namely, vertical, 45° linear, right-hand circular (RHC), and left-hand circular (LHC). The Stokes vectors of the 4 chosen polarizations are given by

$$\mathbf{F}^t_V = \begin{bmatrix} 1 \\ 0 \\ 0 \\ 0 \end{bmatrix}, \quad \mathbf{F}^t_{45} = \begin{bmatrix} 1/2 \\ 1/2 \\ 1 \\ 0 \end{bmatrix}, \quad \mathbf{F}^t_{LHC} = \begin{bmatrix} 1/2 \\ 1/2 \\ 0 \\ 1 \end{bmatrix}, \quad \mathbf{F}^t_{RHC} = \begin{bmatrix} 1/2 \\ 1/2 \\ 0 \\ -1 \end{bmatrix} \tag{6.6}$$

By denoting the ith column of the modified Mueller matrix by $\mathbf{L}^i_m$, the Mueller matrix is given by

$$\begin{aligned} \mathbf{L}^1_m &= \frac{1}{r^2}\mathbf{F}^r_V \\ \mathbf{L}^2_m &= \frac{1}{r^2}\left[\mathbf{F}^r_{LHC} + \mathbf{F}^r_{RHC} - \mathbf{F}^r_V\right] \\ \mathbf{L}^3_m &= \frac{1}{r^2}\left[\mathbf{F}^r_{45} - \frac{1}{2}(\mathbf{F}^r_{LHC} + \mathbf{F}^r_{RHC})\right] \\ \mathbf{L}^4_m &= \frac{1}{r^2}\left[\frac{1}{2}(\mathbf{F}^r_{LHC} - \mathbf{F}^r_{RHC})\right] \end{aligned} \tag{6.7}$$

where $\mathbf{F}^r_p$ represents the received Stokes vector corresponding to the transmit polarization p.

The instrumentation radar is designed as flexible as possible such that the operation parameters can be varied in wide range in order to find the optimum conditions. The radar system uses a vector network analyzer for IF base for transmitter and receiver. An RF unit is designed to up-convert the signal from the network analyzer signal to 94 GHz and down-convert the radar returned signal back to the IF. The block diagram of the RF unit is shown in Figure 6.2. An X-band source is used as the fundamental source whose frequency is one eighth of the desired frequency of the local oscillator for the up- and down-conversion. This X-band signal is amplified to about 30 dBm and then splitted into two branches where one feeds the transmitter module and the other feeds the transceiver module. Phase coherence is maintained because the up-conversion and down-conversion is driven by the same signal source. The transmit signal leaving the X-band source is multiplied by 8 times and is injected to the Gunn oscillator after amplification. Therefore the Gunn oscillator is phase-locked to the X-band source. The chirped output of the network analyzer (IF) is up-converted to the desired transmitted signal. The RF output power of 94 GHz system is stabilized at 0 dBm. For the bistatic and coherent-on-receive modes the RF output of the transmit module is connected to the bistatic transmit antenna module and for the mono-static mode the output is connected to the transceiver module.

The bistatic transmit antenna module consists of two polarization switches and a horn antenna. The transmit polarization of the radar system in bistatic and coherent-on-receive modes is facilitated by two cascaded polarization switches. The bistatic mode transmit antenna is a lens-corrected corrugated circular horn with a Gaussian radiation pattern and beam-width 3°. In the coherent-on-receive mode the transmit

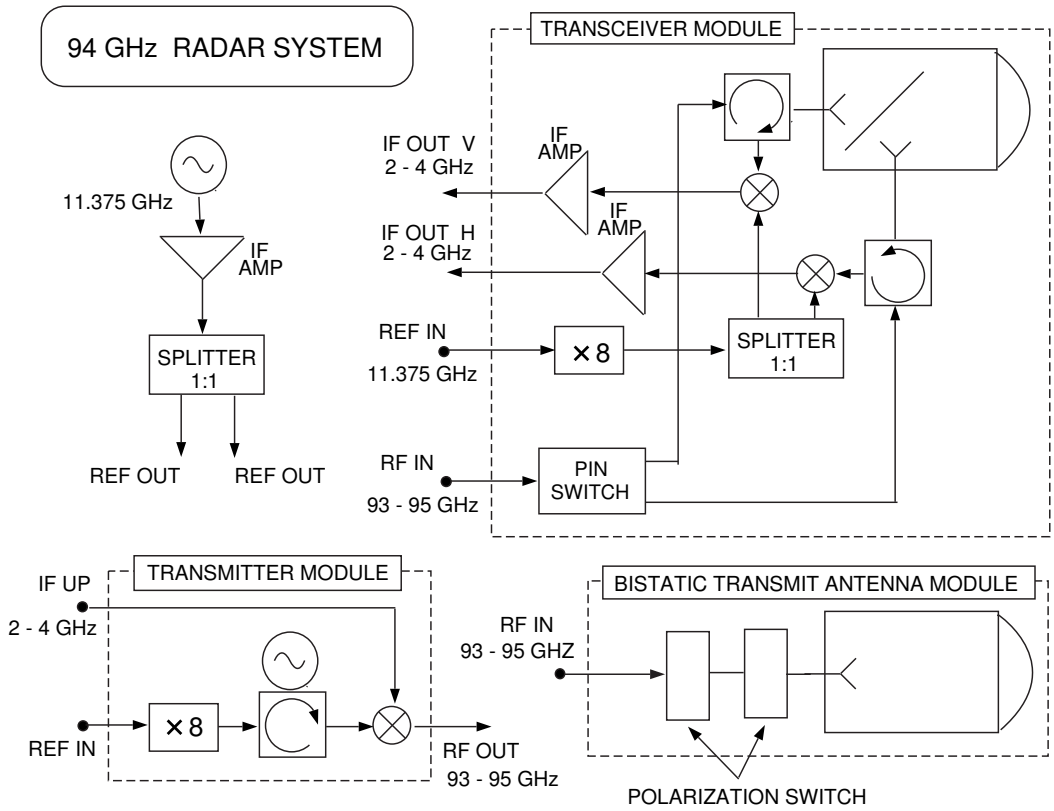

Figure 6.2: The block diagram of the RF unit of The University of Michigan 94 GHz polarimetric radar system.

module is used in either backscatter or bistatic mode to transmit a number of prespecified polarizations. The transceiver module is designed to operate as a transmitter and a receiver in the mono-static configuration as well as a receiver in the bistatic configuration. This module is comprised of a dual polarized antenna, a pair of mixers, a pair of IF amplifiers, a $\times 8$ multiplier and a splitter. In addition, a SPDT PIN switch and a pair of circulators are included for mono-static operation. The antenna of the 94 GHz transceiver uses two separated corrugated horns and a polarization wire grid between the horns and the lens. The beam-width of this antenna is 1.4° after lens correction. In mono-static mode the RF output of the transmitter module is connected to the RF input of the transceiver module via a waveguide. Using the

Rotation Angles	**V**	**H**	**45°**	**135°**	**LHC**	**RHC**
α_1	0	45	0	0	45	-45
α_2	0	45	45	-45	0	0

Table 6.1: Dielectric cards rotational angles for the desired polarization states of the transmitted waves.

PIN switch the desired transmit polarization (V or H) is selected. The receiver local oscillator, similar to the transmitter LO, is phase-locked by the reference X-band source. Using two balanced mixers the received signals in both V and H channels are down-converted to IF frequency and then amplified before going to the network analyzer for further analysis and data transfer.

The transmit signal can be polarized arbitrarily using a polarizer developed in this research. The structure of polarization switch is shown in Figure 6.3 which consists of a circular waveguide with an inserted thin dielectric card that is rotatable within the waveguide. The thickness and dielectric constant of the dielectric card are chosen such that the reflected field is minimal over the desired bandwidth of operation. The polarization state of the transmitted wave is determined by the orientation angle of the card with respect to the polarization of the incoming wave. When the incoming wave enters the polarization switch, the propagation constants for the electric fields perpendicular and parallel to the dielectric card are different. The perpendicular component travels faster than the parallel component and therefore the polarization state of the incoming wave changes. For coherence operation, the polarization switches generates only V- and H-polarized waves, while for the coherence-on-receive mode, six different polarizations (V, H, 45°, 135°, RHC, LHC) are generated. Table 6.1 gives the combination of rotational angels for the 6 polarization status.

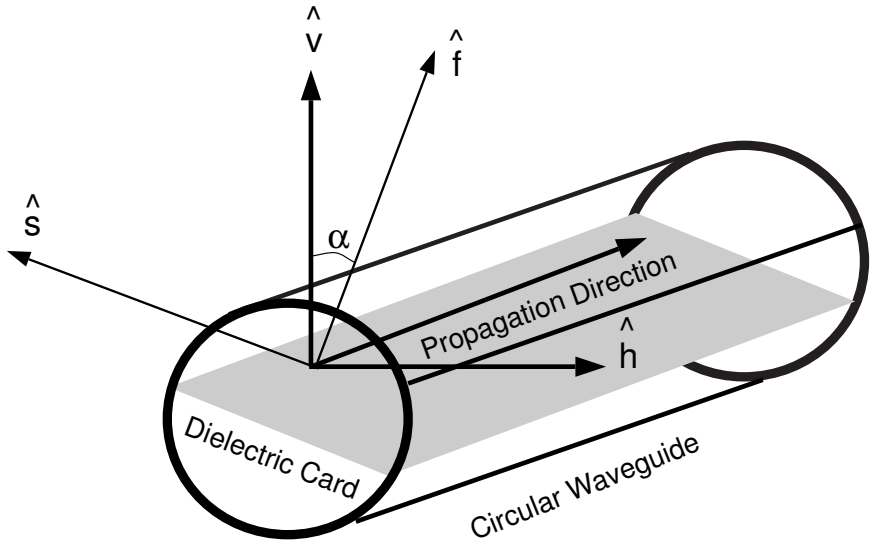

Figure 6.3: The schematic structure of the polarization switch.

An HP8753C automatic vector network analyzer with time domain capability is employed as the vector transceiver of this system in order to save time in hardware design and to ensure the flexibility in radar operation. The network analyzer has two receive ports which allow the reception of V and H channels simultaneously. The operation and measurement procedures can easily be programmed and controlled by a computer over an interface bus. A program written in *Microsoft Visual Basic* is used to set the desired parameters of the network analyzer and to collect and store data. The IF center frequency is set to 2.5 GHz and a bandwidth of 0.5 GHz is selected (the bandwidth can be as high as 1 GHz) for the range resolution of 0.3 m. In order to avoid the aliasing problem in time domain, the number of sampling points is chosen to be 201. Based on the above setting, Δf is equal to 2.5 MHz. The quantity $\frac{1}{\Delta f}$ sets the upper limit of the time-domain span without aliasing problem. In our case the upper limit for the time-domain span is 400 ns. This span covers the range up to 60 m which is sufficient for AHS applications at low grazing angles. If higher range resolution is

required, then the number of sampling also need to increase to keep the same time-domain span. In that case longer sweep time and more space for data storage will be required. The averaging function of the network analyzer can be activated to reduce the noise level of the received signal. This function is sometimes needed for low grazing angle measurements. One of the most useful processing options available with most network analyzers is the time-domain operation. Because the returned signal is measured as a function of frequency, real-time Fourier transform technique can be applied to obtain the time-domain response. In backscatter case, this result is a measure of the radar return as a function of range. By using the time-gating technique, the signal returned from the target of interest at a particular range can be isolated from the signals scattered from other objects and the leakage signal from the transmitter to receiver. The time-gated signal can then be transformed back to the frequency domain to obtain the frequency response of the target. Besides the aforementioned complicated signal processing capabilities the network analyzer also features data storage and complex math functions which are used in a calibration algorithm developed to remove systematic error in our MMW radar.

A Pentium processor-based computer is the main control unit. *Microsoft Visual Basic* creates an interactive environment for the user to operate the system efficiently. An HPIB card provides not only the communication between the network analyzer and the computer, but also the data transfer function. The combination of a motion control card and servo amplifiers gives the system the capacity of scanning in two dimensions. A computer-controlled mechanical assembly (gimbal) is built for the purpose of radar scanning in horizontal and vertical directions. The motion control

card receives commands from the user through a user interface program written in *Microsoft Visual Basic*. The pulse-form outputs of the motion control card, after being amplified by PWM servo amplifiers, are used to drive the DC motors which in turn drive the linear actuators. The motion of the linear actuator enables the radar to scan horizontally and vertically. Again, an incremental encoder is employed to monitor the amount of angle that the radar has rotated. Automatic error correction is done by the feedback circuit to the motion control card. The same mechanism is used by the polarization switch to change the polarization state of the transmitted wave. The voltages of power supplies used for the entire system are 18 V and 12 V, total current consumption is 4.5 A. Over-voltage protection circuits are implemented for every RF component. When the supplied voltage is over the rated voltage, the circuit automatically shuts off the system to protect the component and LED lights on to indicate an over-voltage situation. A solid state laser is installed parallel to the boresight direction of the radar system to facilitate pointing the radar toward the desired target such as a small calibration sphere.

For fast data transfer, the measurements are usually conducted in frequency domain. However, for generating radar images the time-domain response is needed to provide the required range information. In order to obtain the time-domain response, Fourier transform can be used. The Fourier transform is used to perform the transformation from frequency domain to time domain and vice verse. Since the data taken from the network analyzer are discrete, the discrete Fourier transform (DFT) is used in this application. There are many algorithms available to perform the DFT computation. For the present case, the chirp Z transform (CZT) is chosen based on

several advantages it can offer for the applications considered in this investigation. An imaging radar polarimeter measures the dependence of radar backscatter response as a function of both transmitted and received wave polarization states. In order to generate the polarization responses of the desired traffic scenes, the amplitude and phase of all the scattering matrix elements must be measured by transmitting and receiving in two orthogonal channels. Then for each individual pixel in the radar image a subsequent data processing is performed on the measured scattering matrices to synthesize the radar backscattering for any desired combination of transmit and receive polarizations. To achieve a fine range resolution, the bandwidth is chosen to be 0.5 GHz, which corresponds to 30 cm of range resolution. Azimuth resolution is achieved by mechanical movement of the radar assembly. Before displaying the radar image the polarimetric backscatter data is calibrated, followed by chirp Z transformation, then $1/R^2$ range dependence is removed. Polarimetric images of some traffic scene have been generated. It is shown that the backscatter responses of vehicles are significantly influenced by the transmit and receive polarizations.

6.3 Imaging Performance

Figure 6.4: The traffic scene #1 of a pedestrian, a motor bike, two passenger cars, and a pickup truck.

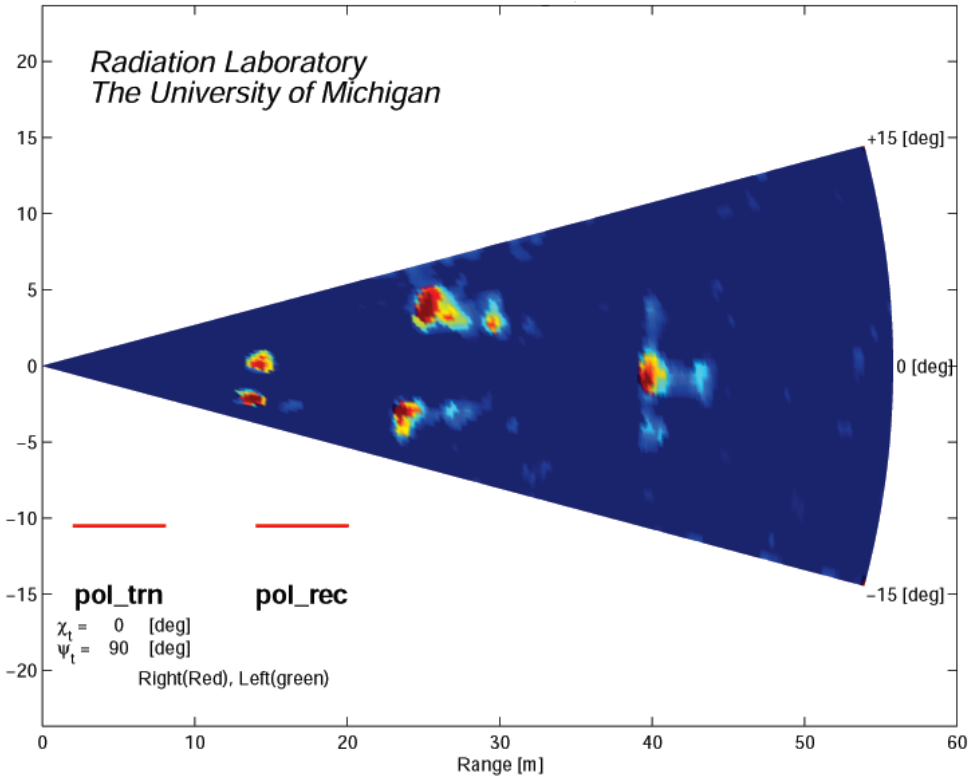

Figure 6.5: polarimetric radar image for traffic scene #1 shown in Figure 6.4. (VV-polarization)

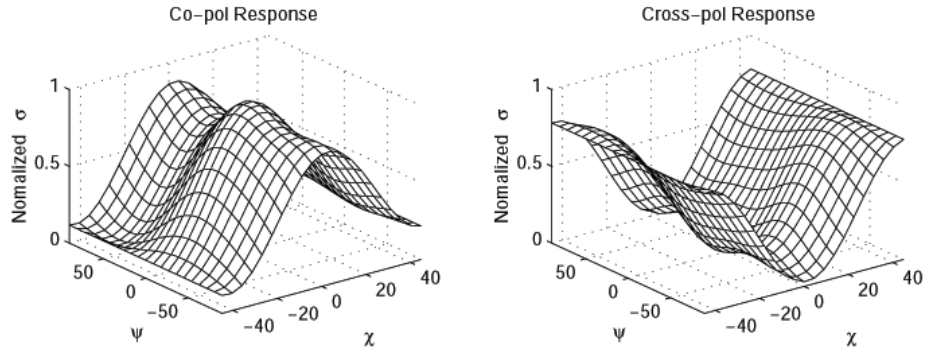

(a)Polarization Response

m_v = 0.94751		m_h = 0.95303	
m_{45} = 0.7489		m_{135} = 0.76102	
m_{lhc} = 0.57742		m_{rhc} = 0.84094	

(b)Degree of Polarization

Figure 6.6: Polarization response and degree of polarization for the pickup truck in the traffic scene #1 shown in the Figure 6.4.

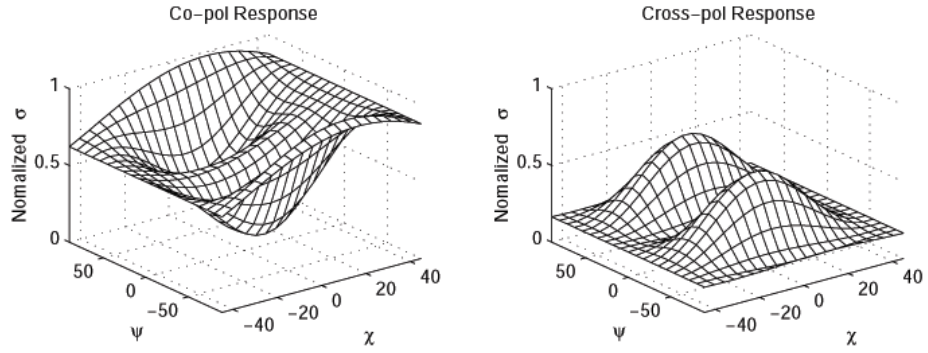

(a)Polarization Response

m_v = 0.65219		m_h = 0.72376	
m_{45} = 0.25696		m_{135} = 0.6062	
m_{lhc} = 0.70947		m_{rhc} = 0.64984	

(b)Degree of Polarization

Figure 6.7: Polarization response and degree of polarization for the ghost image due to the multipath reflection in the traffic scene #1 shown in the Figure 6.4.

Figure 6.8: The traffic scene #2 of military convoys.

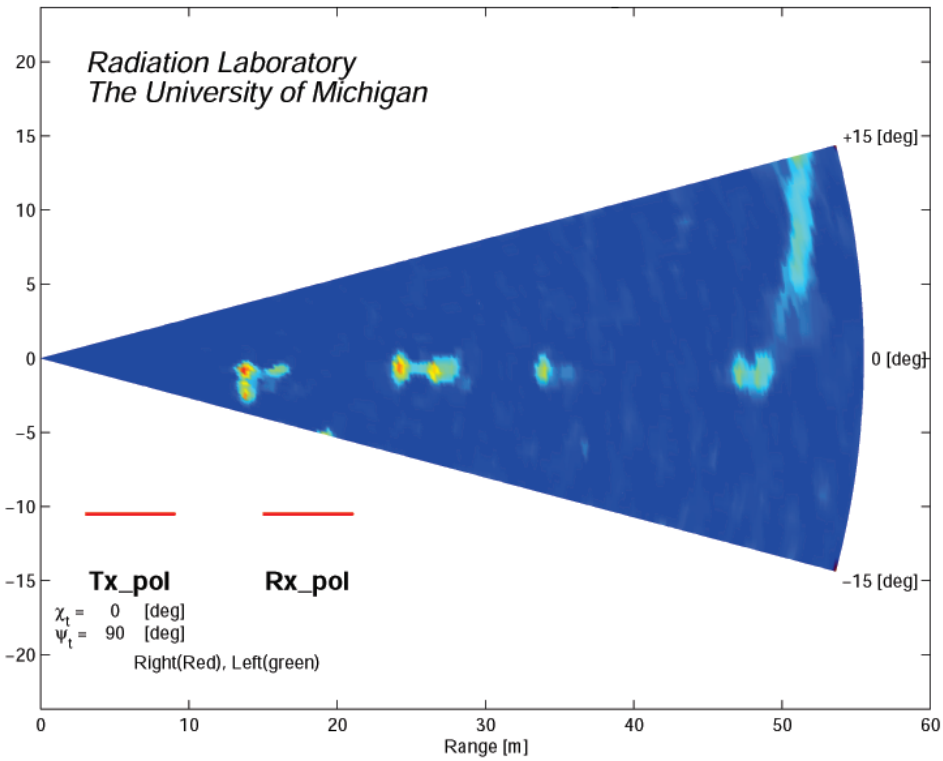

Figure 6.9: polarimetric radar image for the military convoy scene #3 shown in Figure 6.8. (HH-polarization)

Figure 6.10: The traffic scene #3 of a military convoy.

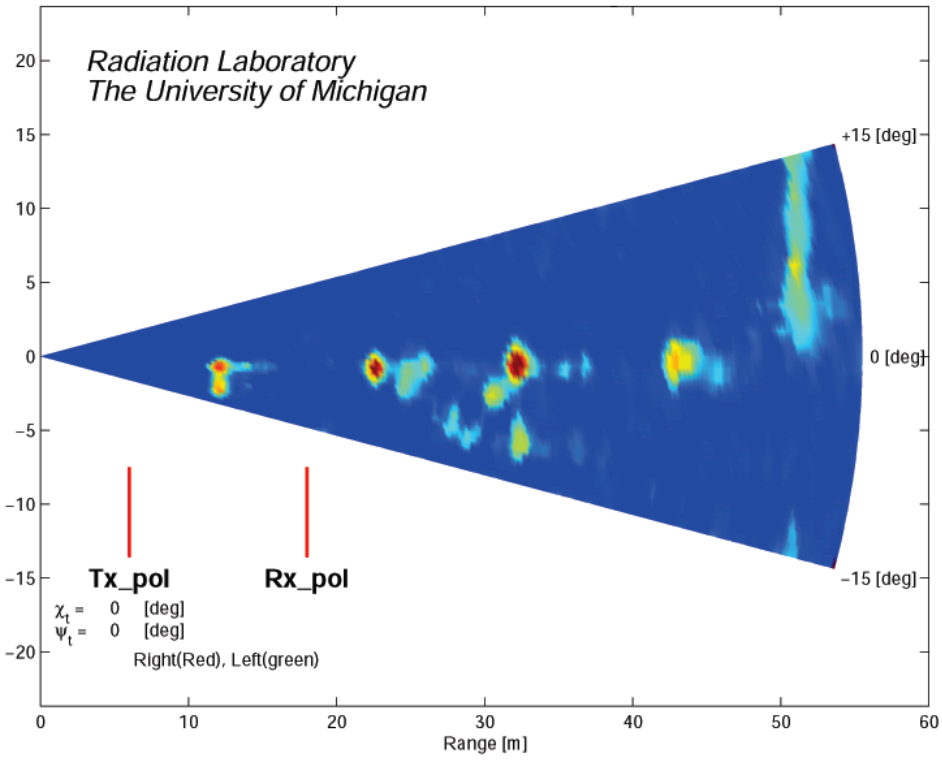

Figure 6.11: A polarimetric radar image for the military convoy scene #3 shown in Figure 6.10. (VV-polarization)

Figure 6.12: A gravel road scene in Ann Arbor, Michigan.

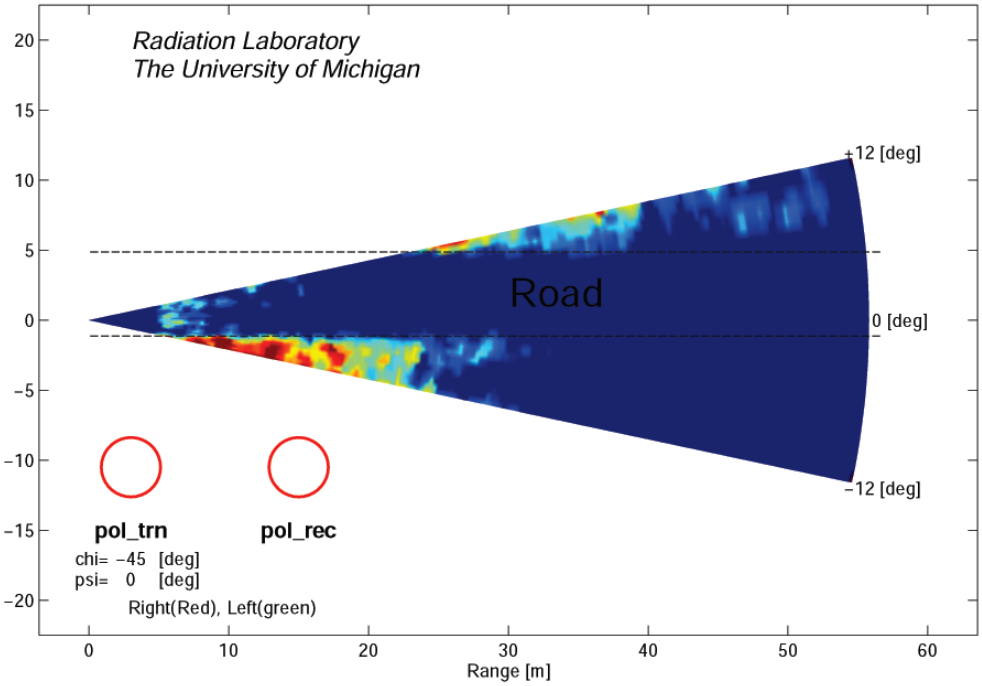

Figure 6.13: A polarimetric radar image of the gravel road scene shown in Figure 6.12. (RR-polarization)

(a)

(b)

Figure 6.14: Traffic scenes with a power line and clutter background of trees (Willow Run Airport test site) (a)Summer (Aug., 1999) (b)Winter (Nov., 1999)

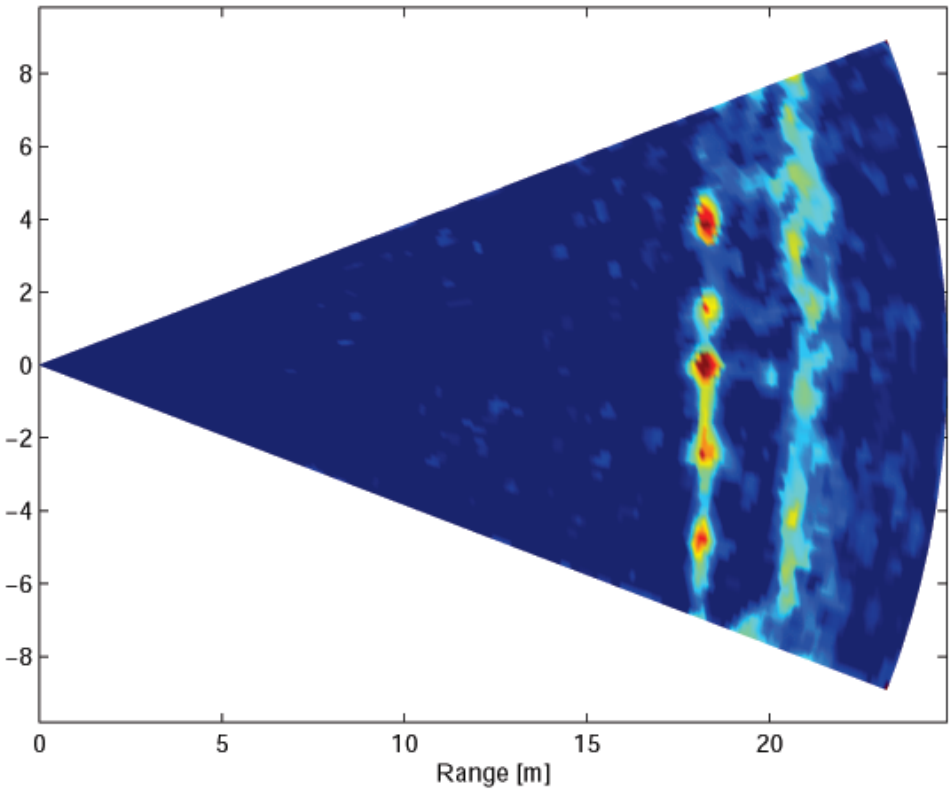

Figure 6.15: Polarimetric radar image for the power line scene with summer vegetation clutter shown in Figure 6.14(a). (VV-polarization)

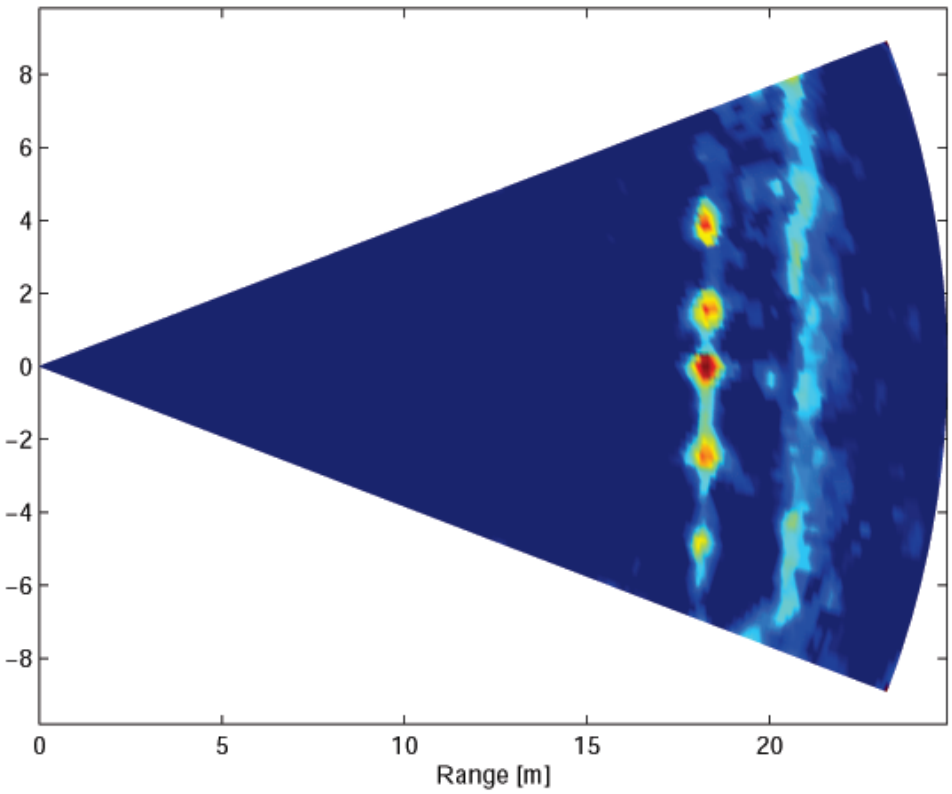

Figure 6.16: Image of polarization ratio for the power line scene with summer vegetation clutter shown in Figure 6.14(a).

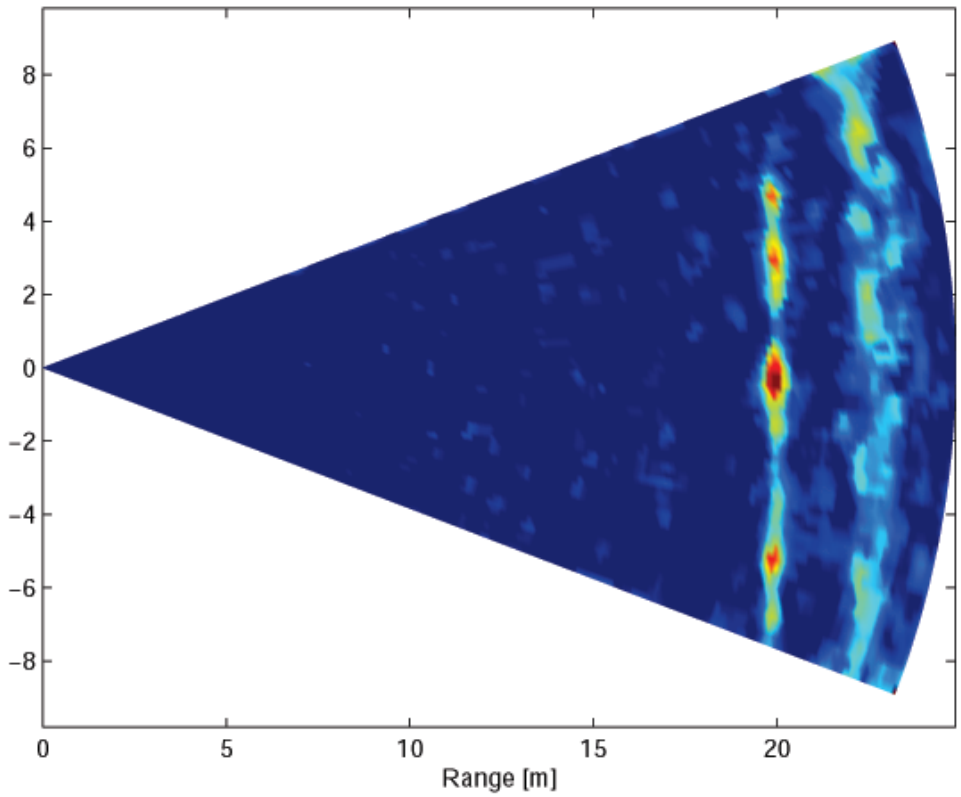

Figure 6.17: Polarimetric radar image for the power line scene with winter vegetation clutter shown in Figure 6.14(b). (VV-polarization)

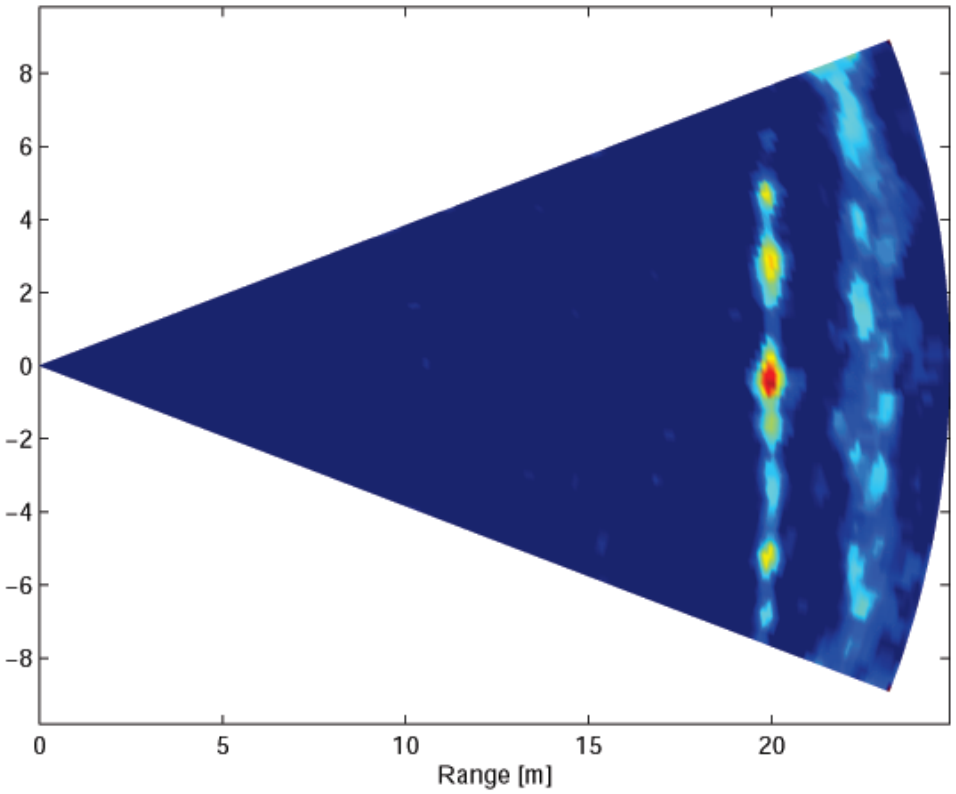

Figure 6.18: Image of polarization ratio for the power line scene with winter vegetation clutter shown in Figure 6.14(b).

6.4 Conclusions

In this Chapter, a prototype high resolution instrumentation polarimetric imaging radar is built up and polarimetric images are generated for some of the simulated typical traffic scenes, which include a scene consists of pedestrian, and vehicles, two scenes of military convoys, a scene of gravel road, and airborne traffic scene of a suspended power line with vegetation background clutter. The radar operation and functions of each units are described. The polarimetric imaging performance of the radar is evaluated with the images generated from the simulated traffic scenes. It is shown that polarimetric imaging of traffic scenes can be a new approach of radar data interpretation. Image processing based traffic scene analysis enables higher level perception of the scene than point target tracking based approach. The interpretation of the radar images can also be performed with established video image processing algorithms including edge detection, segmentation, and clustering with minor modification. When imaging radar is successfully combined with these algorithms, it can provide drivers/pilots with more reliable safety feature.

CHAPTER 7
CONCLUSIONS AND RECOMMENDATIONS

7.1 Summary

In this thesis, full polarimetric radar backscattering of power lines was characterized and power line detection algorithm was proposed and its feasibility was demonstrated in several ways. Followings are the major contributions of this thesis.

1. Polarimetric measurements of the backscattering response from power lines at millimeter-wave frequency under different surface conditions. These measurement provided the basis for the detection algorithm.

2. Development of power line detection algorithm to detect power lines in the strong background clutter.

3. Development of new PO based analytical model which predict the polarimetric backscatter response from power lines of arbitrary strand arrangement.

4. Construction of polarimetric real aperture radar for imaging of flying/traffic scenes.

5. Mapping of power lines from polarimetric SAR images are demonstrated and

the false alarm (FA), and probability of detection are formulated.

6. Demonstration of detection algorithm using developed radar simulator.

In Chapter 2, The radar backscatter behavior of power lines is investigated to develop detection algorithm. For this purpose, polarimetric radar backscattering measurements of power line samples of different diameter and strand arrangements are performed over wide range of incidence angles with fine increments at 94 GHz. Also, similar polarimetric backscatter measurements are conducted for cylinders of the same radii and lengths as the power line samples for identifying the scattering features of the power lines. The effect of the thin layer of water and ice on the polarimetric radar backscatter is investigated by repeating the measurement. Based on this phenomenological study, a polarimetric detection algorithm that makes use of the scattering features caused by braided structure of power line is proposed. The performance of the algorithm is experimentally demonstrated using rough asphalt surface and vegetation foliage as sample clutter background. The proposed algorithm is capable of detecting power lines in the strong clutter background.

In Chapter 3, a high frequency technique, based on iterative physical optics (PO) approach is developed for predicting polarimetric radar backscattering behavior of power lines of arbitrary strand arrangement. In the proposed scattering model, the induced surface current is obtained using the tangent plane approximation in an iterative manner where the first order current, obtained from the incident wave, is used as the source for the second order current and so on. It is shown that the co-polarized backscatter is dominated by the contribution from the first order PO currents whereas

the cross-polarized backscatter is generated by the second and higher order PO currents. Using this model, the effects of radar antenna footprint, surface irregularities, and the cable sag (when suspended between towers) on its radar backscatter are studied. To verify the validity of the proposed model, theoretical results are compared at 94 GHz with experimental results and are found to be in a good agreement.

In Chapter 4, The application of a statistical polarimetric detection algorithm that significantly improves the signal-to-clutter ratio is demonstrated. The coherence between the co- and cross-polarized backscatter component is used as the detection parameter. This statistical detection parameter can be applied to any extended targets such as suspended cable in clutter background. Detection criteria based on clutter backscattering coefficients, power line size, and aspect angle, as well as the number of independent samples are obtained. The performance of the algorithm for mapping power line in SAR images is demonstrated using a number of low-grazing incidence polarimetric SAR images at 35 GHz.

In Chapter 5, An instrumentation real aperture radar is presented, which performs acquisition and visualization of radar images of traffic scenes. The perception capabilities of high resolution radar in traffic environment is demonstrated and the practical realization approaches concerning hardware and data processing is discussed. The imaging capabilities in various traffic situations is demonstrated, proving the use of high resolution imaging radar may enable a number of attractive safety features for low-flying aircrafts and vehicles also.

In Chapter 6, A simulator is developed to test the ideas and scenarios related to detection of power lines using a radar mounted on a moving helicopter flying

above a landscape. The landscape, radar, and power lines are all parameterized and easily adjustable by the analyst. Various scenarios may be analyzed with the goal of detecting power lines in time to avoid a collision under all circumstances. The assumptions and approximations made during the simulator development are detailed along with detailed analysis of one scenario. It is shown that the idea has promise for future implementation on operational helicopters.

7.2 Recommendations for Future Work

Polarimetric radar backscatter measurements of power lines are conducted in the laboratory under far-field condition to investigate the angular response of the radar backscattering. Field measurements in the long range (several hundred meters) is not available due to the limit of the radar power and unavailability of big turntable. Although the angular response of radar backscattering in the long range is also predictable using the developed analytical model, the measured data can be useful information, if available. The effect of layer of thin water and that of ice layer on the radar backscattering is investigated, however, the effect of atmospheric attenuation on the polarimetric radar backscattering is not investigated, which can also a future work.

The MIT Lincoln Laboratory's 35 GHz SAR images are processed to detect power lines in the images and it is shown that the detection algorithm is well performed. The SAR images used in this investigation is not generated exclusively for this study. We picked several images which include power lines. Broad range of look angles and aspect angle was not available and the look angle for SAR images is deeper than the

that of actual flight scenarios. Look angles which is typical in real flight situations are similar to that of the ground based configuration which was set up in the Willow Run Airport for the generation of real aperture images. These problems can be overcome if a helicopter is flown with a radar mounted in it and detection of power lines is tried with different configuration parameters including look angle, aspect angle, clutters, and power lines.

In this dissertation, a radar simulator is developed and the detection of power lines in clutter background is demonstrated. It can be more realistic if more factors are included in the simulator, which include elevation antenna pattern effect, correlated speckle, loss through vegetation, natural texture in the clutter backscatter data, and man-made targets such as buildings.

The promising results obtained in this thesis work on the phenomenology of power line detection in the presence clutter background using polarimetric millimeter-wave radar demonstrate that a full automation of power line detection using proposed millimeter-wave radar is technically feasible. However, some issues must be carefully considered in the design of these systems such as legal aspect related to the responsibility in case of false and incorrect behavior of the system. Therefore, a long period of exhaustive tests and refinement must proceed the availability of these systems on the commercial market.

BIBLIOGRAPHY

BIBLIOGRAPHY

[1] *Aviation Week and Space Tech.*, July 6, 1987, p. 103

[2] Reedy, E.K., "Fundamentals of MMW RAdar Systems," in *Principles and Applications of Millimeter-Wave Radar*, N.C. Currie and C.E. Brown, Eds., chapter 2, pp. 19-71, Artech House, Norwood, MA, 1987

[3] Ioannidis, G.A. and D.E. Hammers, "Optimum antenna polarization for target discrimination in clutter," *IEEE Trans. Antennas Propagat.,* vol. 27, no.5, May 1979

[4] Al-Khatib, H. H., "Laser and millimeter-wave backscatter of transmission cables", *SPIE Vol 300 Physics and Technology of Coherent Infrared Radar*, pp. 212-229, 1981.

[5] Rembold, B., H.G. Wippich, M. Bischoff, and W.F.X. Frank, "A MM-wave collision warning sensor for helicopters", *Proceedings of Military Microwave*, pp. 344-351, 1982.

[6] Savan, M. and D.N. Barr, "Reflectance of wires and cables at 10.6 micrometer", Center for Night Vision and Electro-Optics, MSEL-NV-TR-0063, Jan 1988.

[7] Boerner, A. Kostinsk and B. James,, "On the concept of the Polarimetric Matched Filter in High Resolution Radar Imagery: An Alternative for Speckle Reduction", *Proceeding of IGARSS '88 Symposium*, Edinburgh, Scotland, Sep. 1988, pp.69-72, 1988.

[8] Sarabandi, K., L. Pierce, Y. Oh, and F.T. Ulaby, "Power lines: Radar measurements and detection algorithm for polarimetric SAR images," *IEEE Trans. Aerospace and Electronic Sys.,* vol. 30, no. 2, 632-648, April 1994.

[9] Marcum, J.I., "A statistical theory of target detection by pulsed radar", *IRE Trans.* , vol. IT-6, pp. 59-267, Apr., 1960

[10] Swerling, P., "Probability of fluctuating targets", *IRE Trans.* , vol. IT-6, pp. 269-300, Apr., 1960

[11] Kassam, S.A., "Analysis of CFAR processors in nonhomogeneous background ", *IEEE Trans. Aerospace and Electronic Sys.* , pp. 427-444, July, 1988

[12] Hansen, V.G., and X. Sawyers, H. Yamada, and W. Boerner, "Detectability loss due to greatest of selection in a cell averaging CFAR", *IEEE Trans. Aerospace and Electronic Sys.* , pp. 115-118, June, 1980

[13] Richard, J.T., and G.M. Dillard , "Adaptive detection algorithm for multiple target situations", *IEEE Trans. Aerospace and Electronic Sys.* , pp. 338-343, Apr., 1971

[14] Wilson, S.I., "Two CFAR algorithms for interfering targets and nonhomogeneous clutter", *IEEE Trans. Aerospace and Electronic Sys.* , pp. 57-71, June, 1993

[15] AL-Hussaini, E.K., "Performance of greater-of and censored greater-of detectors in multiple target environment ", *IEE Proceeding* , pp. 193-198, vol. 135, 1988

[16] Boston, J.R., "A fuzzy model of signal detection incorporating uncertainty", *IEEE* , pp. 1107-1112, June, 1993

[17] Russo, F., "A totally fuzzy approach to multisensor instrumentation ", *IEEE* , pp. 951-957, June, 1999

[18] Baldygo, W., "Artificial intelligence application to constant false alarm rate processing", *IEEE* , pp. 275-280, 1993

[19] Moriyama, T., M. Nakamura, Y. Yamaguchi, H. Yamada, and W. Boerner, "Classification of target buried in the underground by radar polarimetry", *IEICE Trans. Commun.* , pp. 951-957, June, 1999

[20] Kalusing, H., W. KEydel, "Feasibility of synthetic aperture radar with rotaing antennas (ROSAR)", *IEEE International Radar Conference*, pp. 51-56, 1990

[21] Novak, L., M. B. Sechtin, M. J. Cardullo, "Studies of target detection that use polarimetric radar data ", *IEEE Trans. Aerospace and Electronic Sys.,* vol. 25, no. 2, 150-165, Mar. 1989.

[22] Chan, T., Y. Kuga, A. Ishimaru,, "Experimental studies on circular SAR imaging in clutter using angular corellation function technique", *IEEE Trans. Geoscience and Remote Sensing* vol. 17, no.5, 2492-2497, Sep. 1999.

[23] Jackson, C.R., H. Rais, and A.W. Mansfield;, "Polarimetric target detection techniques and results from the Goddard Space Flight Center Search and Rescue Synthetic Aperture Radar (SAR2) program";, *Proceedings of SPIE Conference on Automatic Target Recognition VIII*, F.A. Sadjadi, Ed., SPIE Vol. 3371, Orlando, Florida, April 13-17, 1998, pp. 185-193.

[24] Novak, L. M., Sechtin, M. B., and Cardullo, M. J., "Studies of Target Detection Algorithms That Use Polarimetric Radar Data ," *IEEE Trans. Aerospace and Electronic Systems,* vol. 25, no. 2, 150-165, March 1989.

[25] Sivertson, W.E., Jr., "A Global Search and Rescue Concept Using Synthetic Aperture Radar and Passive User Targets",*NASA Technical Report NASA -TN-D-8172*, NASA Langley Research Center, Hampton, Va., U.S.A., April, 1976, 29 p.

[26] Bennett, Andrew J., Currie, Anthony, "Use of high-resolution polarimetric SAR for automatic target recognition", *SPIE Algorithms for Synthetic Aperture Radar Imagery IX* Vol. 4727, pp. 146-153, Aug., 2002

[27] Ringrose, Robert, Nicola Harris, "Ship Detection Using Polarimetric SAR DAta", *CEOS SAR Workshop Proceedings*, OCt, 1999

[28] Van Zyl, J.J., "Calibration of polarimetric radar images using only imge parameters and trihedral corner reflector responses," *IEEE Trans. Geoscience and Remote Sensing ,* vol. 28, no.12, May 1990

[29] Sarabandi, K., and M. Park, " A radar cross section model for power lines at millimeter-wave frequencies," *IEEE Trans. Antennas Propagat.,* accepted for publication.

[30] Sarabandi, K., and M. Park,"Millimeter-wave radar Phenomenology of power lines and a polarimetric detection algorithm," *IEEE Trans. Antennas Propagat.,* vol. 47, No. 12, pp. 1807-1813, Dec. 1999 .

[31] Sarabandi, K., and M. Park,"Extraction of pwer line maps from millimeter-wave polarimetric SAR images" *IEEE Trans. Antennas Propagat.,* vol. 48, no. 12, pp. 1802-1809, Dec. 2000.

[32] Ulaby,F.T., C. Elachi, *Radar Polarimetry for Geoscience Applications*, Artech House, Dedham MA, 1990

[33] Ulaby, F.T. and M.C. Dobson, *Handbook of Radar Scattering Statistics for Terrain*, Artech House, Norwood, MA, 1989

[34] Nashashibi, A., F.T. Ulaby, and K. Sarabandi, "Measurement and modeling the millimeter-wave backscatter response of soil surfaces," *IEEE Trans. Antennas Propagat.,* vol. 34, no. 2, 561-572, March 1996.

[35] Sarabandi, K., Eric S. Li, and A. Nashashibi, "Modeling and Measurements of Scattering from Road Surfaces at Millimeter-wave Frequencies," *IEEE Trans. Antennas Propagat.,* vol. 45, no. 11, pp. 1679-1688, Nov. 1997.

[36] Li, E.S., and K. Sarabandi, "Low grazing incidence millimeter-wave scattering models and measurements for various road surfaces," *IEEE Trans. Antennas Propagat.,* vol. 47, no. 5, May 1999.

[37] Mead, James B., Andrew L. Pazmany, Paul S. Chang, and Robert E. McIntosh, "Comparison of coherent and noncoherent polarimetric radar measurement at 95 GHz" *Radio Sci*, vol.31, no 2, pp. 325-333

[38] Ulaby, F.T., P.R. Sequeira, A. Nashashibi, and K. Sarabandi, "Semi-empirical model for radar backscatter from snow at 35 and 95 GHz," *IEEE Trans. Geosci. Remote Sensing.*, vol. 34, no. 5, pp. 1059-1065, Sept. 96.

[39] Gradshteyn, L.S. and I.M. Ryzhik, *Table of Integrals, Series, and Products*, Academic, San Diego, CA, 1980

[40] Ulaby, F.T., A. Nashashibi, A. El-Rouby, E. Li, R. Deroo, K. Sarabandi, R. Wellman, and B. Wallace, "95-GHz scattering by terrain at near-grazing incidence," *IEEE Trans. Antennas Propagat.,* vol. 46, no.1, pp. 3-13, Jan. 1998.

[41] Touzi, R. and A. Lopes, "Statistics of the Stokes parameters and of the complex coherence parameters in one-look and multi-look speckle field ", *IEEE Tans. Geosci. Remote Sensing*, vol. 34, pp. 519–532, Mar. 1996

[42] Currie, N.C. and C.E. Brown, eds., *Principles and Applications of Millimeter-Wave Radar* , Artech House, Norwood, MA, 1987

[43] Currie, N.C. and R.D. Hays, eds., *Millimeter-Wave Radar Clutter*, Artech House, Norwood, MA, 1992

[44] Henry, J.C., "The Lincoln Laboratory 35 GHz Airborne Polarimetric SAR imaging Radar System," *IEEE National Telesystems Conference,* ,Atlanta, GA, March, 1991

[45] Nashashibi, A., K. Sarabandi, F.T. Ulaby, "A calibration technique for polarimetric coherent-on-receive radar system," *IEEE Trans. Antennas Propagat.,* vol. 43, no. 4, pp. 396-404, April 1995.

[46] Sarabandi K., T.C. Chiu "Optimum Corner Reflectors for Calibration of Imaging Radar", *IEEE Transactions on Antennas Propagat.*, pp.1348-1361, Oct. 1996

[47] Gracey, G.C., *Overhead Electric Power Lines, Ernest Benn Ltd.*, London, 1963

[48] Anderson, W. C., "Consequences of Nonorthogonolality on the Scattering Properties of Dihederal Reflectors", *IEEE Transactions on Antenna Propagation* , vol. AP–35, pp. 1154–1159, Oct. 1987

[49] Senior, T.B.A., K.Sarabandi, and J. Natzke, "Scattering by a narrow gap", *IEEE Transactions on Antenna Propagation* , pp.1102-1110, July 1990

[50] Keiler, J.B., "Diffraction by a convex cylinder", *IRE Transactions on Antenna Propagation* , vol. AP-4, p. 312, 1956

[51] Andreasen, M.G., "Scattering from parallel metallic cylinder with arbitrary cross section", *IEEE Transactions on Antenna Propagation* , vol. AP-4, p. 812-817, 1956

[52] Van Vleck, J.H., "Theory of radar reflection from wires or thin metallic strips", *J. Applied Physics* , p. 274-294, 1947

[53] Kuga, Y., K.Sarabandi, A. Nashashibi, F.T. Ulaby, and R. Austin, "Millimeter-wave polarimetric scatterometer systems: measurement and calibration techniques", *Proc. AGARD, Electromag. Wave Propag. Panel 48 Symp.*, Montreal, May 1991.

[54] Skolnik, Merrill, *Introduction to Rarar Systems* , McGraw-Hill, 1986

[55] De Roo, Roger, Fawwaz T. Ulaby, Alaa El-Rouby, and Adib Nashashibi, , "MMW Radar Scattering Statistics: Terrain At Near Grazing Incidence," *IEEE Trans. Aerospace ans Electronic Systems,* vol. 35, no.3, pp. 1010-1018, July, 1999.